UNIVERSITÉ DE SHERBROOKE
Faculté de Génie
Département de Génie Chimique et de Génie Biotechnologique

CONTRIBUTION AUX ÉCOULEMENTS COMPLEXES GAZ-LIQUIDE: DÉVELOPPEMENT ET VALIDATION D'UN MODÈLE MATHÉMATIQUE

CONTRIBUTION TO COMPLEX GAS-LIQUID FLOWS: DEVELOPMENT AND VALIDATION OF A MATHEMATICAL MODEL

Thèse de doctorat es sciences appliquées
Spécialité: Génie chimique

Composition du jury:

Martin Désilets	Rapporteur
Nicolas Abatzoglou	Examinatreur
Fouzi Kerdouss	Examinatèur
Pierre Proulx	Directeur de thèse

Brahim **S**elma

Sherbrooke (Québec), Canada Octobre 2009

Erreur de pagination
Les gages 168-169-170 et 171 sont en double

Your file Votre référence
ISBN: 978-0-494-64226-9
Our file Notre référence
ISBN: 978-0-494-64226-9

To my parents

To my wife

To my son Redouane

To my brothers and sisters

To my friends and my teachers of primary school

Acknowledgements

I wish to express my gratitude to my supervisor, Professor Pierre Proulx, for his continued support, guidance and constructive criticism. Special thanks are also due to my collegue Dr. Fouzi Kerdouss for his vital support, invaluable insights and the use of his experience in muliphase flow modelling.

Furthermore, I would like to acknowledge the collaboration and companionship of my colleagues Dr. Mbark El Morsli and Dr. Abdelfetah Bannari who worked with me on the OPPUS Laboratory. I will also miss the many fruitful discussions with M. Rachid Bannari who worked on the OpenFOAM development and mathematical modelling.

My great thanks also go to France Auclair, Andrée Paradis, Louise Chapdelaine, Sylvie Lebrun, Louise Carbonneau and Benoît Côté for the arrangement of many administrative matters in the Department of Chemical Engineering.

Résumé

Cette étude décrit le développement et la validation d'un modèle mathématique pour la mécanique des fluides computationnelle (CFD). Ce modèle contribue aux simulations numériques des écoulements complexes gaz-liquide en prenant en considération la distribution des tailles des bulles avec les phénomènes de coalescence et de fragmentation avec une méthode numérique efficace et précise.

L'approche Euler-Euler développée précédemment pour les écoulements complexes est adaptée au présent projet. La turbulence en phase liquide est représentée au moyen d'un modèle de turbulence à deux équations $k - \epsilon$ avec addition de nouveaux termes sources supplémentaires pour tenir compte des effets de la dispersion des bulles et de l'interface gaz-liquide sur la rhéologie.

Le transfert du momentum à l'interphase est déterminé à partir de l'action instantanée des forces sur la phase dispersée. Ces forces peuvent être par exemple la force de trainée, de soulèvement, de masse virtuelle. Ces forces dépendent de la fraction volumique de la phase dispersée et dans ce travail, un modèle est développé afin de prédire les profils de la concentration, la vitesse du liquide et les paramètres de la turbulence avec une bonne précision. En outre, une corrélation de l'effet de la vitesse de dérive sur le comportement de la turbulence est proposée. La version révisée est basée sur une étude de la littérature existante.

Les équations de conservation sont discretisées en utilisant la méthode des volumes finis. Cette méthode est basée sur l'algorithme **PISO**.

Des techniques numériques avancées sont utilisées pour assurer la stabilité de la solution quand la fraction volumique de la phase dispersée est élevée ou a un taux de changement rapide [61].

Finalement, l'évaluation du modèle développé est faite en se basant sur une recherche bibliographique approfondie et sur des données expérimentales tirées de la littérature scientifique.

Différents tests ont été faite pour valider le modèle à savoir: les écoulements complexes gaz-liquide dans une colonne à bulles rectangulaire [133; 134; 135; 18], un réservoir à double

turbine [126; 127] et un bioréacteur [101].

Mots clés: Modélisation mathématique, les écoulements multiphasiques gaz-liquide, turbulence, bilan de population, mécanique des fluides computationnelle CFD, OpenFOAM. méthode des moments, méthode des classes, QMOM, DQMOM.

Abstract

This study describes the development and validation of Computational Fluid Dynamics (CFD) model for the simulation of dispersed two-phase flows taking in the account the population balance of particles size distribution.

A two-fluid (Euler-Euler) methodology previously developed for complex flows is adapted to the present project. The continuous phase turbulence is represented using a two-equation $k - \epsilon$ turbulence model which contains additional terms to account for the effects of the dispersed on the continuous phase turbulence and the effects of the gas-liquid interface.

The inter-phase momentum transfer is determined from the instantaneous forces acting on the dispersed phase, comprising drag, lift, virtual mass and drift velocity. These forces are phase fraction dependent and in this work revised modelling is put forward in order to capture a good accuracy for gas hold-up, liquid velocity profiles and turbulence parameters. Furthermore, a correlation for the effect of the drift velocity on the turbulence behaviour is proposed. The revised modelling is based on an extensive survey of the existing literature.

The conservation equations are discretised using the finite-volume method and solved in a solution procedure, which is loosely based on the PISO algorithm. Special techniques are employed to ensure the stability of the procedure when the phase fraction is high or changing rapidely [61].

Finally, assessment of the model is made with reference to experimental data for gas-liquid bubbly flow in a rectangular bubble column [133; 134; 135; 18], in a double-turbine stirred tank reactor [126; 127] and in an air-lift bioreacator [101].

Key words: mathematical modelling, complex flow gas-liquid, turbulence, population balance, computational fluids dynamics CFD, OpenFOAM, moments method, method of classes, QMOM, DQMOM.

Contents

List of Figures

List of Tables

Nomenclature

Roman Symbols

Symbol	Description	Units
a	interfacial area	m^2
A	surface face	m^2
A_d	multiplier term used in the two-equation model of turbulence	–
A_D	multiplier term used in the drag force	s^{-1}
$b(x_k)$	breakup frequency function	s^{-1}
C_f	friction coefficient	kg/m^3s^3
C_l	lift coefficient, dimensionless	–
C_t	turbulence coefficient, dimensionless	–
C_{vm}	virtual mass coefficient, dimensionless	–
C_μ	$k-\epsilon$ constant (=0.09), dimensionless	–
$C_{\mu,BIT}$	Bubble induced turbulence coefficient, dimensionless	–
d	bubble diameter	m
D	reactor diameter	m
f	friction factor	–
f_i	bubble volume fraction of group of size i,	–
f_j	bubble volume fraction of group of size j,	–
F	force vetor	N
g	acceleration vector due to gravity	m/s^2
H	reactor heigh (bubble column)	m
$\bar{\bar{I}}$	unit tensor, dimensionless	–
k	turbulent kinetic energy	m^2/s^2

K	exchange coefficient	$kg/m^3.s$
Nb	number of nodes used in DQMOM method	–
$\mathbf{k_L}$	mass transfer coefficient	m/s
P	pressure	Pa
$p(v, v_k)$	probability function, dimensionless	–
S	source term	–
t	time	s
$\overline{U}$	average velocity	m/s
$\mathbf{U}_\varphi$	velocity of phase φ	m/s
$\mathbf{U}_r$	relative velocity	m/s
W	reactor width	m

Greek Symbols

Symbol	Description	Units
α	Volume fraction, dimensionless	–
β	Dimensionless coefficient used for C_t model	–
Δ	Difference	–
ϵ	Turbulent kinetic energy dissipation rate	m^2/s^3
μ	Dynamic viscosity	kg/ms
ν	Kinematic viscosity	m^2/s
ρ	Density	kg/m^3
σ	Surface tension	N/m
Γ_i	Break-up frequency of bubbles of size group i	s^{-1}
γ_i	Fraction reassigned to nearby classes pivot	–
θ	angle between U_d and U_r	rad
η	Test function	–

Dimensionless Numbers

Symbol	Description	Definition
C_d	Drag coefficient	$\frac{\mathbf{F}_d}{\frac{1}{2}\rho_c A \mathbf{U}_r^2}$
Co	Courant number	$\frac{U_f \cdot S}{d \cdot S}\Delta t$
Eo	Eötvös number	$\frac{g\Delta\rho d^2}{\sigma}$
Re	Reynolds number	$\frac{\rho_c \mathbf{U}_r d}{\mu_c}$
St	Stokes number	$\frac{\rho_d d^2 \mathbf{U}_r}{18\rho_c \nu_c L}$
We	Weber number	$\frac{\rho_c d \mathbf{U}_r^2}{\sigma}$

Subscripts & Superscripts

Symbol	Description
c	continuous phase
d	dispersed phase
φ	phases index
eff	effective
(k)	first moment order, $k = 0, .., 2Nb - 1$
t	turbulent
D	drag
l	lift
vm	virtual mass
r	relative
i	interface
dis	dispersed
in	inlet
s	superficial
h	hydrolic

Chapter 1

Introduction

1.1 Background

Bubbly flow regime in the gas-liquid systems has a very important role in the modern chemical industry for a wide variety of applications including for example bubble columns, stirred-tank in bio-reactors, rotary gas injection to clean liquid aluminum and air-lift reactors. The optimal design and development of these apparatus rely on the ability to predict the complex gas-liquid flow. This can be accomplished by measurements or numerical modelling of the multiphase model equations, known as Computational Fluid Dynamics CFD, and by a combination of the two approaches taking advantage of the strengths of both. The goal of this work is to develop a model which accounts for the coupling of several phenomena such as bubble coalescence and breakage, bubble size distribution and mass transfer. Based on the Computational Fluid Dynamics (CFD) and the opensource CFD library OpenFOAM, we are able to develop new mathematical models including complex flow behavior while maintaining good numerical stability. CFD has been used namely to describe adequately systems as complex as the production of nanoparticles in plasma reactors but its use for

the multiphase flows of gas-liquid flows encountered in chemical reactors presents different challenges that have been only recently addressed fully. During the last few years, CFD has become an indispensable predicting tool for several engineering, scientific and current life applications. Nevertheless, the use of readily usable commercial CFD software is still far from routine, and for research applications is often very limited. In fact, they are often limited to well-defined applications, so one can not add or modify physical models to suit researchers needs. The use of open source software, such as OpenFOAM, allowed us to develop without the constraints of a commercial package, but of course at the expense of a much more involved work in the numerical model itself. At the end, the choice of the CFD platform was between the apparent ease of a commercial package (which is limited in terms of flexibility of the mathematical modelling), and the much more intense work of numerical modelling in an open-source package which involves a total control over all the mathematical an numerical models. At the end, the use of OpenFOAM proved to be a very good choice, combining very good numerical performance with an understanding of all the steps involved in the model from the differential equations set-up to the final report.

The modelling of multiphase flows with the presence of turbulence due to a generally very high agitation is still a tremendous challenge. This task requires both intense material and human resources [39] and it is usually necessary to modify and to adapt the physical and chemical laws according to the specific application. In most cases, the developed model represents those flows with a certain degree of accuracy, from a numerical point of view. From the literature, it is seen that solutions for these problems are progressing very fast but with some limitations (neglecting of certain forces, geometry different from reality, laboratory scale, numerical methods less efficient,etc.). Until now, there are few studies related to the problem of bubbly flows taking into account the bubble coalescence and break-up. These phenomena are due to the strong turbulence created by agitation, or the high inlet gas flows.

CFD methods, when they can be applied to a system, can provide data otherwise not accessible by traditional experimental techniques in a short time and often for low costs. For this reason, its use in designing multiphase reactors has increased in the last two decades along with the computer power availability. However, CFD is not experimental-free! Experimental validation and correlations are required for the closure of the multiphase model equations. Generally, the formal mathematical modelling of multiphase models uses two approaches. In the first, the bubble and liquid phases are considered as continuous phases, the phases occupying each a fraction of the volume, thus introducing the concept of volume fraction. This technique, where a set of Eulerian conservation equations is written for each phase is named the Eulerian-Eulerian method. The second method considers only the liquid phase as continuous and the bubble's movements in the liquid are described through a set of Lagrangian trajectory equations. This is the Eulerian-Lagrangian method. In the present study the first method is used, since it is well known that it is better suited for high volume fractions of bubbles encountered locally in the bubble columns. The bubbles and liquid phases are related through interaction forces that are described as drag, lift and virtual mass forces. These interphase forces are formulated, in the mathematical model, as source terms in the momentum conservation equations. The formulation of these terms is relatively straightforward but their inclusion in the numerical algorithm often results in significant difficulties in convergence and stability. Among the authors who introduced these terms in the modeling of bubble columns [49; 133; 103; 134]. Many authors also neglected the lift force [17; 95; 96; 44]. However, it has been shown that the lift force has a significant effect on the flow and void fraction fields of the columns [103; 80; 16]. A few authors used empirical formulations of the lift force coefficient, C_l, but mostly it has been assumed a constant value, from 0 to 0.5. Recent studies on bubble columns have been aimed at a better understanding and a more appropriate formulation of the interphase forces [136; 3; 106; 133; 21; 134].

The present work uses the Tomiyama correlation for the lift force, and is validated by com-

parison with the measurements data of [134; 135; 18]. The other interphase forces, the drag and virtual mass contributions, have been studied in depth by [104; 40; 102]. In the present work, the drag coefficient is also determined using the Tomiyama correlation, which is only a function of the Eötvös number. Virtual mass can be conceptually represented as the change in kinetic energy due to the acceleration of the bubbles. Sato and Sekoguchi [139] introduced the notion of "Bubble Induced Turbulence", a concept which takes into account the turbulence induced by the rotation of bubbles. The present work aims at the validation of the developed turbulence model and to apply it in the context of population balance modelling (PBM). A study of the current state of the art in the scientific literature on multiphase flow modelling reveals that largely, the models do not consider the influence of the dispersed phase and the influence of the gas-liquid interface on turbulence, as well as the turbulence induced by the rotation of the bubbles. In the present work we review many of the different formulations of these terms available in the literature, and proceed to a full integration of the validated terms in the standard $k-\epsilon$ model and the population balance equation, using the available published experimental data. The validation of these studies has been made using different gas-liquid systems (bubble columns, air-lift reactors and bio-reactors) [44; 45; 102]. The numerical solution of the developed mathematical model is made using the open source CFD package OpenFOAM (Field Operation And Manipulation) library. OpenFOAM uses advanced numerical methods and formal programming that can be used to represent the mathematical models in a form very close to the natural formulation.

1.2 Problem statement

The main objective of the current research project is to develop a mathematical model that represents the contribution of the turbulence and population balance on the multiphase flows. The problem of turbulence modelling in multiphase flows is studied and outlined in

the chapter 4. On the other hand, the population balance equation is implemented in the code to taking into account the bubble size distribution function. This model can help to predict the gas-liquid dynamics in the presence of several phenomena in gas-liquid systems.

The new open source software OpenFOAM is used for the solution of the model's nonlinear equation set. OpenFOAM presents several advantages; in particular, it provides complete access to the formulation of the mathematical models. Overall, the benefit expected by this study is to improve the efficiency of the processes that can be modelled using the present two-phase flow models. This improvement could have an impact on productivity, quality, flexibility (optimal design of chemical process).

1.3 Objectives

The scientific and technical objectives of this project are the development, validation and application of mathematical models for several multiphase flows applications. The developed model here includes some fundamental aspects and it is broad enough to be applied in industrial applications such as thermal plasma processing, bio-reactors, bubble columns, water treatment, stirred-tank reactors, polymerization and liquid aluminum purification using rotary gas injection process.

This thesis involves the following scientific axes and technical applications:

1. Development of a mathematical model to be used in bubbly flows.
2. Integration of the population balance equation and their solution by an efficient and robust technique; the Direct Quadrature Method of Moments (DQMOM).
3. Modelling of bubble coalescence and break-up phenomena.
4. Validation of the developed model with measurements for three different applications:
   - 4.1 Bubble columns
   - 4.2 Stirred-tank reactor

4.3 Air-lift bioreactor

5. Prediction of the mass transfer coefficient and Sauter mean diameter in bubbly flow regime

1.4 Present contribution

This study involves a contribution to the Computational Fluid Dynamics field as follows:

1- Development of new combination of physical models extending the standard $k-\epsilon$ model of turbulence. A full integration of source terms that represent the dispersed phase and gas-liquid interfaces on multiphase flows are included. The turbulence force induced by the rotational movement of bubbles and the drift velocity are considered.

2- Population balance equation and the use of new resolution techniques such as the direct quadrature method of moments "DQMOM".

3- Modelling of bubble coalescence and breakage using several physical models.

4- Mesh grid dependence study.

1.5 Thesis outline

Chapter 1 is a general introduction to the problem statement and objectives of this work followed by some contributions to complex system modelling.

Chapter 2 presents the mathematical equations describing the Newtonian Multiphase Fluid Flow, the different physical approaches and some of the more relevant physical models in this area.

Chapter 3: A brief definition of the turbulence modelling is presented. The most popular two-equations models of turbulence are explained and detailed.

Chapter 4: The population balance equation is introduced. Different solution techniques are highlighted in this section. In our project, the results of modelling are integrated, tested and validated with other numerical models and correlations obtained through experimentation.

Chapter 5 is devoted to the various mechanisms of bubble coalescence and break-up. The coupling between CFD and these phenomena is also discussed and developed.

Chapter 6 presents the numerical solution procedure. Spatial and time discretization are also outlined and detailed.

Finally, Chapters 7 and 8 are dedicated to the presentation of results, discussion and conclusion.

Chapter 2

Multiphase flow modelling

2.1 Introduction

In this Chapter, a typical multiphase flow system is described. Firstly, governing equations are stated along with basic turbulence and inter-phase momentum exchange modelling. Then, the numerical solution procedure is discussed. The test cases chosen for this purpose are the hydrodynamic behaviour in a rectangular bubble column at different mesh grid and stirred-tank reactor with double turbine.

In the chemical process industry, complex multiphase flow such as gas-liquid systems are often encountered. In the past, a large number of authors have devoted a considerable amount of effort to formulate field equations. The most important characteristic of a multiphase flow is the existence of an interface separating the continuous and dispersed phases. The various transfer mechanisms between phases and between a two-phase mixture and a surrounding wall strongly depend upon the two-phase flow regime. The two-phase flows are generally classified into three-flow regimes: the separated, transitional and dispersed flows. In this thesis, we will focus on only dispersed flows because of their most frequent occurrence in the

modern chemical industry.

In this chapter we look at two mathematical descriptions of two-phase flow. The first examined, is the Lagrangian approach which tracks each discrete particle separately with its trajectory being governed by its own equation of motion within the continuous phase. The second, is the Eulerian approach, treats the phases as inter-penetrating continua and models each phase by averaging the microscopic equations of motion.

2.1.1 Lagrangian Approaches

In the Lagrangian approach, the individual particles of the dispersed phase or a statistical sample thereof, are tracked through the flow domain. The conservation equation of momentum for each of the particles is expressed in a co-ordinate frame of reference which follows the trajectory. The resulting equation, which describes the motion of the particle in the continuous medium, relates the rate of change of the particle's velocity to the sum of forces acting upon it:

$$\rho_d \frac{d\mathbf{U}_d}{dt} = \sum \mathbf{F} \tag{2.1}$$

where

$\mathbf{U}_d$ is the velocity of dispersed phase

ρ_d is the dispersed phase density

$\mathbf{F}$ is the individual forces acting on the particles

The commonly accepted Lagrangian equation governing the motion of a particle at low Reynolds numbers reads [116]:

$$\frac{d\mathbf{U}_d}{dt} = \mathbf{F}_D + \frac{\rho_d}{\rho_c}\frac{D\mathbf{U}_c}{Dt} + \frac{1}{2}\frac{\rho_d}{\rho_c}\left(\frac{D\mathbf{U}_d}{Dt} - \frac{D\mathbf{U}_c}{Dt}\right)$$
$$+ \frac{6r^2(\pi\rho_c\mu_c)^{1/2}}{m_p}\int_{t_{p,0}}^{t_p}\frac{d/dt(\mathbf{U}_d - \mathbf{U}_c)}{(t_p - \tau)^{1/2}}d\tau + g\left(1 - \frac{\rho_d}{\rho_c}\right) \tag{2.2}$$

where

- d/dt Derivative with respect to time following the moving particle.
- D/Dt Total acceleration of the continuous phase as seen by the particle.
- $\mathbf{U}_d$ Velocity of dispersed phase particle.
- $\mathbf{U}_c$ Velocity of continuous phase.
- g Gravity.
- m_p Mass of particle.
- m_f Mass of fluid displaced by the particle $= m_p(\rho_c/\rho_d)$
- r Particle radius.
- $\mathbf{F}_D$ Drag force exerted on particle due to relative motion.
- μ_c Dynamic viscosity of the continuous phase.
- ρ_d Density of the dispersed phase.
- ρ_c Density of the continuous phase.
- t_p Particle response time.

Another significant advantage of the Lagrangian approach is that since there is one equation of motion for each particle, it is relatively easy to account for a distribution of particle sizes. Also, in gas-liquid and liquid-liquid systems, where the bubbles or droplets can break up into two or more smaller fragments or coalesce into a larger entity, the Lagrangian approach can be easily applied. The strategy of a Lagrangian analysis of two-phase flow is usually to follow a sufficient number of particles individually through the flow domain by solving the above equation for each one. The calculated trajectories of the particles are then used to obtain

information regarding the average nature of the flow, such as the dispersion coefficient, the local volume fraction or the local velocity.

The coupling between the continuous phase and the dispersed phase is often tackled in the solution procedure by using a two-step iterative approach. Here, the continuous phase flow is determined at a particular instant in time after which the motion and position of the individual dispersed phase elements are updated according to the newly calculated continuous phase flow. The exchange of momentum between phases is evaluated between steps so that it can be included as sources or sinks in the subsequently solved equations for the other phase. The sequence is repeated until sufficient data on the motion of the dispersed phase has been gathered by Kralj [11]. However, problems arise with the Lagrangian approach when the system of interest contains many particles. The first problem is that since there is one equation of motion for each particle the problem may become computationally too large to allow the trajectory of every particle to be calculated. Many particle trajectories are required in order to obtain meaningful information on the average nature of the flow. For example, a typical stirred-tank reactor (say with a volume of 6 m^3) with particles of 1 mm in diameter at a volume fraction of 1% contains approximately 10^8 particles. In such cases, a representative sample of particles trajectories are calculated and the overall flow properties inferred from these. Secondly, for high to moderate phase fractions, the increased coupling between the particles and the continuous phase can introduce numerical stability problems [11].

2.1.2 Eulerian Methods in Two Phase Flow

In the Eulerian approach, both the continuous and dispersed phases are described using Eulerian conservation equations written in fixed co-ordinates. Each phase is treated as a continuous medium, each inter-penetrating the other, and is represented by macroscopic

conservation equations, one set for each phase, which are valid throughout the entire flow domain. This approach is commonly known as the 'Two-Fluid' approach, or when more than two phases are considered, the 'Multi-Fluid' approach Ishii [77].

The two-fluid conservation equations are derived from the fundamental conservation equations for mass, momentum and energy which govern the behaviour of each phase and which are valid within each phase up to the interface between the phases: the familiar Navier-Stokes equations. The two-fluid conservation equations are obtained by applying a suitable averaging procedure to the entire two-phase system. The resulting mathematical form of the two-fluid equations is similar to the single-phase Navier-Stokes equations but contain extra terms which account for the transfer of mass and momentum between phases. In principle, the two-fluid approach is applicable to the entire range of flow regimes encountered in multi-phase flows, including the separated, dispersed and intermediate regimes. The physical character of the extra inter-phase mass and momentum transfer terms depends heavily on the exact nature of the flow, but the Eulerian approach is only limited by the ability to accurately model these terms, and is not inherently limited to dispersed systems. The generality of this approach comes at a cost, however, and it's main disadvantage is the difficulty in prescribing suitable inter-phase models for the flow regime under consideration. The identification of relevant inter-phase forces, such as drag, lift or virtual mass, is not as obvious as in the Lagrangian approach where each is represented by its own term and modelling the effects of many particles in averaged form can add considerable complexity to the modelling process. Similarly, the derivation of models which are applicable to flows which are between well defined regimes, or where the regime varies in different parts of the flow, can be extremely complex and the physical understanding of these situations may not be sufficiently well developed until now. However, the two-fluid approach is frequently more efficient than the Lagrangian approach, since individual dispersed phase elements are not tracked and the calculations are not restricted to the transient case.

The two- fluid equations for both phases are discretised using the same computational mesh and are often solved using similar techniques to those employed for single-phase flow but suitably extended to account for the coupled nature of the flow. Importantly, this approach allows the numerical problems arising from the coupling between phases to be more easily handled. For these reasons, the two-fluid approach has proven to be popular in the study of two-phase systems and has been adopted as the basis for the present work.

2.2 Governing equations

2.2.1 Continuity equation

To solve the multiphase model equations, discrete approaches need to be used. The time and spatial domain is subdivided in a finite elements. The most common and widely used discretization techniques are finite difference, finite volume and finite element methods [124; 67]. In the present work the finite volume method is used for solving non-linear equations system. A general local continuity equation of the quantity φ can be written as:

$$\frac{\partial}{\partial t}(\alpha_\varphi) + \nabla \cdot (\alpha_\varphi \mathbf{U}_\varphi) = 0 \tag{2.3}$$

Where α_φ is the volume fraction of a phase φ and $\mathbf{U}_\varphi$ is the velocity magnitude of phase φ. In the Eulerian frame, the following relation must be respected:

$$\sum_\varphi \alpha_\varphi = 1.0 \tag{2.4}$$

In order to solve the problem of boundedness, Spalding [25] suggested that Eqn. (2.3) should be solved for α_d and its counterpart for α_c, the solutions should then be recombined:

$$\alpha_d^\star = \frac{\alpha_d}{\alpha_d + \alpha_c} \tag{2.5}$$

The new phase fraction field $\alpha_d^\star$ will be bounded by zero and one only if α_d and α_c are both larger than zero and it follows that appropriate differencing is essential.

Weller [61] re-arranged the phase continuity Eqn. (2.3) so that all terms are in conservative form and α_d can be bounded at both ends, as follows:

$$\frac{\partial \alpha_d}{\partial t} + \nabla \cdot (\overline{\mathbf{U}} \alpha_d) + \nabla \cdot (\overline{\mathbf{U}}_r \alpha_d (1 - \alpha_d)) = 0 \tag{2.6}$$

Where $\overline{\mathbf{U}} = \alpha_d \overline{\mathbf{U}}_d + \alpha_c \overline{\mathbf{U}}_c$ and $\overline{\mathbf{U}}_r = \overline{\mathbf{U}}_d - \overline{\mathbf{U}}_c$.

2.2.2 Momentum equation

In absence of mass transfer between phases and for incompressible fluids in the steady-state regime, the local conservation equation of momentum is:

$$\frac{\partial}{\partial t}(\alpha_\varphi \vec{\mathbf{U}}_\varphi) + \nabla \cdot (\alpha_\varphi \vec{\mathbf{U}}_\varphi \vec{\mathbf{U}}_\varphi) + \nabla \cdot (\alpha_\varphi \nu_\varphi \nabla \vec{\mathbf{U}}_\varphi) = -\alpha_\varphi \nabla p + \nabla \cdot (\bar{\bar{\tau}}_\varphi) + \alpha_\varphi \vec{g} + \vec{\mathbf{F}} + \vec{\mathbf{R}}_\varphi \tag{2.7}$$

Where $\bar{\bar{\tau}}_\varphi$ represent the Reynolds stress tensor for the continuous phase defined as:

$$\bar{\bar{\tau}}_\varphi = -\nu_\varphi^{eff} \left(\nabla \bar{\mathbf{U}}_\varphi + \nabla \cdot \bar{\mathbf{U}}_\varphi^T - \frac{2}{3} I \nabla \cdot \bar{\mathbf{U}}_\varphi \right) + \frac{2}{3} Ik \tag{2.8}$$

and $\vec{\mathbf{R}}_\varphi$ represent the Coriolis and centrifugal forces applied in the rotating reference of frames (MRF) and is written as follow:

$$\vec{\mathbf{R}}_\varphi = -2\alpha_\varphi \rho_\varphi \vec{\mathbf{N}}_\varphi \times \vec{\mathbf{U}}_\varphi - \alpha_\varphi \rho_\varphi \vec{\mathbf{N}}_\varphi \times (\vec{\mathbf{N}}_\varphi \times \vec{r}_\varphi) \tag{2.9}$$

Here $\vec{\mathbf{N}}$ represent the rotating velocity (**RPM**) and $\vec{r}$ is the position vector (m). ν_φ^{eff} is the effective kinematic viscosity of phase φ. $\vec{\mathbf{U}}_\varphi$ and $\vec{\mathbf{F}}$ are respectively the velocity field of phase φ and the interfacial forces due to drag, lift and virtual mass.

2.2.3 Interfacial momentum exchange equations

In the present work the drag and the lift forces developed by Tomiyama et al. [4] are used to determine the interfacial momentum exchange. In the Eulerian-Eulerian approach used here, and at high volume fraction (>10%) we consider the dispersed phase as a continuous phase using the same momentum and continuity equations applied for the continuous phase. Hence, the instantaneous inter-phase momentum exchange is determined by assembling the forces acting on the dispersed bubbles. The main contributions are drag, lift, virtual mass, and the Basset forces. In this section, the exchange terms are written as components of these different contributions:

$$\overrightarrow{\mathbf{F}} = \overrightarrow{\mathbf{F}}_D + \overrightarrow{\mathbf{F}}_l + \overrightarrow{\mathbf{F}}_{vm} \tag{2.10}$$

The Drag Force

The relative motion between a submerged body and the surrounding fluid gives rise to the so-called drag force. It is a resistance of a particle in a fluid environment such as water or air. For spherical dispersed phase particles we have Rusche [56]:

$$\overrightarrow{\mathbf{F}}_D = \mathbf{A}_D \overrightarrow{\mathbf{U}}_r \tag{2.11}$$

Where

$$\mathbf{A}_D = \frac{3}{4}\frac{\alpha_d C_D}{d}|\overrightarrow{\mathbf{U}}_r| \tag{2.12}$$

Here d is the bubble or particle diameter, $\overrightarrow{\mathbf{U}}_r$ is the mean relative velocity $(\overrightarrow{\mathbf{U}}_d - \overrightarrow{\mathbf{U}}_c)$. The drag coefficient C_D depends on the characteristics of the flow surrounding the body and is a function of the Eötvös number for the case of bubbles. In the present work, for the drag coefficient C_D the particle drag model of Tomiyama is chosen, which gives good results for

large bubbles ($> 5\ mm$) and is defined as follow:

$$C_D = \frac{8}{3}\frac{\mathbf{Eo}(1-E^2)}{E^{2/3}\mathbf{Eo} + 16(1-E^2)E^{\frac{4}{3}}}\frac{1}{F(E)^2} \tag{2.13}$$

Where **Eo** is the Eötvös number defined as:

$$\mathbf{Eo} = \frac{g\Delta\rho d^2}{\sigma} \tag{2.14}$$

The Eötvös parameter is a dimensionless number and it can be used to characterize the shape of bubbles (see Fig. 2.1) or drops moving in a surrounding fluid. Eötvös number may be regarded as proportional to buoyancy force divided by surface tension force.

Here, g and σ are respectively the gravity and surface tension.

$$E = \frac{1}{1 + 0.163\mathbf{Eo}^{0.757}} \tag{2.15}$$

and

$$Eo_d = \frac{\mathbf{Eo}}{E^{2/3}} \tag{2.16}$$

and

$$F(E) = \frac{sin^{-1}(\sqrt{1-E^2}) - E\sqrt{1-E^2}}{1-E^2} \tag{2.17}$$

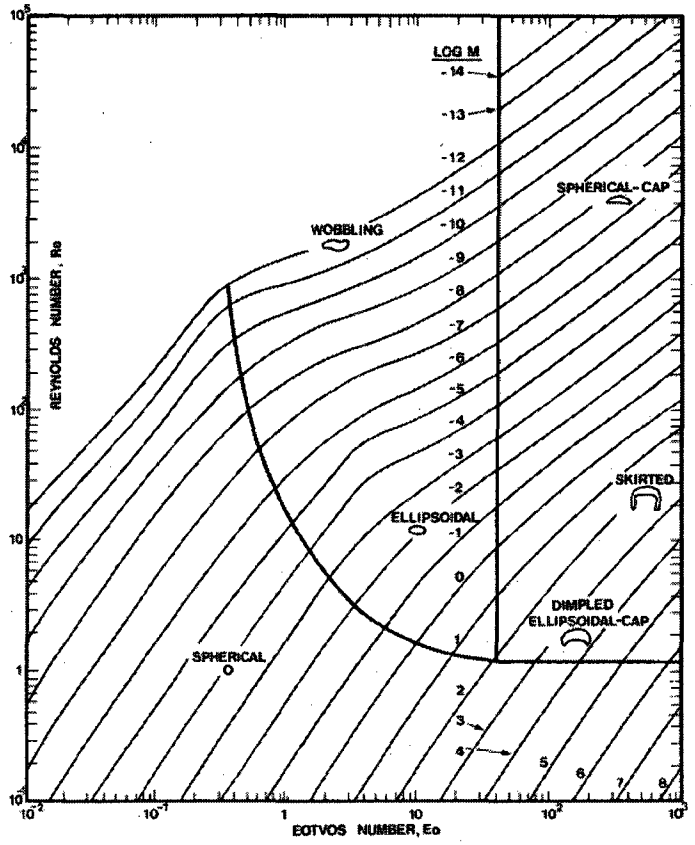

Figure 2.1: Shape regimes of bubbles according to Eötvös number

The Lift Force

The lift force $\overrightarrow{\mathbf{F}}_l$ describes the lateral force experienced by a particle subjected to a shearing flow field or due to the rotation of the particle itself. It is important for gas-liquid systems in which regions of high shear exist and it can have a large effect on phase distribution. The lift fore is defined as suggested by Drew [23] and [22]:

$$\overrightarrow{\mathbf{F}}_l = \alpha_d C_l \overrightarrow{\mathbf{U}}_r \times (\nabla \times \overrightarrow{\mathbf{U}}_c) \tag{2.18}$$

Here C_l represent the lift coefficient which is calculated using the Tomiyama correlation as follows:

$$C_l = \begin{cases} min[0.288tanh(0.121\mathbf{Re}), f(Eo_d)] & Eo_d < 4 \\ f(Eo_d) & 4 \leqslant Eo_d \leqslant 10.7 \end{cases} \tag{2.19}$$

where

$$f(Eo_d) = 0.105(Eo_d)^3 - 0.0159(Eo_d)^2 - 0.0204Eo_d + 0.474 \tag{2.20}$$

The Virtual Mass Force

By definition, the virtual mass force can be understood by considering the change in kinetic energy of fluid surrounding an accelerating bubble. The effect of virtual mass force is much larger for a bubble in liquid than for a drop in gas due to the higher liquid density surrounding the bubble. The virtual mass coefficient C_{vm} is often set to 0.5 for rigid spherical particles in the literature Carrica et al. [98]. For low phase fraction $\overrightarrow{\mathbf{F}}_{vm}$ is given as:

$$\overrightarrow{\mathbf{F}}_{vm} = \alpha_c C_{vm} \left(\frac{D_c \overrightarrow{\mathbf{U}}_c}{Dt} - \frac{D_d \overrightarrow{\mathbf{U}}_d}{Dt} \right) \tag{2.21}$$

Where $\frac{D_\varphi}{Dt}$ denotes the substantive derivative which is defined as:

$$\frac{D_\varphi}{Dt} = \frac{\partial}{\partial t} + \mathbf{U}_\varphi \cdot \nabla \tag{2.22}$$

The Basset Force

The Basset force represents the influence of the time dependent development of the boundary layer on the particle surface in accelerating flows. In essence, it takes into account the fact that the drag on the particle depends on the previous history of the particle motion. The Basset force is given by:

$$\mathbf{F}_B = \frac{3}{2} d^2 \sqrt{\pi \rho_c} \int_0^t \frac{d}{dt}(|\mathbf{U}_d - \mathbf{U}_c|)_{t=t'} \frac{dt'}{\sqrt{t-t'}} \tag{2.23}$$

in gas-liquid flows, the Basset force is very small when compared to the drag force and is usually neglected.

2.2.4 Interfacial closure summary

Collecting the models for the various interfacial forces described above and substituting them into Eqn. (2.10) we have

$$\vec{\mathbf{F}} = \frac{3}{4}\frac{\alpha_d C_D}{d}\vec{\mathbf{U}}_r|\vec{\mathbf{U}}_r| + \alpha_d C_l \vec{\mathbf{U}}_r \times (\nabla \times \vec{\mathbf{U}}_c) + \alpha_c C_{vm}\left(\frac{D_c \vec{\mathbf{U}}_c}{Dt} - \frac{D_d \vec{\mathbf{U}}_d}{Dt}\right) \tag{2.24}$$

In this work, two values of 0.25 and 0.5 for the virtual mass coefficient are used in the comparison with the experimental data.

Chapter 3

Turbulence modelling

Turbulence modeling is one of three key elements in computational fluid dynamics (CFD), in particular when one is interested in industrial processes Wilcox [26]. The other key elements are the grid generation and numerical algorithms development. By definition, a mathematical model of turbulence is one that approximates the real physical behaviour of turbulent flows. As examples of turbulence motion, flow in the wake of a cylinder, bubble columns, stirred reactors,...etc. Really most of all flows of practical engineering situations are turbulent.

3.1 Introduction

Most fluid flows occurring in nature are turbulent. Turbulence can be described as a state of continuous instability in the flow, where it is still possible to separate the fluctuations from the mean flow properties. It is characterized by irregularity in the flow, increased diffusivity and energy dissipation Tennekes and Lumley [57]. Turbulent flows are always three-dimensional and time dependent, even if the boundary conditions of the flow do not change in time. The range of scales in such flows is very large, from the smallest turbulent

eddies characterized by Kolmogorov microscales, to the flow features comparable with the size of the geometry. A comprehensive review of simulation techniques for turbulent flows can be found in Ferziger and Peric [69] works. A brief overview of the modelling techniques will be given here.

There are several possible approaches to the simulation of turbulent flows. The first, Direct Numerical Simulation (**DNS**) ([130; 129; 115; 87]) numerically integrates the governing equations over the whole range of turbulent scales. The requirements on mesh resolution and time-step size put very high demands on the computer resources, rendering it unsuitable for engineering applications. The second approach is generally known as Large Eddy Simulation (**LES**). In order to separate different length scales in a turbulent flow field, a spatial filter is applied. Large scale structures that can be resolved by the numerical method on a given mesh are called the super-grid scales. The influence of all other (sub-grid) scales to the super-grid behaviour is modelled. The rationale behind this principle lies in the fact that the small scales of turbulence are more homogeneous and isotropic and therefore easier to model. As the mesh gets finer, the number of scales that require modelling becomes smaller, thus approaching the Direct Numerical Simulation. Examples of this approach can be found in [73; 65; 138]. In the present study, the above approaches cited here (**DNS**, **LES**, **RANS**) are presented here briefly as follow:

- **Direct Numerical Simulation (DNS)**: it is not a model, Navier-Stokes Equations are computed in their most general form meaning that the complete spectrum of involved frequencies and length scales are solved. This approach is only feasible at current time for Low Reynolds number flows, due to limitation on computer resources, and used mainly as validation test for other approaches or as a help in understanding turbulence physics.

- **Large Eddy Simulation (LES)**: remembering that energy is contained

mainly in the largest scales, this model reduces the range of interest only to the biggest vortices. It employs, in fact, a time dependent three dimensional computation of the large-eddy structure and a model for the small scales. It basically consists in filtering in space the Navier-Stokes Equations with a high-pass filter, resolving for scales that actually are the energy-containing scales and modelling dissipation subrange behaviour. LES is becoming more and more popular in the CFD community, particular complexities in treating boundary conditions and the need for wide computer resources still limit the use to simple geometries and specific areas of interest in which turbulence modelling is more than fundamental (turbulent combustion, wake effects, chemical reactions).

• **Reynolds Averaged Navier Stokes (RANS)**: Navier-Stokes Equations are averaged in time on a period long enough to contain also lowest frequency oscillation. The unsteady behaviour of the turbulent flows is completely neglected, turbulence become a steady phenomenon simply considering the effects of fluctuations onto the mean flow. At the state of art RANS simulations are the standard for flows involving heat transfer of industrial interest. In fact unsteady phenomena result in being determinant for such simulations. Because of its ease of implementation and the speed in solving, supported by a good accuracy in modelling mean flows, one can reasonably believe that this approach will be used for many years to come.

3.2 History of turbulence modelling

The earliest attempts to constructing a mathematical model of turbulence flows goes back to Boussinesq [62] works which introduced the concept of the so-called eddy viscosity. In the nineteenth century, Prandtl (1925) introduced the mixing length which formed the basis of all turbulence modeling research for the next twenty years. In 1945's, Prandtl postulated a model in which the eddy viscosity depends upon the kinetic energy of the turbulent fluctu-

ations, k. He proposed a partial-differential equation approximating the exact equation for k. This model is thus called one-equation model of turbulence.

Kolmogorov (1942) introduced the first complete model of turbulence. In addition to having an equation for k, he introduced a second parameter ω that he referred to as "the rate of dissipation of energy in unit volume and time". This model is thus termed a two-equation model of turbulence. It went with virtually no applications for the next 25 years because of the unavailability of computers to solve its nonlinear differential equations.

3.2.1 one-equation models of turbulence

Prandtl (1945) postulated that the dissipation assumes the following form Wilcox [26]:

$$\epsilon \sim k^{3/2}/l \tag{3.1}$$

Introducing a closure coefficient C_k, the dissipation is:

$$\epsilon = C_k k^{3/2}/l \tag{3.2}$$

Thus, Prandtl's one-equation model is as follows:

$$\frac{\partial k}{\partial t} + \mathbf{U}_j \frac{\partial k}{\partial x_j} = \tau_{ij} \frac{\partial \mathbf{U}_i}{\partial x_j} - C_D \frac{k^{3/2}}{l} + \frac{\partial}{\partial x_j}\left[(\nu + \nu^t/\sigma_k)\right] \tag{3.3}$$

where τ_{ij} is the Reynolds-Stress Tensor, if we assume the Boussinesq approximation, the Reynolds-Stress is given by:

$$\tau_{ij} = 2\nu_T S_{ij} - \frac{2}{3} k \delta_{ij} \tag{3.4}$$

Here, S_{ij} is the strain-rate tensor. We can define the kinematic eddy viscosity as follows:

$$\nu^t = k^{1/2} l = C_D \frac{k^2}{\epsilon} \tag{3.5}$$

The one-equation model is not, by far, a universal turbulence model. Therefore the development of more general models is necessary.

3.2.2 Two-equation models of turbulence

Turbulence modelling for two-phase flows has been reviewed recently by several authors [36; 16; 34; 53]. As in a single-phase flow turbulence modelling, second-order closure models, which solves transport equations for each component of the Reynolds stresses, constitutes the highest level of closure currently feasible for practical applications. So far, only two authors [28; 80] developed two-phase Reynolds stress turbulence models, whereas the majority of authors invoke the Boussinesq [62] hypothesis and model the turbulent stress-strain relation analogous to the constitutive relation of a viscous fluid, e.g. [27; 123; 5; 131; 42; 103; 92; 50]. The turbulent viscosity is then related to the fluid's turbulent kinetic energy k and its dissipation rate ϵ, which are governed by their own transport equations.

We limit our discussion to the more commonly used $k-\epsilon$ models. In fact, a wide variety of $k-\epsilon$ models exists, the most noteworthy being the standard $k-\epsilon$ model by Jones and Launder [72]. Before building and analyzing the structure of the transport equation for turbulent kinetic energy k and turbulent kinetic energy dissipation ϵ, a general overview common to all $k-\epsilon$ models is needed, in order to understand how k and ϵ are related to the wanted scalar μ^t.

First the turbulent length scale l_t is computed locally as:

$$l_t = C_\mu \frac{k^{3/2}}{\epsilon} \tag{3.6}$$

and second, following the definition of length scale, one obtains:

$$\mu_t = C_\mu \rho k^{1/2} l_t = C_\mu \rho \frac{k^2}{\epsilon} \tag{3.7}$$

3.2.3 The standard $k-\epsilon$ model

The most popular two-equation turbulence model is the $k-\epsilon$ model. The central paper for this model is that published by Jones and Launder [72] which is, in the turbulence modelling community, well known as the standard $k-\epsilon$ model of turbulence. The idea in this model is to derive the exact equation of ϵ and to find suitable closure approximations for other parameters. Thus, the standard $k-\epsilon$ is as follows:

Turbulent viscosity

$$\nu^t = C_\mu \frac{k^2}{\epsilon} \tag{3.8}$$

Kinetic energy

$$\frac{\partial k}{\partial t} + \mathbf{U}_j \frac{\partial k}{\partial x_j} = \tau_{ij} \frac{\partial \mathbf{U}_i}{\partial x_j} - \epsilon + \frac{\partial}{\partial x_j}\left[(\nu + \nu^t/\sigma_k)\frac{\partial k}{\partial x_j}\right] \tag{3.9}$$

Dissipation rate

$$\frac{\partial \epsilon}{\partial t} + \mathbf{U}_j \frac{\partial \epsilon}{\partial x_j} = C_{\epsilon,1}\frac{\epsilon}{k}\tau ij \frac{\partial \mathbf{U}_i}{\partial x_j} - C_{\epsilon,2}\frac{\epsilon^2}{k} + \frac{\partial}{\partial x_j}\left[(\nu + \nu^t/\sigma_\epsilon)\frac{\partial \epsilon}{\partial x_j}\right] \tag{3.10}$$

Closure coefficients and auxiliary relations:

$$C_{\epsilon,1} = 1.44, \quad C_{\epsilon,2} = 1.92, \quad C_\mu = 0.09, \quad \sigma_k = 1.0, \quad \sigma_\epsilon = 1.3$$

3.2.4 The Mudde et al. (1999) closure terms for $k-\epsilon$ model

Following the work of Robert and Oliver [49], the two-equations $k-\epsilon$ model has been modified to the following formulation:

$$\frac{\partial}{\partial t}\left(\alpha_c k\right) + \nabla \cdot \left(\alpha_c \mathbf{U}_c k\right) = \nabla \cdot \left(\alpha_c \frac{\mu_c^t}{\sigma_k}\nabla k\right) + \Pi_k + \Pi_k^i \tag{3.11}$$

and

$$\frac{\partial}{\partial t}\left(\alpha_c \epsilon\right) + \nabla \cdot \left(\alpha_c \mathbf{U}_c \epsilon\right) = \nabla \cdot \left(\alpha_c \frac{\mu_c^t}{\sigma_\epsilon}\nabla \epsilon\right) + \Pi_\epsilon + \Pi_\epsilon^i \tag{3.12}$$

Where Π_k and Π_ϵ denote the ordinary one-phase production and dissipation terms defined as follow

$$\Pi_k = \alpha_c G \tag{3.13}$$

and

$$\Pi_\epsilon = \alpha_c \frac{\epsilon}{k}(C_1 G - C_2 \epsilon) \tag{3.14}$$

Here, G stands for the production of turbulent kinetic energy and is defined as:

$$G = 2\nu_c^{eff}\left(\nabla \overline{\mathbf{U}}_c \cdot dev(\nabla \overline{\mathbf{U}}_c + (\nabla \overline{\mathbf{U}}_c)^T)\right) \tag{3.15}$$

Where *dev* represents the deviatory component defined as:

$$dev\mathbf{T} = \mathbf{T} - \frac{1}{3}(tr(\mathbf{T})) \tag{3.16}$$

$\mathbf{T}$ is a second rank tensor and tr is the trace of this tensor.

The effective viscosity of the continuous phase is calculated from $\nu_c^{eff} = \nu_c + \nu^t$ where ν^t is given by the Eqn. (3.8). The values of C_μ, C_1, C_2, σ_k and σ_ϵ are unchanged from the originally derived for single-phase flow and they are summarized in Table 3.1.

Table 3.1: Coefficients used in the different $k-\epsilon$ models. NC : not considered, T.C : Tomiyama correlation

Constants	C_μ	C_1	C_2	C_3	σ_k	σ_ϵ	C_t	$C_{\mu,BIT}$
Fluent	0.09	1.44	1.92	1.2	1.0	1.3	NC	NC
OpenFOAM	0.09	1.44	1.92	NC	1.0	1.3	NC	NC
This work	0.09	1.44	1.92	1.2	1.0	1.3	C_t	0.6

From the equations (3.11) and (3.12) Π_k^i and Π_ϵ^i includes the effect of the interfaces on the turbulent kinetic energy and the dissipation rate respectively. According to Bel F'Dhila and Simonin [103], the Π_k^i term is formulated as:

$$\Pi_k^i = \frac{\rho_d}{(\rho_c+\rho_d)}\alpha_d \mathbf{F}_D\big[< \mathbf{U}_c^{"}.\mathbf{U}_d^{"} >_d -2k + \mathbf{U}_{drift}.\mathbf{U}_r\big] \tag{3.17}$$

where $< \mathbf{U}_c^{"}.\mathbf{U}_d^{"} >_d$ represent the covariance defined by the Eqn. (3.30).
The Π_ϵ^i is modelled according to Elghobashi and Abou-Arab [125]:

$$\Pi_\epsilon^i = C_3\frac{\epsilon}{k}\Pi_k^i \tag{3.18}$$

Where C_3 is constant of the standard model of turbulence (see table 3.1) and $\mathbf{F}_d$ is the drag force density coefficient given by:

$$\mathbf{F}_d = \left(\frac{\alpha_d\alpha_c\rho_d f}{\tau_p}\right) \tag{3.19}$$

and $\mathbf{U}_{drift}$ is the drift velocity used to correct the relative velocity as follows:

$$\mathbf{U}_r = (\mathbf{U}_d - \mathbf{U}_c) - \mathbf{U}_{drift} \tag{3.20}$$

As mentioned, the drift velocity accounts for the dispersion of the particles due to transport by turbulent fluid motion and is calculated by Robert and Oliver [49]:

$$\mathbf{U}_{drift} = -D_{c,d}^t \cdot \left[\frac{1}{\alpha_d}\nabla\alpha_d - \frac{1}{\alpha_c}\nabla\alpha_c\right] \tag{3.21}$$

where $D^t_{c,d}$ is the fluid-bubble turbulent dispersion tensor and is expressed as:

$$D^t_{c,d} = \frac{1}{3}\tau^t_{c,d} < \mathbf{U}^{"}_c \mathbf{U}^{"}_d >_2 \tag{3.22}$$

In Robert and Oliver [49] works, the turbulence of the dispersed phase is treated using three time scales: the characteristic time of turbulent eddies τ^t_c, the characteristic time of particles entrainment by the fluid motion $\tau^F_{c,d}$ and the characteristic time of the fluid turbulence viewed by the bubbles $\tau^t_{c,d}$. The last three time scales are given by:

$$\tau^t_c = \frac{3}{2} C_\mu \frac{k}{\epsilon} \tag{3.23}$$

$$\tau^F_{c,d} = \frac{1}{\mathbf{F}_d}\left(\frac{\rho_d}{\rho_c} + C_A\right) \tag{3.24}$$

and

$$\tau^t_{c,d} = \frac{\tau^t_c}{\sigma_k}\left[1 + C_\beta \zeta_r^2\right]^{(-1/2)} \tag{3.25}$$

Here, ζ_r is the ratio between the characteristic time of the turbulent eddies and the characteristic transit time, $\tau^T_{c,d}$, required for the bubbles to cross the large eddies:

$$\zeta_r = \frac{\tau^t_c}{\tau^T_{c,d}} = \frac{|\mathbf{U}_r|}{\sqrt{(2/3)k}} \tag{3.26}$$

The parameter C_β is defined as:

$$C_\beta = 1.8 - 1.35 cos^2(\theta) \tag{3.27}$$

with

$$cos(\theta) = \frac{\overrightarrow{\mathbf{U}_d}\overrightarrow{\mathbf{U}_r}}{\|\overrightarrow{\mathbf{U}_d}\| \cdot \|\overrightarrow{\mathbf{U}_r}\|} \tag{3.28}$$

the turbulent kinetic energy k_d of the dispersed phase and the covariance $< \mathbf{U}^{"}_c . \mathbf{U}^{"}_d >_d$ are given by:

$$k_d = k\left[\frac{b^2 + \eta_r}{1 + \eta_r}\right] \tag{3.29}$$

and

$$< \mathbf{U}_c^{"}.\mathbf{U}_d^{"} >_d = 2k\left[\frac{b+\eta_r}{1+\eta_r}\right] \tag{3.30}$$

with $\eta_r = \tau_{c,d}^t/\tau_{c,d}^F$ and $b = \dfrac{1+C_A}{\rho_d/\rho_c + C_A}$ $(C_A = 0.5)$.
In this model, only the effect of the interfaces on the turbulence terms are included.

3.2.5 The Rusche (2002) closure terms for $k-\epsilon$ model

As mentionned, most two-phase turbulence models of dispersed flows are based on a single-phase turbulence model for the continuous phase. The presence of the dispersed phase is accounted for by additional terms. Recently, Tabor [50] outlined a more elaborate, four-equation model where separate $k-\epsilon$ systems are assembled for each phase. This model requires additional closure and more effort is needed to finalize the coupling terms. However, in the work of Rusche [56], the two-fluid turbulence model extended by Gosman et al. [5] is adopted. It consists of the standard $k-\epsilon$ model of Jones and Launder [72] with the effect of the dispersed phase on the turbulence, while the model of Robert and Oliver [49] presented above deals with the effect of the interface. The two-equations $k-\epsilon$ are then written as:

$$\frac{\partial}{\partial t}\left(\alpha_c k\right) + \nabla\cdot\left(\alpha_c \overline{\mathbf{U}}_c k\right) - \nabla\cdot\left(\frac{\nu_c^{eff}}{\sigma_k}\nabla k\right) = \Pi_k - \alpha\epsilon + \Pi_k^{dis} \tag{3.31}$$

$$\frac{\partial}{\partial t}\left(\alpha_c \epsilon\right) + \nabla\cdot\left(\alpha_c \overline{\mathbf{U}}_c \epsilon\right) - \nabla\cdot\left(\frac{\nu_c^{eff}}{\sigma_\epsilon}\nabla\epsilon\right) = \Pi_\epsilon + \Pi_\epsilon^{dis} \tag{3.32}$$

The additional two-phase source terms are:

$$\Pi_k^{dis} = \frac{2k\alpha_d \mathbf{A}_d(C_t-1)}{\rho_c} + \frac{\mathbf{A}_d\nu^t}{\rho_c\sigma}\frac{\nabla\alpha_d}{\alpha_c}\cdot\overline{\mathbf{U}}_r \tag{3.33}$$

$$\Pi_\epsilon^{dis} = \frac{2C_3\epsilon\alpha_d A_d(C_t-1)}{\rho_c} \tag{3.34}$$

Table 3.2: Multiplier term used in the two-equation model of turbulence

Multiplier term	Gosman et al. [5]	Weller [61]
$\mathbf{A}_d$	$\alpha_d \frac{3}{2} \frac{\rho_c}{\rho_d} C_D \lvert\overline{\mathbf{U}}_r\rvert$	$\alpha_d \alpha_c \frac{3}{4} \left(f_d \frac{C_{dd}\rho_c}{d_d} + f_c \frac{C_{dc}\rho_d}{d_c} \right) \lvert\overline{\mathbf{U}}_r\rvert$

Here, the drag multiplier term $\mathbf{A}_d$, which depends on the inter-phase momentum transfer, is defined in Table 3.2. In this model, the presence of dispersed phase is accounted for by additional source terms, which are related to that of the continuous phase through a turbulence response coefficient, C_t, (see [56; 5; 111; 6; 2]) in which the correlation proposed by Issa and Oliveira [112] is adopted:

$$C_t = \frac{3 + \beta_t}{1 + \beta_t + 2\rho_d/\rho_c} \tag{3.35}$$

Where: $\beta_t = \dfrac{2\mathbf{A}_d L_\epsilon^2}{\mu_c \mathbf{Re}_t}$; $\mathbf{Re}_t = \dfrac{\mathbf{U}_c^{'} L_\epsilon}{\nu_c}$; $L_\epsilon = C_\mu \dfrac{k^{3/2}}{\epsilon}$; $\mathbf{U}_c^{'} = \sqrt{\dfrac{2k}{3}}$;
Where ν_d and ν_c are respectively the the kinematic viscosity of dispersed and continuous phase. $\mathbf{Re}_t$ is the Reynolds number based on the eddy length scale L_ϵ.

Here the C_{dd} and C_{dc} terms are defined as follow Weller [61]:

$$C_{dd} = (24\nu_c/d_d)(1 + 0.15(\frac{d_d|U_r|}{\nu_d})^{0.687}) \tag{3.36}$$

and

$$C_{dc} = (24\nu_d/d_c)(1 + 0.15(\frac{d_c|U_r|}{\nu_c})^{0.687}) \tag{3.37}$$

Finally, the Reynolds stresses are obtained from the Boussinesq hypothesis [62], which models the turbulent stress-strain relation analogous to the constitutive relation of a viscous fluid. It is given by:

$$\overline{\mathbf{R}}_{\varphi}^{eff} = -\nu_{\varphi}^{eff}(\nabla\overline{\mathbf{U}}_{\varphi} + \nabla\overline{\mathbf{U}}_{\varphi}^{T} - \frac{2}{3}\mathbf{I}\nabla\cdot\mathbf{U}_{\varphi}) + \frac{2}{3}\mathbf{I}k_{\varphi} \tag{3.38}$$

3.2.6 New combination of $k-\epsilon$ models (present contribution)

In order to improve the modelling of the two-phase flows studied in the present thesis, we extend the models proposed by Robert and Oliver [49] and Rusche [56] described above and combine them to take into account both the effect of the interface and the dispersed phase effects. The proposed model is solved and validated through a comparison with the measurements of Buwa and Ranade [134] and Pfleger et al. [18] available in the literature. The following resulting transport equations of turbulence, still based on an extension of the standard $k-\epsilon$ model incorporate the effect of the interfaces and the dispersed phase on the turbulence:

$$\frac{\partial}{\partial t}(\alpha_c k) + \nabla\cdot(\mathbf{U}_c k) = \nabla\cdot(\alpha_c\frac{\nu_c^{eff}}{\sigma_k}\nabla k) + \alpha_c G - \alpha_c\epsilon + \alpha_c\Pi_k^i + \alpha_c\Pi_k^{dis} \tag{3.39}$$

and

$$\frac{\partial}{\partial t}(\alpha_c\epsilon) + \nabla\cdot(\mathbf{U}_c\epsilon) = \nabla\cdot(\alpha_c\frac{\nu_c^{eff}}{\sigma_\epsilon}\nabla\epsilon) + \alpha_c\frac{\epsilon}{k}(C_1 G - C_2\epsilon) + \alpha_c\Pi_\epsilon^i + \alpha_c\Pi_\epsilon^{dis} \tag{3.40}$$

All source terms Π_k^i, Π_ϵ^i, Π_k^{dis} and Π_ϵ^{dis} presented in this model are expressed by the Eqns. (3.17, 3.18, 3.33, 3.34) respectively.

To correct the relative velocity as suggested by Robert and Oliver [49], we take into account the effect of the drift velocity based on the work of Ishii and Zuber [78]:

$$\mathbf{U}_{drift} = \mathbf{U}_r \times \begin{cases} (1-\alpha_d)^{1.75}; & \mu_c >> \mu_d \\ (1-\alpha_d)^{2.00}; & \mu_c \sim \mu_d \\ (1-\alpha_d)^{2.25}; & \mu_c << \mu_d \end{cases} \tag{3.41}$$

In the present work, the first expression under the condition $\mu_c >> \mu_d$ (for air-water system) is used. The effective dynamic viscosity of the continuous phase is calculated in this model as follow [44]:

$$\mu_c^{eff} = \mu_c + \mu^t + \mu_{BIT} \tag{3.42}$$

Where

$$\mu_{BIT} = C_{\mu,BIT}(1-\alpha_d)d_d|U_r| \tag{3.43}$$

3.3 Wall functions

The standard $k-\epsilon$ is a high Reynolds model, therefore because of the way that turbulence is viewed in this framework, it must be completed by wall-functions boundary conditions, to capture approximately the near wall behaviour . So let's come back at the concept of a wall function to see what is the standard formulation for near wall turbulence quantities. In the present study, the standard wall functions based on the proposal of Launder and Spalding [9] are used. They have been most widely used for industrial flows.

The law-of-the-wall for mean velocity yields

$$\mathbf{U}^* = \frac{1}{\kappa}\ln(Ey^*) \tag{3.44}$$

where

$$y^* \equiv \frac{C_\mu^{1/4} k_P^{1/2} y_P}{\nu} \tag{3.45}$$

and κ is the von Karman's constant (= 0.4187, default value in OpenFOAM), E is an empirical constant (= 9 in the present work). In OpenFOAM, the log-law Eqn.(3.44) is employed when the dimensionless coordinate $y* > 11.6$.

In the $k-\epsilon$ model, the k equation is solved in the whole domain including the wall-adjacent cells. The boundary condition for k imposed at the wall is

$$\frac{\partial k}{\partial n} = 0 \tag{3.46}$$

where n is the local coordinate normal to the wall.

The production of kinetic energy, G, and its dissipation rate, ϵ, at the wall-adjacent cells, which are the source terms in the k equation, are computed on the basis of the local equilibrium hypothesis. Under this assumption, the production of k and its dissipation rate ϵ are assumed to be equal in the wall-adjacent control volume.

Thus, the production of k is computed from

$$G = \frac{\nu_L \mathbf{U}_P C_\mu^{1/4} k^{1/2}}{\kappa y_P} \tag{3.47}$$

and ϵ is computed from

$$\epsilon_P = \frac{C_\mu^{3/4} k_P^{3/2}}{\kappa y_P} \tag{3.48}$$

Here y_P, $\mathbf{U}_P$, k_P denotes respectively the distance from point P to the wall, the mean velocity at the point P, and the kinetic energy at the point P.

The standard wall functions described so far are provided as a default option in OpenFOAM. The standard wall functions work reasonably well for a broad range of wall-bounded flows.

3.4 Boundary Conditions

The numerical representation of the boundary conditions used with the two-fluid methodology is very similar to the practice used for laminar single-phase flow Hill [36]. However, two issues require further discussion here: the pressure boundary condition at a no-slip impermeable wall and near-wall turbulence.

3.4.1 Pressure Boundary Condition at Walls

In single-phase flow the dynamic pressure gradient at the wall is specified to be zero, implying that the pressure gradient at the wall equals ρg. In the two-fluid methodology, difficulties arise from the fact that the system is modelled in such a way that it has only a single pressure, but two fluids with possibly very different densities.

In general, the specification of pressure boundary conditions depends on the exact definition of pressure. In incompressible flow calculations, the pressure is often modified to remove possibly steep gradient arising from hydrostatic effects as well as simplifying the specification of the wall pressure boundary condition. This route is adopted here, and we define a modified mixture pressure as follows Rusche [56]:

$$\overline{p}^{\star} = \overline{p} - \rho_c \mathbf{g} \cdot \mathbf{x} \tag{3.49}$$

where ρ_c is the density of the heavier phase and x is the position vector.

3.4.2 Near-wall Turbulence

The behaviour of turbulence near walls is considerably different from that in the other parts of the flow. It is therefore necessary to use appropriate modelling in the near-wall region. In

Table 3.3: Numerical boundary conditions applied in this study.

Variable	Wall	Inlet	Outlet
$\vec{\mathbf{U}}_d$	Fixed Value	Fixed Value	Zero Gradient
$\vec{\mathbf{U}}_c$	Fixed Value	Fixed Value	Zero Gradient
α_d	Zero Gradient	Fixed Value	Zero Gradient
p	Zero Gradient	Zero Gradient	Fixed Value
k	Fixed Value	Fixed Value	Zero Gradient
ϵ	Fixed Value	Fixed Value	Zero Gradient

this study, the near-wall region of high gradients is used by using the so-called wall-function approach by Launder and Spalding [9] (see section 3.3), which creates an additional term in the momentum equation in order to compensate for the increased shear stress at the wall. The additional drag is treated as a change in the effective viscosity at the **wall face**, carrying the difference between the assumed linear and the logarithmic velocity profile between the cell centre and the wall. For the k and ϵ transport equations, the situation is somewhat different: wall-functions use the local equilibrium assumption and prescribe the generation of k and the value of ϵ in the near-wall cell. Until now, the validity of the wall-function approach is not known for multiphase flows.

Following Politis [122], it is assumed that the effects of the second phase on the turbulent boundary layer are adequately accounted for by including the phase fraction to account for the effective reduction of the wall surface area in contact with the considered phase.

3.5 Summary of Boundary Conditions

In this study, the following types of boundary conditions are used and the corresponding numerical boundary conditions for each variable are summarized in Table 3.3:

Inlet The velocity fields at the inlet are supplied and, for consistency, the boundary condition on the modified pressure is zero gradient. In addition, fixed value conditions for the dispersed phase fraction, the turbulence kinetic energy as well as its dissipation rate are specified.

Outlet The modified pressure field at the outlet is supplied and a zero gradient boundary condition on velocity is specified. Furthermore, zero gradient boundary conditions are applied to the dispersed phase fraction, turbulence kinetic energy as well as its dissipation rate.

Walls The velocities of the fluids are equal to that of the wall, i.e. a fixed value condition is specified. The dynamic pressure is specified to be zero gradient since the flux through the wall must be zero. Zero gradient boundary conditions are also used for the additional scalars if appropriate.

3.6 Closure

In this chapter, several models of turbulence were presented, analyzed and discussed. First, the standard $k - \epsilon$ for single phase was presented, then the extended models of Robert and Oliver [49] and Rusche [56] for multiphase flow are detailed. Finally, a new combination of these models is developed and integrated to incorporate both the effect of the bubble dispersion and the interface gas-liquid on the turbulence behaviour.

Chapter 4

Population Balance Modelling

In general, fluid flow where the use population balance equation can be used is encountered in several engineering disciplines. It is used to study bubbly flow, particle size distribution (PSD) of plasma, polymerization etc. As analytical solution of population balance equation are available in a very few cases, numerical techniques are essential in most practical applications. Such techniques are sought to be accurate and with a relatively low computational cost. There are several numerical methods available that satisfy the accuracy requirement. Among them are the Monte Carlo Method [82; 20], the method of classes (CM) [113; 85; 68; 117; 118; 83; 20], the quadrature method of moments (QMOM) [107; 108; 33] the direct quadrature method of moments (DQMOM) [105; 31].

4.1 Background

In the last decade, an increasing number of studies has been made on the modeling of bubbly flow using advanced computational fluid dynamics methods (CFD). These studies often involved experimental work aimed at identifying the hydrodynamic behaviour, heat and

mass transfer, flow regime and mixing behaviour in these bubble columns. The importance of chemical processing technologies involving bubbly reacting flows brings sustained interest in fundamental studies of the hydrodynamics and flow regime for better reactor design and operation. Among the important models of the gas-liquid flows in bubble columns [103; 1; 17; 93; 95; 21], most of these represent the bubbles with a single uniform size (one bubble size model). However, recently Buwa and Ranade [133] have shown different dynamic characteristics for different bubble sizes. It appears more and more that it is essential to represent the dispersed phase taking into account its bubble size distribution and taking in consideration the coalescence and break-up processes to model the bubble size evolution. A few authors have included a population balance equation to describe the bubbles behaviour. For example [120; 47; 44; 45]. They solve mass and momentum conservation equations for all bubble groups (multi-fluid model). The coalescence and break-up processes are accounted for by solving continuity equation for all bubble classes. For some types of bubbly flows [47; 44] have assumed equilibrium between the coalescence and break-up processes transforming the population balance model to a single equation. However, in bubble columns this assumption may be not applicable because of the significant influence of convection.

Several authors have used different models (multi-fluid model) to calculate coalescence and break-up rates and probabilities of bubble collisions [86; 55; 47]. The solution of population balance equations for multi-fluid model has been receiving, as a consequence of the interest in bubbly flows, increasing attention. The original work of von Smoluschowski was published over 92 years ago (1917), it has the following form:

$$\frac{dn_j}{dt} = \frac{1}{2}\sum_{i+k=j} K_{ik} n_i n_k - n_j \sum_i K_{ij} n_j \tag{4.1}$$

Here, the first right hand term represent the formation of j-mother particles due to binary collisions between i and k primary particles. The second term is the birth rate of j-mother particles due to aggregation. Since 1971, many solutions were proposed for solving population

balance equation. For example [19; 114; 99; 88; 30; 140; 76; 89; 117; 118; 70].

Attempts have been made to solve the population balance equation using the so-called quadrature method of moments (QMOM) first proposed by McGraw [107]. It has proved an efficient and successful technique, for example, for describing aerosol dynamics under conditions that can include new particle formation, evaporation, growth and coagulation. In the case of bubble size distribution in bubble columns, the dispersed phase tends to break-up or coalesce due to presence of complex fluid mechanical mechanisms present in bubbly flows. The break-up occurs according to two mechanisms, the first is when turbulent eddies strike the bubble surface with sufficient energy, and the second is the break-up of large bubbles, due to their structural instability. The coalescence occurs when two bubbles or more collide because of velocity difference and/or because of turbulence.

There are numerous challenges in modelling dispersed flows because of the exchange of momentum between particles due to collision, and the changes of particles properties due to break-up and aggregation. The problem is carried out on the coupling of PBE to the solution of the multiphase fluid mechanics equations, using CFD. An important technical limitation of this coupling is the extra computational effort for PBE solution, such as classical methods (Monte Carlo, sectional and Classes methods). Therefore, very efficient and accurate numerical methods are developed for solving PBE with more computational efficiency .

The Direct Quadrature Method Of Moments (DQMOM) [32] is one of the most efficient methods, it was inspired by the Quadrature Method Of Moments (QMOM) first developed by McGraw [107]. The main advantage of DQMOM/QMOM is that few abscissas are necessary to describe the particle size distribution due to quadrature approximation closure. In the present work, DQMOM is applied to the PBE-CFD modelling of polydispersed gas-liquid bubble columns using the OpenFOAM CFD package. Besides the PBE-CFD coupling, another challenge on the modelling of multiphase flows is the breakage and coalescence phe-

nomena. At the present, the current available breakup and aggregation models for gas-liquid flows are not completely adequate, For example, a bubble column model must consider several phenomena as turbulence, bubble induced turbulence, momentum interface exchange forces (drag, lift, virtual mass, gravity,. drift velocity,..), wall viscosity, PBE with breakage and aggregation models. In the present work, we focus on the validation of the DQMOM with the CM and with experimental data available in the literature. Some preliminary comparisons of predicted Sauter mean diameter (d_{32}), volume mean diameter, and mass transfer coefficient (kla) and experimental measurements are included.

4.2 Definition

In practical bubbly flow applications, bubbles can break or coalesce due to bubble-bubble and bubble-fluid interactions. Under this assumption, a fixed bubble size model might not be suitable for predicting correct multiphase flow behaviour in the gas-liquid system. So, if breakage and coalescence events produce very different bubble size distribution, it may affect the interfacial interactions between the phases as well as heat and mass transfer, or momentum i.e. drag and lift forces. As analytical solutions of population balance equation are available in very few cases, numerical techniques become essential to resolve this problem. There are several numerical methods available in the scientific literature that satisfy the required precision. Among them are the Monte Carlo Method (Smith1998b, Ramkrishna2000), the Method of Classes [117; 118; 83], the Quadrature Method of Moments [107; 33], the Direct Quadrature Method of Moments Rong et al. [48].

4.3 Population Balance Equation solution methods

Analytical solution of population balance equation are available in a very few cases (see for example [37]), then the numerical solutions are essential in most practical applications. Such techniques are sought to be accurate and with a relatively low computational cost. The most commonly technique used to solve PBE is the Method of Classes (CM) which require 12-15 classes to achieve a good accuracy Vanni [83]. Using only few nodes (2-4) for the QMOM and DQMOM reach comparable accuracy with the CMs.

The first attempt to couple CFD and PBE was the MUSIG (MUlti-Size Group) model used by Lo [120]. It is based on a two-fluid model formulation where the secondary phase accounts for all classes of the bubble size distribution. The limitation of the MUSIG model stems form its incapability to predict the dynamics of different classes. Kumar and Ramkrishna (1996) used a fixed pivot approach to discretize the PBE in the domain. This technique is known as the method of classes (CM) and is today the most commonly used technique for solving PBE.

McGraw [107] introduced into CFD the concept of moments to solve the population balance. The method of moments (MOM) is a powerful approach for describing, for example, aerosol dynamics under conditions that can include new particles formation, evaporation, nucleation and growth, condensation, coagulation and complex mixing flows [107; 46; 84].

Marchisio et al. [33] introduced a new efficient numerical technique to solve PBE, the quadrature method of moments (QMOM), which was developed by McGraw [107]. Furthermore, Marchisio et al. [31] have developed an original technique, the direct quadrature method of moments (DQMOM), which is particularly suited for CFD applications. A review of population balance methods applicable to CFD can be found in Jakobsen et al. [58].

4.3.1 Method of Classes "CM"

By definition, the population balance equation (PBE) is the conservation equation of the number n_i of the bubbles (per unit volume) of size i. Luo and Svendsen [55] was the first to use computational fluid dynamics methods coupled with the population balance model. In the literature, there are several numerical methods for solving PBE using CM technique. In this study, the fixed pivot approach of Ramkrishna and Kumar [20; 117; 118] is used which assumes that the population of bubbles is distributed on pivotal grid points x_i with $x_{i+1} = sx_i$ and $s > 1$. The main advantage of CM is that bubble size distribution is explicitly known.

Population balance using CM

In order to solve the PBE coupled to the full flow problem, the CM method with bubble classes is implemented in the OpenFOAM CFD code. The Population Balance Equation for the i th bubble class can be written for constant density (Chen et al. [95; 96]) as:

$$\frac{\partial}{\partial t}(\rho_d n_i) + \nabla \cdot (\rho_d \mathbf{U}_{d,i} n_i) = \rho_d S_i \tag{4.2}$$

Where n_i is the number density of class i, S_i represent the term source due to the bubbles coalescence and break-up given by:

$$S_i = (B_i^{coal} - D_i^{coal}) + (B_i^{break} - D_i^{break}) \tag{4.3}$$

Here, B_i^{coal} and D_i^{coal} are the birth and death rates due to coalescence. B_i^{break} and D_i^{break} are the birth and death rates due to bubbles break-up.

The number density n_i is related to the individual bubble volume through the gas volume fraction as follows:

$$n_i = \frac{\alpha_i}{v_i} \tag{4.4}$$

v_i and α_i are respectively the volume and gas volume fraction of class i. The sum of the bubble group volume fractions is indeed the volume fraction of the dispersed phase:

$$\sum_i \alpha_i = \alpha_d \tag{4.5}$$

Each individual size group volume fraction is then expressed in terms of the total dispersed phase fraction as follows:

$$f_i = \frac{\alpha_i}{\alpha_d} \tag{4.6}$$

with

$$\sum_i f_i = 1 \tag{4.7}$$

f_i is the bubble volume fraction of group of size i. S_i is the source term due to coalescence and break-up. Several bubble coalescence and break-up models have already been implemented in the CFD package OpenFOAM for bubbly flows.

Eqn. (4.2) can be rewritten using the scalar f_i and the Eqn. (4.3)

$$\frac{\partial}{\partial t}(\alpha_d \rho_d f_i) + \nabla \cdot (\alpha_d \rho_d \mathbf{U}_d f_i) = \rho_d v_i([B_i^{coal} - D_i^{coal}] + [B_i^{break} - D_i^{break}]) \tag{4.8}$$

It is important to note the important difference between Eqn. (4.2) and Eqn. (4.8). In the Eqn. (4.2), the individual bubble velocity is used. On the other hand, in the Eqn. (4.8), the same gas velocity is used for all bubble sizes. For practical reasons, Eqn. (4.8) is often preferred. This is mainly justified because the global computational effort is lower than when using the second approach (see Eqn. (4.2)). In this work, the population balance equation chosen has the form of a transport equation of a scalar variable f_i and is solved using the CFD tools OpenFOAM. The interfacial exchange forces coupling is done via the Sauter mean diameter (d_{32}):

$$d_{32} = \frac{\sum_i f_i}{\sum_i (f_i/d_i)} \tag{4.9}$$

The Sauter mean diameter is a common measure in fluid dynamics as a way to estimate the average particle size. It was originally developed by German scientist, J. Sauter in the late 1920s. It is defined as the diameter of a sphere that has the same volume/surface area ratio as a particle of interest. Sauter mean diameter is especially important in calculations where the active surface area is important. Such areas include bubbles dispersion, catalysis and applications in fuel combustion.

Discretization of PBE by the method of classes (CM)

As mentioned above, to discretize the PBE in the domain, the fixed pivot approach of Kumar and Ramkrishna (1996) is used. This technique is known as the Class Method (CM) and is today the most commonly used technique for solving PBE. The CM assumes that population bubbles is distributed on pivoted grid points x_i where $x_{i+1} = sx_i$ and $s > 1$. Bubble break-up and coalescence may generate new bubbles with volume v such that $x_i < v < x_{i+1}$. This bubble must be split by assigning respectively fraction γ_i and γ_{i+1} to x_i and x_{i+1}. In this method, the number density (zeroth moment) and mass conservation (first moment) are preserved by prescribing the following two constraints Kerdouss et al. [45]:

$$\begin{cases} \gamma_i x_i + \gamma_{i+1} x_{i+1} = v \\ \gamma_i + \gamma_{i+1} = 1 \end{cases} \tag{4.10}$$

Following Kumar and Ramkrishna [117], the terms of birth rates B_i^{coal} due to coalescence (Eqn.4.3) is given by:

$$B_i^{coal} = \sum_{k=0}^{n}\sum_{j=0}^{n}\left[\theta(x_{i-1} < x_j + x_k < x_i) \times \left(1 - \frac{1}{2}\delta_{jk}\right)\right] \times (\gamma_{i-1}(x_j + x_k)a(x_k, x_j)n_j n_k)$$
$$+ \sum_{k=0}^{n}\sum_{j=k}^{n}\left[\theta(x_i < x_j + x_k < x_{i+1}) \times \left(1 - \frac{1}{2}\delta_{jk}\right]\right] \times (\gamma_i(x_j + x_k)a(x_k, x_j)n_j n_k)$$

where θ is a test function defined as

$$\theta(test) = \begin{cases} 0 & test\ is\ false \\ 1 & test\ is\ true \end{cases} \tag{4.11}$$

and

$$\gamma_{i-1}(v) = \frac{v - x_{i-1}}{x_i - x_{i-1}};\ \gamma_i(v) = \frac{x_{i+1} - v}{x_{i+1} - x_i}$$

The death rates D_i^{coal} in class i due to coalescence

$$D_i^{coal} = n_i \sum_{k=0}^{n} a(x_i, x_k) n_k \tag{4.12}$$

The birth rate B_i^{break} in class i due to breakup

$$B_i^{break} = \sum_{k=i}^{n} m(x_k) b(x_k) n_k \pi_{i,k} \tag{4.13}$$

The death rate D_i^{break} in class i due to breakup

$$D_i^{break} = b(x_i) n_i \tag{4.14}$$

where

$$\pi_{i,k} = \int_{x_{i-1}}^{x_i} \frac{v - x_{i-1}}{x_i - x_{i-1}} p(v, v_k) dv + \int_{x_i}^{x_{i+1}} \frac{x_{i+1} - v}{x_{i+1} - x_i} p(v, v_k) dv \tag{4.15}$$

The above integrals are approximated by the Gaussian quadrature integration as follows:

Table 4.1: Values of weighting function used in Gaussian quadrature integration

W_1	W_2	W_3	$W_4 = -W_2$	$W_5 = -W_1$
$\sqrt{\frac{35+2\sqrt{70}}{63}}$	$\sqrt{\frac{35-2\sqrt{70}}{63}}$	0.0	$-\sqrt{\frac{35-2\sqrt{70}}{63}}$	$-\sqrt{\frac{35+2\sqrt{70}}{63}}$

$$\pi_{i,k} \simeq \sum_{j=1}^{5} \frac{(1+W_j)^3}{(j+1)^2 P_5^2 P(W_j)} P\left(\frac{x_i - x_{i-1}}{2}(1+W_j) - x_{i-1}, x_k\right) + \sum_{j=1}^{5} \frac{(1+W_j)^2(1-W_j)}{(j+1)^2 P_5^2 P(W_j)} P\left(\frac{x_{i+1} - x_i}{2}(1+W_j) - x_i, x_k\right) \tag{4.16}$$

P_n is a Legendre polynomial which can be constructed using the three term recurrence relation:

$$P_n = \frac{(2n-1)xP_{n-1} - (n-1)P_{n-2}}{n}; \quad P_0 = 1; \quad P_1 = x \tag{4.17}$$

W_j is the weighting function related to the orthogonal polynomials, in this case as shown in Table4.1. $j = 5$ this number gives good accuracy.

4.3.2 Method Of Moments "MOM"

The method of moments solves the problem by tracking the time evolution of the first lower-order of moments. These lower-order moments are often sufficient to describe the physical properties of particles (e.g size distribution) [107; 46; 84]. Generally, the k^{th} moments of particles (or bubbles) size distribution is defined as:

$$m^{(k)} = \int L_k f(L) dL \tag{4.18}$$

where $f(L)$ is the distribution function for the number density of particles of size L. k is the moment-order. The key of the MOM is that the lower-order moments (generally the first 6

moment-order) can be tracked directly without requiring additional knowledge of the initial distribution. This method has been losing interest because the closure requirements are very severe and depends upon the choice of the first lower-order of moments.

4.3.3 Quadrature Method Of Moments "QMOM"

The QMOM is a more recent approach of the MON introduced by McGraw (1997) for solving population balance equation. In this method, the moments of the number density function f are tracked in time directly, and the analytic closure of MOM is replaced by an approximate closure condition which is a numerical quadrature (e.g Gauss, Laguerre, Lagrange,...) and therefore is called quadrature method of moments. Still, the QMOM is based on the idea of solving the population balance equation in terms of the moments which is defined as follows [32]:

$$m^{(k)}(t) = \int_0^{+\infty} n(\xi;t)\xi^k d\xi \tag{4.19}$$

where ξ and $n(\xi;t)$ are respectively a single internal coordinate and a number density function (NDF). Some of the moments of the NDF have specific physical meanings, for example the zeroth moment represents the total number particles per unit volume. The second and third moments are respectively related to the total particles surface area and total particles volume through the following relationship:

$$A_{total} = k_A m^{(2)} \tag{4.20}$$

$$V_{total} = k_V m^{(3)} \tag{4.21}$$

where k_A and k_V are the surface and volume shape factors. We can also define directly from the moments different particles properties, for example the Sauter mean diameter d_{32} and the volume mean diameter d_{43} as follows:

$$d_{32} = m^{(3)}/m^{(2)} \tag{4.22}$$

and

$$d_{43} = m^{(4)}/m^{(3)} \tag{4.23}$$

Now, if we applied the moment transform to PBE, the following equation is obtained:

$$\frac{\partial m^{(k)}(t)}{\partial t} + \nabla \cdot (\mathbf{U}^{(k)} m^{(k)}) = S^{(k)} \tag{4.24}$$

where $S^{(k)}$ is the source term of moment of order k and $\mathbf{U}^{(k)}$ is the k^{th} moment velocity defined as:

$$\mathbf{U}^{(k)} = \frac{\sum_{i=1}^{N} u(L_i) w_i L_i^k}{\sum_{i=1}^{N} w_i L_i^k} \qquad k = 0, ..., 2N-1 \tag{4.25}$$

The focus of the QMOM is to approximate the integral equation Eqn. (4.19) by means of n-point Gaussian quadrature as follows:

$$m^{(k)}(t) = \int_0^{+\infty} n(\xi; t) \xi^k d\xi \approx \sum_{i=1}^{n} L_i(t)^k w_i(t) \tag{4.26}$$

where N is the node of quadrature approximation (in general 3 nodes gives good results). $L_i(t)$ and $w_i(t)$ are the abscissas and weights of the quadrature. However, the direct solution of Eqn. (4.26) is not recommended and requires a costly nonlinear search. A better approach is to use the moment sequence to construct a tridiagonal Jacobi matrix from which the quadrature abscissas and weights can be obtained using product-difference algorithm (PDA). This algorithm is described in appendix A.

4.3.4 Direct Quadrature Method of Moments "DQMOM"

The DQMOM method is based on the direct solution of the transport equations for weights and abscissas of the quadrature approximation Rong et al. [48]. The advantage of this method is that it is directly applicable to the PBE with more than one internal coordinate. Thus, the DQMOM offers a good approach for describing bubble size distribution undergoing

break-up and coalescence processes in the context of CFD-bubble flow modeling. Since this method has been described extensively by many authors recently, the discussion is limited here to a brief review of the equations. The transport equations for calculating the weights and abscissas are written as:

$$\begin{cases} \dfrac{\partial}{\partial t} w_i + \nabla.(\mathbf{U} w_i) = a_i \\ \dfrac{\partial}{\partial t} L_i + \nabla.(\mathbf{U} L_i) = b_i \end{cases} \tag{4.27}$$

where a_i and b_i are found by the solution of the following linear system in the unknowns a_i and b_i [7]:

$$\sum_{i=1}^{N} \left[(1-k) L_i^k a_i + k L_i^{k-1} b_i \right] = S^{(k)} \qquad k = 0, ..., 2N-1 \tag{4.28}$$

This system is numerically solved using the Gauss-Seidel method. The source term $S^{(k)}$ is defined as follows:

$$S^{(k)} = (B_{coal}^{(k)} - D_{coal}^{(k)}) + (B_{break}^{(k)} - D_{break}^{(k)}) \tag{4.29}$$

where $B_{coal}^{(k)}$ and $D_{coal}^{(k)}$ are the k^{th} birth and death rates due to coalescence, and $B_{break}^{(k)}$ and $D_{break}^{(k)}$ are the k^{th} birth and death rates due to break-up of bubbles and its formulation are Rong et al .[48]:

$$B_{coal}^{(k)} = \frac{1}{2} \sum_{i=1}^{N} \sum_{j=1}^{N} \omega_i \omega_j \left(L_i^3 + L_j^3 \right)^{k/3} \beta_{ij} \tag{4.30}$$

$$D_{coal}^{(k)} = \sum_{i=1}^{N} \sum_{j=1}^{N} \omega_i \omega_j L_i^k \beta_{ij} \tag{4.31}$$

$$B_{break}^{(k)} = \sum_{i=1}^{N} \overline{b}_i^{(k)} a_i^{\star} \omega_i \tag{4.32}$$

$$D_{break}^{(k)} = \sum_{i=1}^{N} \omega_i L_i^k a_i^{\star} \tag{4.33}$$

where $\beta_{ij} = \beta(L_i, L_j)$, $a_i^* = a(L_i)$, and $\overline{b}_i^{(k)} = \int_0^\infty L^k b(L/L_i) dL$.

The above integrals of the daughter distribution function $\overline{b}_i^{(k)}$ is approximated as:

$$\overline{b}_i^{(k)} \approx L_i^k \frac{m^{k/3} + n^{k/3}}{(m+n)^{k/3}} \tag{4.34}$$

where m and n represent the mass ratios between the two bubble breakage. For example, if $m = 1$ and $n = 1$, the two fragments have the same volume and thus, symmetric breakage is considered. In the present work, a symmetric breakage is considered ($m = n = 1$) and if we applied Eqn. (4.34) the following relation is obtained:

$$\overline{b}_i^{(k)} \approx 2^{(3-k)/3} L_i^k \tag{4.35}$$

Here L_i denotes the characteristic length of the bubble and it is taken to be equivalent to the bubble diameter of class i. The breakage kernel $a(L_i)$ can be formulated by using the Eqn. (5.4) addressed in the next section.

In the present study, the direct quadrature method of moments is adopted, mainly because it is a computationally attractive and accurate alternative. It is based on the idea of directly tracking the weights and abscissas of the quadrature approximation rather than resorting on the product algorithm PDA used in the simple quadrature method of moments.

4.4 Closure

We have described the basis of population balance equation modelling adopted in this study. First, a background of population balance modelling was presented, followed by a short definition of number density function. Next, some numerical solution procedures were discussed. We note here that the source terms of coalescence and breakage have been included in the population balance equation as additives. Concerning the breakage phenomena, it has often been described by combining the collision frequency between the bubbles and the turbulent

eddies and the probability at which the collision leads to the breakage. Common assumptions of breakage models are that the turbulence is isotropic, and particles can break due to collisions with smaller or equal-sized eddies with enough energy. Hence, the coalescence term is generally described by combining the frequency of bubble-bubble collisions and the efficiency of coalescence. In many studies and also here, turbulence is considered as the dominant mechanism for the collisions (Coulaloglou and Tavlarides [15], Tsouris and Tavlarides [14], Venneker et al. [8]). Coalescence efficiency has commonly been described as the film drainage process between the collided bubbles (Fig. 5.2). .

Chapter 5

Bubble coalescence and break-up models

Bubble coalescence and break-up phenomena have attracted considerable attention in the last decades in reactor design and operations, aerated beds in bubble column, stirred tank reactors and bioreactors, mainly because gas-liquid contact area is one of the key parameters in mass transfer. When bubbles coalesce or break-up the contact area change and mass transfer decreases and/or increase. Bubble size distribution is a result of bubble formation, bubble coalescence and break-up due to the turbulence, gas-liquid velocities difference and the instability of the large bubbles. For these reasons it is important to predict bubble coalescence and breakage in order to prevent low yields in reactors and to increase the efficiency of chemical process and allow us a better choice of multiple design.

5.1 Bubble break-up models

In the present section, we describe the bubble break-up functions. Break-up tends to occur when shear forces in the liquid are large enough to overcome the surface tension of the bubbles (Fig. 5.1). In this work. the model of Luo and Svendsen [55] is adopted. Breakup of bubbles in a turbulent flow occurs when turbulent eddies, with an energy higher than the bubble surface energy hit the bubble surface. For bubble breakup to occur, the sizes of the bombarding eddies have to be smaller than or equal to the bubble size. The model assumes that breakup is binary and that the turbulent breakup mechanism can be modelled as the product of breakup probability due to the energy contained in eddies and a collision frequency between bubbles and turbulent eddies.

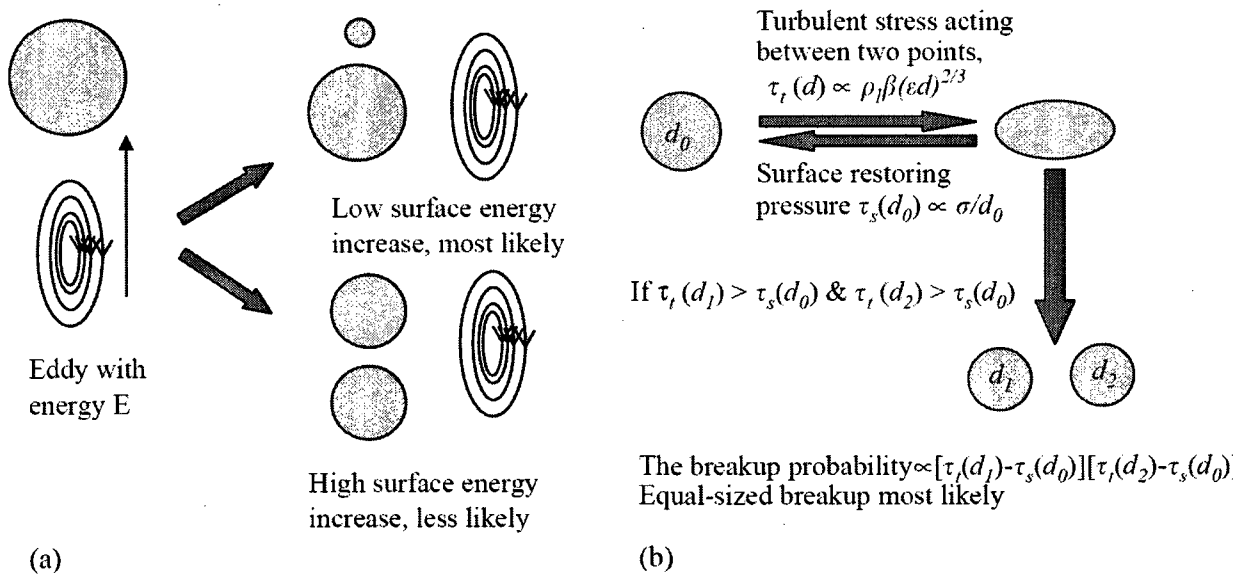

Figure 5.1: Bubble breakup illustration (a) Luo and Svendsen [55], (b) Martínez-Bazán et al. [12]

5.1.1 Break-up model by Luo and Svendson (1996)

The bubble break-up can be related to the influence of small turbulent eddies on the bubble surface [123; 55; 47]. The model of Luo and Svendsen [55] has served as a basis for many of the studies published after 1996. It is derived from theories of isotropic turbulence. We use the break-up model of Luo and Svendsen [55] which is based on the idea that break-up occurs when the eddy of higher energy hits the bubble surface. Hence, the break-up frequency is related to the frequency of collision of small eddies with the bubble and is given by Bhole et al. [90]:

$$\Omega_B(v_i : v_j) = 0.923\alpha_L N_i \left(\frac{\epsilon}{d_i^2}\right)^{1/3} \int_{\zeta_{min}}^{1} \frac{(1+\zeta)^2}{\zeta^{11/3}} Exp\left(-\frac{12 c_f \sigma}{2\rho_L \epsilon^{2/3} d_i^{5/3} \zeta^{11/3}}\right) d\zeta \qquad (5.1)$$

The Eqn. (5.1) gives the break-up frequency for the breakage of bubble of volume i into a bubble of volume j. The increase energy in the surface area is given by:

$$c_f = f_{BV}^{2/3} + (1 - f_{BV})^{2/3} - 1 \tag{5.2}$$

where $f_{BV} = v_j/v_i$ and ζ is the dimensionless eddy size (the ratio of eddy size to the bubble size). The minimum eddy size can be calculated from $\zeta_{min} = 11.4\zeta_d$ with $\zeta_d = (\frac{\nu_c^3}{\epsilon})^{1/4}$ which is the Kolmogoroff micro scale. In this model no probability density is needed and the break-up rate function can be calculated by using incomplete gamma functions in the following form ([45; 102]):

$$\Omega_B(v_i : v_j) = -\frac{18}{11}\frac{0.923\alpha_L\alpha_G f_j}{\pi b^{8/11} d_j^3}\left(\frac{\epsilon}{d_j^2}\right)^{1/3}(\Gamma(8/11, t_m) - \Gamma(8/11, b) \tag{5.3}$$
$$+2b^{3/11}(\Gamma(5/11, t_m)\Gamma(5/11, b)) + b^{6/11}(\Gamma(2/11, t_m) - \Gamma(2/11, b)))$$

where

$$b = \frac{12 c_f \sigma}{2\rho_L \epsilon^{2/3} d_j^{5/3}} \tag{5.4}$$

and

$$t_m = b(\zeta_{min}/d_j)^{-11/3} \tag{5.5}$$

At high Reynolds number, terms with t_m in the incomplete Gamma function are taken equal to zero as $t_m \simeq \infty$ Chen et al. [94].

5.1.2 Break-up model by Wu et al. (1998)

Following Wu et al. [100], an expression inspired from the kinetic theory of gases can be written for bubble break-up rate when $We > We_{crit}$. In this model, a single distribution function of particle sizes is assumed, thus only a single scalar transport equation is required for the overall number density distribution. This model, using a single local bubble size, does

not address the full complexity of such a complex process, where a local size distribution obviously exists. The predictions of this model include the distribution of bubble sizes n, based on the mechanisms for break-up described in this section and the coalescence described later, is related to the gas holdup α_d and the average bubble size d by:

$$n = \frac{\alpha_d}{(\pi/6)d^3} \tag{5.6}$$

From the values of n at each cell in the grid mesh, the local average bubble size d can be calculated and so is the drag coefficient C_D. The conservation equation of bubble number density can be written as (Lane et al., 2002; Wu et al., 1998):

$$\frac{\partial}{\partial t}(\alpha_d \rho_d n) + \nabla \cdot (\alpha_d \rho_d \vec{\mathbf{U}}_d) = \rho_d (S_{br} - S_{co}) \tag{5.7}$$

S_{br} and S_{co} are respectively the rates of bubble breakage and coalescence. Turbulence is the primary mechanism responsible for break-up and only the small eddies can break the bubbles, while the large ones transport the bubbles. The bubble break-up rate is considered to depend on the frequency of collisions between bubbles and eddies and can occurs only when the Weber number We exceeds a critical value ($W_{crit} = 1.2$). The Weber number is given by:

$$\frac{\rho_c u_t^2 d}{\sigma} \tag{5.8}$$

where u_t is the turbulent velocity of eddies, and is given by:

$$u_t = 1.4(\epsilon d)^{1/3} \tag{5.9}$$

Following Wu et al. (1998) an expression inspired from the kinetic theory can be written for bubble break-up rate when $We > We_{crit}$:

$$S_{br} = C_{br} n \frac{(\epsilon d)^{1/3}}{d} \left(1 - \frac{We_{crit}}{We}\right)^{1/2} Exp\left(-\frac{We_{crit}}{We}\right) \tag{5.10}$$

C_{br} is an adjustable model parameter that has to be evaluated by calibration with experimental data , it is set to 0.02.

5.1.3 Break-up model by Martínez-Bazán et al. (1999)

As an other option, the considered phenomenological model (see Fig. (5.1)-(b)) for bubble breakup frequency proposed by Martínez-Bazán et al. [12; 13] is illustrated in this section. This model is based on the turbulence stress and surface tension and was validated with experimental data. According to this model:

$$\Omega_B(\epsilon, d_i) = K_g n_i \sqrt{\frac{\beta(\epsilon d_i)^{2/3} - 12\sigma/(\rho_c d_i)}{d_i}} \tag{5.11}$$

where the constant $\beta = 8.2$ was given by Batchelor [51], and $K_g = 0.25$ was found experimentally by Martínez-Bazán et al. [12].

5.1.4 Break-up model by Lehr (2001)

An alternative model of Lehr and Mewes [47] was developed for breakage phenomena. It is tested as an alternative to the previously presented models. Both the model of Lehr and Mewes [47] and model of Chen et al. [95] have been shown to predict bubble size distribution function successfully in bubbly flows.

In Lehr's model the breakage frequencies are calculated as:

$$\Omega_B(L_i) = \frac{1}{2} \frac{L_i^{5/3} \rho_c^{7/5} \epsilon^{19/15}}{\sigma^{7/5}} exp\left(- \sqrt{2} \frac{L_i^3 \epsilon^{6/5} \rho_c^{9/5}}{\sigma^{9/5}} \right) \tag{5.12}$$

5.2 Bubble coalescence models

The coalescence phenomena occurs when bubble collide with each other in a turbulent environment (Fig. 5.2). There are various mechanisms of bubble coalescence. Prince and Blanch [86] have considered three mechanisms of bubble collision: Bubble can collide due to the random motion in a turbulent flow, due to the different rise velocity, and due to the mean shear in the flow field Bhole et al. [90].

Mathematically, the coalescence rates Ω_C $(m^3 s^{-1})$ is usually written as the product of collision rate θ_{ij} $(m^3 s^{-1})$ and coalescence efficiency P_c (or some times applied probability as defined by Hagesather et al. [75]) The figure 5.2 show the coalescence model of Prince and Blanch [86]. This model is based on the drainage between deforming drops with immobile surfaces and the initial film thickness and the critical film thickness are assumed constant.

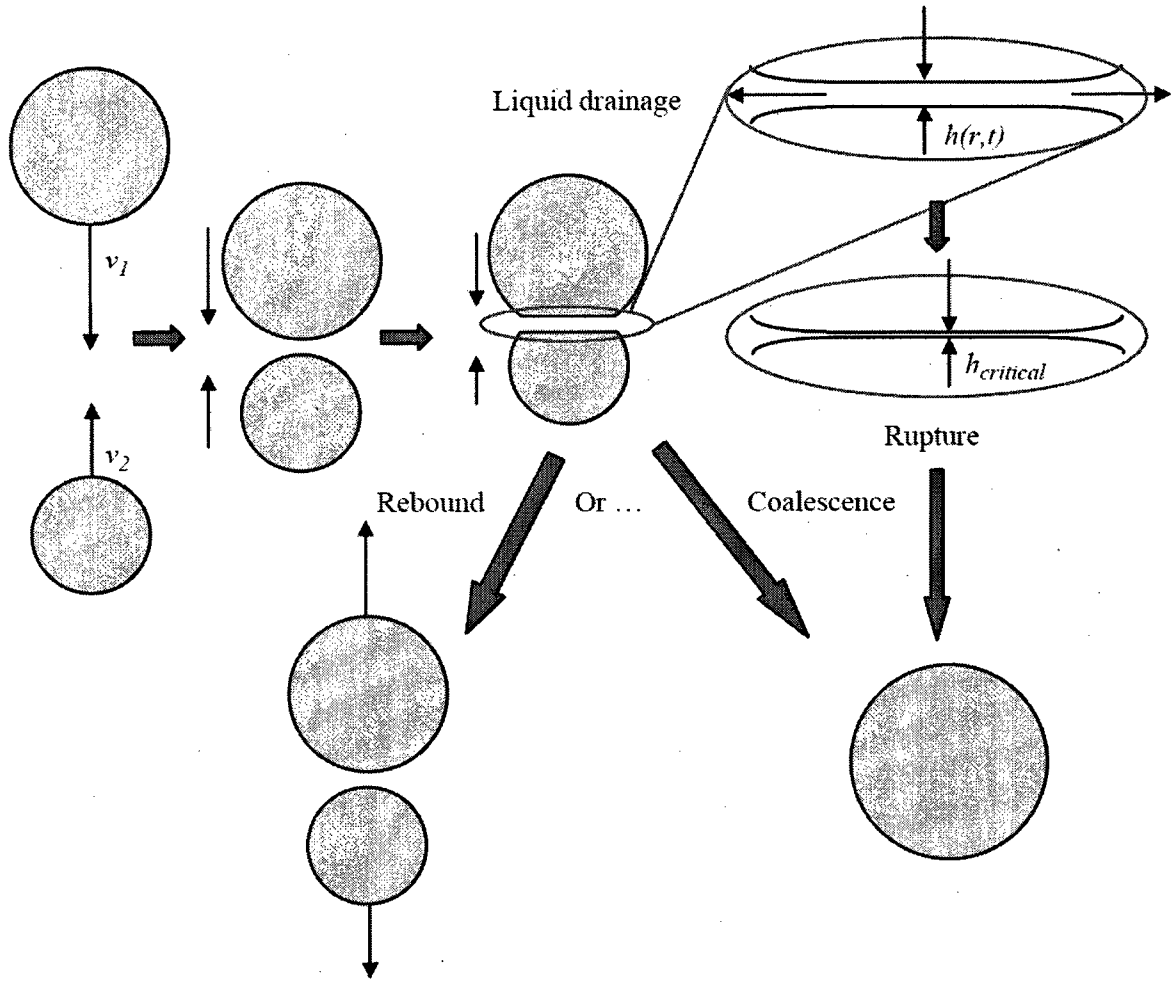

Figure 5.2: Bubble coalescence in turbulent flow

5.2.1 Coalescence model by Prince and Blanch (1990)

Prince and Blanch [86] proposed a collision frequency model based on on the summation of the turbulent collision rate, buoyancy-driven collision rate and laminar shear collision rate. Only the turbulent collision rate is considered here:

$$\theta_{ij} = 0.089\pi(d_i + d_j)^2\epsilon^{1/3}(d_i^{2/3} + d_j^{2/3})^{1/2} \tag{5.13}$$

For the collision efficiency P_c, Prince and Blanch [86] suggested:

$$P_c(d_i, d_j) = exp\Bigg[- \frac{\left(\frac{d_{ij}^3\rho_c}{16\sigma}\right)^{1/2}\epsilon^{2/3}ln\frac{h_0}{h_f}}{d_{ij}^{2/3}}\Bigg] \tag{5.14}$$

where d_{ij} is the equivalent diameter defined as

$$d_{ij} = \left[\frac{1}{2}\left(\frac{1}{d_i} + \frac{1}{d_j}\right)\right]^{-1} \tag{5.15}$$

In this model, d_i and d_j are the diameter of bubbles of class i and j. h_0 and h_f are the initial and final (critical) film thickness between coalescing bubbles.

Another expression for the coalescence efficiency was given by Chesters et al. [6] as follows:

$$P_c(d_i, d_j) = exp\Bigg[- c\left(\frac{We}{2}\right)^{1/2}\Bigg], \quad We = \frac{\rho_c(\epsilon d_{ij})^{2/3}d_{ij}}{2\sigma} \tag{5.16}$$

A third alternative expression of collision efficiency was proposed by Luo et al. [54]

$$P_c(d_i, d_j) = exp\Bigg[- c\frac{[0.75(1 + \xi_{ij}^2)(1 + \xi_{ij}^3)]^{1/2}}{(\rho_d/\rho_c + 0.5)^{1/2}(1 + \xi_{ij})^3}We_{ij}^{1/2}\Bigg] \tag{5.17}$$

where $We_{ij} = \rho_c d_i \overline{u}_{ij}^2/\sigma$; $\xi_{ij} = d_i/d_j$; $\overline{u}_{ij} = (\overline{u}_i^2 + \overline{u}_j^2)^{1/2} = \overline{u}_i(1 + \xi_{ij}^{-2/3})$; $\overline{u}_i = \beta^{1/2}(\epsilon d_i)^{1/2}$. Here β is a constant set to 2.05.

5.2.2 Coalescence model by Luo and Svendson (1996)

As described in the latest section, the coalescence rates $\Omega_C(v_i, v_j) = \theta_{i,j} P_c$ and in this model the collision rate of bubble per unit volume is obtained by Saffman and Turner [97] as follows:

$$\theta_{i,j} = \frac{9\alpha_G^2 f_i f_j}{\pi d_i^3 d_j^3}(d_i + d_j)^2 \epsilon^{1/3}(d_i^{1/3} + d_j^{1/3})^{1/2} \tag{5.18}$$

where d_i and d_j are the diameter of bubbles of class i and j with their number density n_i and n_j respectively.

In the present study, the coalescence probability P_c is expressed as follows Hagesather et al. [75]:

$$P_c(d_i, d_j) = Exp\Big(- C\frac{[0.75(1 + \xi_{ij}^2)(1 + \xi_{ij}^3)]^{1/2}}{(\rho_G/\rho_L + 0.5)^{1/2}(1 + \xi_{ij})^3} We_{ij}^{1/2}\Big) \tag{5.19}$$

where $We_{ij} = \rho_L d_i u_{ij}^2/\sigma$; $\xi_{ij} = d_i/d_j$; $u_{ij} = (u_i^2 + u_j^2)^{1/2}$; $u_i = \beta^{1/2}(\epsilon d_i)$. The constant C is set to 0.5 in this model.

5.2.3 Coalescence model by Wu et al. (1998)

Coalescence depends essentially on turbulent fluctuations and to a lesser degree on variation in rise velocity of different size bubbles and velocity gradients. These mechanisms force nearby bubbles to approach each other and leads to collisions. In this model, the coalescence is considered to occur in the case of binary collisions between two bubbles of classes i and j and the expression of coalescence rate is given by Wu et al. [100]:

$$\Omega_C(v_i, v_j) = C_{co}\eta_{co} d^2 (\epsilon d)^{1/3} n^2 \frac{1}{1 - \alpha_d^{1/3}} \tag{5.20}$$

C_{co} is an adjustable model parameter set to 0.03. η_{co} is the collision efficiency set to unit in this model.

5.2.4 Coalescence model by Lehr (2001)

In this model, collisions arising from turbulent fluctuations and from the difference in rise velocities of bubbles of different size are considered. For the first case the characteristic velocity is assumed to be the turbulent eddy velocity of the length scale of the bubbles. Smaller eddies do not contain sufficient energy to significantly affect bubble motion, while eddies much larger than the bubble size transport groups of bubbles. For the second case the characteristic velocity corresponds to the difference in rise velocities $\mathbf{U}$ of the bubbles. The characteristic velocity is expressed as

$$u^{'} = max(\sqrt{2}(\sqrt{d_1 d_2}\epsilon)^{1/3}, |\mathbf{U}_1 - \mathbf{U}_2|) \tag{5.21}$$

The coalescence efficiency depends on the size of the bubbles and on the velocity of approach. Experiments (Doubliez [35; 38] with single bubbles show that small bubbles and small approach velocities lead to a higher coalescence efficiency. Thus for two colliding bubbles with given diameters the coalescence efficiency depends on the relative velocity of approach. This velocity depends on the angle under which the two bubbles collide. The relative probability is assumed to be equal for all steradians. Hence the coalescence probability is given by

$$P_c(d_i, d_j) = max(\frac{u_{crit}}{u^{'}}, 1) \tag{5.22}$$

As reported by Duineveld [38] the conditions for coalescence to occur can be expressed with the help of a critical Weber number We_{crit}

$$We < We_{crit} \quad with \quad We = \frac{\rho_l u_{rel} d_{eq}}{\sigma} \tag{5.23}$$

where d_{eq} represents the equivalent diameter

$$d_{eq} = 2\left[\frac{1}{d_i} + \frac{1}{d_j}\right]^{-1} \tag{5.24}$$

and u_{rel} is the relative velocity of approach perpendicular to the plane of contact. Thus for the critical velocity used in Eqn. (5.22)

$$u_{crit} = \sqrt{\frac{We_{crit}\sigma}{\rho_c d_{eq}}} \tag{5.25}$$

From the experimental results of Doubliez [35] and Duineveld [38] $We_{crit} = 0.06$ is obtained for pure liquids (as water in this study).

5.3 Closure

This chapter described the most popular bubble break-up and coalescence models. First, the governing equations of break-up and coalescence models were expressed and outlined. In this study the model of Luo and Svendsen [55], both for breakage and coalescence phenomena, is implemented in the CFD package OpenFOAM because this model can be used to determine the breakage frequency of bubbles of size a_j to the smaller ones in the form of Eqn. (5.1). In the other hand, also in this model, the individual size group volume fraction f_i and f_j are considered and included in the calculation of the collision rate term $\theta_{ij}(v_i, v_j)$. The model of Luo and Svendsen [55] gives a good results in comparison with experimental measurement (see Bannari et al. [102]).

Chapter 6

Computational Methodology

6.1 Definition

Any numerical modelling consists of a model and a solution procedure. A model is a mathematical set of equations representing a physical and/or chemical process to be predicted. The solution procedure gives us the details about how to obtain an approximate solution to the model equations using a discrete form of the mathematical formulation. The dynamic behaviour of many multiphase flows in industrial applications are adequately modelled using Navier-Stokes equations. Heat and mass transfer as well as chemical reactions and phase changes are not considered in this study.

6.2 Spatial discretization

Domain discretization, the mathematical technique used to transform the model written as a set of coupled non-linear partial differential equations into a set of discrete algebraic

equations, can be subdivided into spatial discretization and temporal discretization. Spatial discretization defines the solution domain as a collection of well defined sub-volumes that fill and bound a region of space. Each of these control volumes (CV) encapsulates a computational point **P** at its centroid. The typical CV, an example of which is displayed in Fig. (6.1), is bounded by a set of convex faces of arbitrary shape resulting in polyhedral cells and an arbitrary unstructured mesh. In Fig. (6.1) **d** is the vector connecting adjacent cell centres **P** and **N**, and **A** is the face normal area vector for the common face between the cells. While all main dependent variables **u**, **p**,...etc. are defined at the cell centroid **P** and some derived properties may be defined at the cell face, **f** Jasak [64].

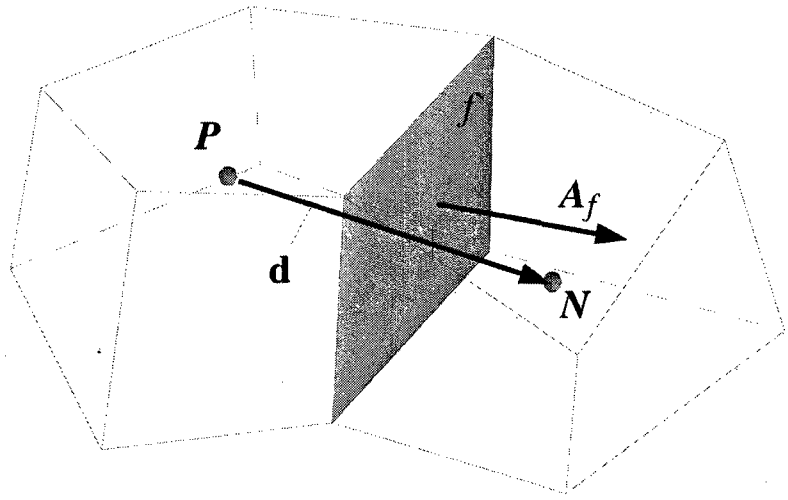

Figure 6.1: Control volume for finite volume discretization

The entire discretization procedure for each partial differential equation (PDE) on term by term is as follows:

$$\underbrace{\frac{d}{dt}\int_V \phi dV}_{} + \underbrace{\int_V \nabla \cdot (\overline{u}\phi) dV}_{} - \underbrace{\int_V \nabla \cdot (\Gamma_\phi \nabla \phi) dV}_{} = \underbrace{\int_V S_\phi(\phi) dV}_{} \tag{6.1}$$

Where the first term on the left hand side represents the temporal derivative, the second is the convection and the third term is the diffusion. The source term is written in the right hand side of the equation.

Here ϕ is the transported quantity, i.e. velocity, volume fraction or mass, and Γ is the diffusion coefficient. To represent this term with acceptable accuracy, the order of the discretization must be equal to or higher than the equation to be discretized. To conform to this rule, temporal discretization must also be second order. As a consequence of this requirement, all dependent variables are assumed to vary linearly around the point **P** and

time t, so that:

$$\phi(x) = \phi_P + (x - x_P)(\nabla\phi)_P \tag{6.2}$$

$$\phi(t + \Delta t) = \phi^t + \Delta t\left(\frac{\partial\phi}{\partial t}\right)_t \tag{6.3}$$

Each of the terms in Eqn. (6.1) will now be treated separately, starting with the spatial functions. Gauss theorem will be used throughout to reduce many of the volume integrals to their surface equivalents e.g.

$$\int_{\partial V} \nabla\phi dV = \oint_{\partial A} \phi dA \tag{6.4}$$

Several volume and surface integrals now need to be evaluated over the control volume to second order. Taking into account the variation of ϕ and x around P in Eqn. (6.2) it follows that Jasak [64]:

$$\int_{V_P} \phi(x) dV = \phi_P V_P \tag{6.5}$$

where V_P is the cell volume. Recalling that all the cell faces are convex and using similar assumptions as above, integration of the divergence operator over the cell surface produces:

$$\int_{V_P} \nabla\phi dV = \int_{\partial V_P} \phi dA = \sum_f \left(\int_f \phi dA\right) = \sum_f A_f \cdot \phi_f \tag{6.6}$$

Where ϕ_f is the cell face-average value of ϕ over the face and A_f is the cell face area vector.

6.2.1 Convection term

The discretization of the convection term can be obtained using Eqn. (6.6) to produce:

$$\int_{V_P} \nabla \cdot (\overline{u}\phi) dV = \sum_f A \cdot (\overline{u}\phi)_f = \sum_f (A \cdot \overline{u}_f)\phi = \sum_f F\phi_f \tag{6.7}$$

where F is the volume flux through the face defined as:

$$F = A \cdot \overline{u}_f \tag{6.8}$$

The flux, F depends on the face value of $\overline{u}_f$. This can be calculated in a similar fashion to ϕ_f described below, with the caveat that the velocity field from which the fluxes are derived must be such that finite volume **FV** continuity equation is obeyed, i.e.:

$$\int_V \nabla \cdot \overline{\mathbf{U}} dV = \int_{\partial V} dA \cdot \overline{\mathbf{U}} = \sum_f \left(\int_f dA \cdot \overline{\mathbf{U}} \right) = \sum F = 0 \tag{6.9}$$

Since linear variation of the dependent variable is assumed, the face centred value can be found from a simple interpolation between the cell values at **P** and **N** (where **N** indicates the neighbouring cell, see Fig. 6.2):

$$\phi_f = f_x \phi_P + (1 - f_x)\phi_N \tag{6.10}$$

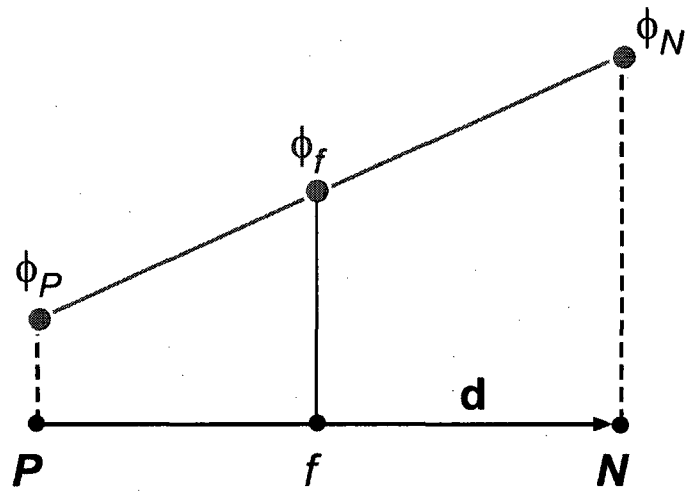

Figure 6.2: Face interpolation

Here the interpolation factor, f_x, is defined as the ratio of the distances FN and PN i.e:

$$f_x = \frac{fN}{PN} \tag{6.11}$$

The practise is commonly known as **C**entral **D**ifferencing (**CD**) and has been shown to be second order accurate even on unstructured meshes Emery [41]. The **CD** scheme has some drawbacks however, chief among which is its tendency to produce unphysical oscillations in the solution when the convection term strongly dominates the rest of the system. This is typically a product of unboundedness and can create particular problems in a coupled system like the Navier-Stokes equation. Boundedness in this context refers to the solution at a particular computational point being bounded by the solution values at surrounding points which influence it. For increasing convection dominance the solution will become increasingly non-physical and may diverge. This problem can be alleviated without impacting the formal order of the scheme by applying a higher order filter in the form of a fourth order dissipation term Hinze [71]. As has been mentioned previously however, higher than second order schemes are cumbersome to implement on a unstructured mesh. In addition, the fourth

order derivative may become very large due to discontinuous phenomena and itself become a source of instability Jasak [64].

An alternative discretization that improves stability and boundedness, is **U**pwind **D**ifferencing (**UD**). In the scheme's first order variant the face value of ϕ is determined according to the direction of the flux:

$$\begin{cases} \phi_f = \phi_P & : \ F \geq 0 \\ \phi_f = \phi_N & : \ F < 0 \end{cases} \tag{6.12}$$

Unfortunately, even second order variations of **UD** like linear upwind Warming and Beam [109] tend to introduce numerical diffusion into the system. This is particularly problematic with **LES** (**L**arge **E**ddy **S**imulation) since the contribution of the modeled turbulent diffusivity is typically very small, so that even modest false diffusion can produce large inaccuracies.

6.2.2 Diffusion term

Using a similar approach as above, the diffusion term in Eqn. (6.6) can be discretized as follows:

$$\int_{V_P} \nabla \cdot (\gamma_\phi \phi) dV = \sum_f \mathbf{A} \cdot (\gamma_\phi \phi)_f = \sum_f (\gamma_\phi)_f \mathbf{A} \cdot (\nabla \phi)_f \tag{6.13}$$

where $(\gamma_\phi)_f$ can be found from Eqn. (6.10). If the mesh is orthogonal, i.e. the vectors $\mathbf{d}$ and $\mathbf{A}$ in Fig. (6.1) are parallel, the face gradient of ϕ term can be expressed as follows:

$$\mathbf{A} \cdot (\nabla \phi)_f = |\mathbf{A}| \frac{\phi_N - \phi_P}{|\mathbf{d}|} \tag{6.14}$$

This employs a compact computational molecule and is more accurate than simply interpolating the cell centred gradients,

$$\left(\widetilde{\nabla \phi} \right)_f = \left(f_x (\phi)_P + (1 - f_x)(\nabla \phi)_N \right) \tag{6.15}$$

where

$$(\phi)_P = \frac{1}{V}\sum_f \phi_f \tag{6.16}$$

and the tilde signifies the interpolated gradient quantity. Although both methods are second order accurate, Eqn. (6.15) uses a larger computational molecule and has a larger truncation error than the first method Issa [110].

If the mesh is not orthogonal, as is often the case, Eqn. (6.14) is no longer second order accurate and needs to be supplemented as follows:

$$\mathbf{A}\cdot(\nabla\phi)_f = |\mathbf{A}_d|\frac{\phi_N - \phi_P}{|d|} + \mathbf{A}_\Delta \cdot (\widetilde{\nabla\phi})_f \tag{6.17}$$

where the vector $\mathbf{A}_d$ represents the component parallel to $\mathbf{d}$ and $\mathbf{A}_\Delta$ is the remainder that must satisfy the equality (see Fig. (6.3))

$$\mathbf{A} = \mathbf{A}_d + \mathbf{A}_\Delta \tag{6.18}$$

In the Eqn. (6.17) the first term on the right hand side represents the orthogonal term and the second is the non-orthogonal term.

There is some scope for variability of the component vectors A_d and A_δ within the constraints of Eqn. (6.18). Several such configurations are explored by Jasak [64] with the conclusion that the approach known as 'over-relaxed' is the most robust, convergent and computationally efficient. In the 'over-relaxed' approach the orthogonal vector component is calculated from,

$$\mathbf{A}_d = \frac{d}{d\cdot\mathbf{A}}|\mathbf{A}|^2 \tag{6.19}$$

This approach increases the importance of the term in ϕ_p and ϕ_N with increased non-orthogonality, as shown by the face area decomposition in Fig. (6.3).

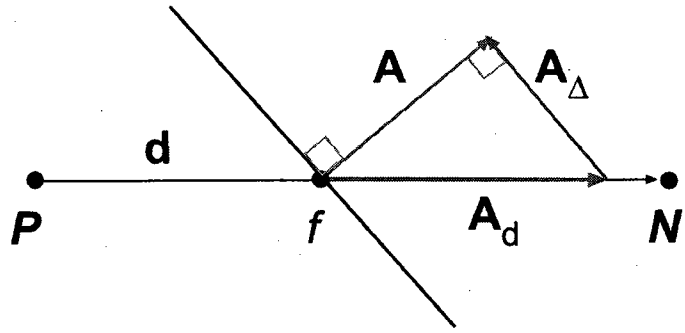

Figure 6.3: Decomposition of the face area vector due to non-orthogonality using the 'over-relaxed' approach.

6.2.3 Source terms

All terms of a transport equation that cannot be written as convection, diffusion or temporal contributions are here loosely classified as source terms. Source terms typically consist of a general function of ϕ and other variables, that need to be linearized to be incorporated in the solution matrix:

$$S_\phi(\phi) = S_c + S_P\phi \tag{6.20}$$

where S_c and S_P can also depend on ϕ. Following the mid-point rule from Eqn. (6.5) the volume integral is calculated from,

$$\int_{V_P} S_\phi(\phi)dV = S_c V_P + S_P V_P \phi_P \tag{6.21}$$

6.3 Time discretization

Next we consider the temporal derivative and integration of the generalized transport equation (6.1) in time. The integral relation for the generic transport equation can be written

as,

$$\int_t^{t+\Delta t}\left[\frac{\partial}{\partial t}\int_V \phi dV + \int_V \nabla\cdot(\overline{\mathbf{U}}\phi)dV - \int_V \nabla\cdot(\Gamma\phi\nabla\phi)dv\right]dt = \int_t^{t+\Delta t}\left[\int_V S_\phi(\phi)dV\right]dt \quad (6.22)$$

Using equations (6.6), (6.13), (6.21) and (6.22) can be rewritten as:

$$\int_t^{t+\Delta t}\left[\left(\frac{\partial\phi}{\partial t}\right)V_P + \sum_f F\phi_f - \sum_f(\Gamma_\phi)_f S\cdot(\nabla\phi)_f\right]dt = \int_t^{t+\Delta}[S_c V_P + S_P V_P\phi_P]dt \quad (6.23)$$

6.3.1 Time Centered Crank-Nicholson

Keeping in mind the assumed variation of ϕ with t Eqn. (6.3), the temporal derivative and time integral can be calculated directly as follows:

$$\left(\frac{\partial\phi}{\partial t}\right)_P = \frac{\phi_P^n - \phi_P^{n-1}}{\Delta t} \quad (6.24)$$

and

$$\int_t^{t+\Delta t}\phi(t)dt = \frac{1}{2}(\phi^{n-1} + \phi^n)\Delta t \quad (6.25)$$

where $\phi^n = \phi(t+\Delta t)$ and $\phi^{n-1} = \phi(t)$ represent the value of the dependent variable at the new and previous times respectively. Eqn. (6.24) provides the temporal derivative at a centered time between times $n-1$ and n. Combining equations (6.23), (6.24) and (6.25) produces:

$$\begin{aligned}\frac{\phi_P^n - \phi_P^{n-1}}{\Delta t}V_P + \frac{1}{2}\left[\sum_f F\phi_f - \sum_f(\Gamma_\phi)_f\mathbf{A}\cdot(\nabla\phi)_f\right]^n \\ + \frac{1}{2}\left[\sum_f F\phi_f - \sum_f(\Gamma_\phi)_f\mathbf{A}\cdot(\nabla\phi)_f\right]^{n-1} \\ = \frac{1}{2}\Big([S_c V_P + S_P V_P\phi_P]^n - [S_c V_P + S_P V_P\phi_P]^{n-1}\Big)\end{aligned} \quad (6.26)$$

This form of temporal discretization is called the Crank-Nicholson method. It is second order accurate in time and requires the face and cell-centred values of ϕ and $\nabla\phi$ along

with the convective and diffusive fluxes for both the current and new time levels. The Crank-Nicholson scheme requires inner-iterations during each time step and coupled with the memory overhead due to the large number of stored variables, this means the scheme is expensive compared to the Backward Differencing scheme described below. In previous work of Jasak [64], the new value of ϕ_P was determined and the Eqn. (6.26) produces an algebraic equation:

$$a_P \phi_P^n + \sum_S a_N \phi_N^n = R_P \tag{6.27}$$

For every control volume, one equation of this form is assembled. The value of ϕ_P^n depends on the values in the neighbouring cells, thus creating a system of algebraic equations:

$$[\mathbf{A}][\phi] = [\mathbf{R}] \tag{6.28}$$

where $[\mathbf{A}]$ is a sparse matrix, with coefficients a_P on the diagonal and a_N off the diagonal, $[\phi]$ is the vector of $\phi - s$ for all control volumes and $[\mathbf{R}]$ is the source term vector.

When this system is solved, it gives a new set of ϕ values which is the solution for the new time-step. The coefficient a_P in Eqn. (6.27) includes the contribution from all terms corresponding to ϕ_P^n: The temporal derivative, convection and diffusion terms as well as the linear part of the source term.The coefficient a_N include the corresponding terms for each of the neighbouring points.

It has been customary to neglect the variation of the face values of ϕ and $\Delta\phi$ in time (Patankar [128]). This leads to several methods of temporal discretization. The new form of the discretized transport equation combines the old and new time-level convection, diffusion and source terms, leaving the temporal derivative unchanged Jasak [64]:

$$\frac{\phi_P^n - \phi_P^0}{\Delta t} V_P + \sum_f \mathbf{F}\phi_f - \sum_f (\Gamma_\phi)_f S \cdot (\nabla\phi)_f = SuV_P + S_P V_P \phi_P \tag{6.29}$$

6.3.2 Solution Techniques for Systems of Linear Algebraic Equations

We consider the system of algebraic equations created by the discretization of Eqn. (6.27):

$$a_P\phi_P^n + \sum_S a_N\phi_N^n = \mathbf{R}_P \tag{6.30}$$

This system can be solved in several different ways. Existing solution algorithms fall into two main categories: direct and iterative methods. Direct methods give the solution of the system of algebraic equations in a finite number of arithmetic operations. Iterative methods start with an initial guess and then continue to improve the current approximation of the solution until some 'solution tolerance' is met. While direct methods are appropriate for small systems, the number of operations necessary to reach the solution raises with the number of equations squared, making them prohibitively expensive for large systems Muzaferija [121]. Iterative methods are more economical, but they usually pose some requirements on the matrix. An iterative solver require diagonal dominance in order to guarantee convergence. A matrix is said to be diagonally equal if the magnitude of the diagonal (central) coefficient is equal to the sum of magnitudes of off-diagonal coefficients. The additional condition for diagonal dominance is that $|a_P| > \sum_n |a_N|$ for at least one row of the matrix.

In order to enable the use of iterative solvers, the diagonal dominance needs to be enhanced in some other way [64], namely through **under-relaxation.** Consider the original system of Eqn. (6.27), the Diagonal dominance is created through an artificial term added to both left and right-hand side of Eqn. (6.27):

$$a_P\phi_P^n + \frac{1-\delta}{\delta}a_P\phi_P^n + \sum_N a_N\phi_N^n = \mathbf{R}_P + \frac{1-\delta}{\delta}a_P\phi_P^0 \tag{6.31}$$

Or

$$\frac{a_P}{\delta}\phi_P^n + \sum_N a_N\phi_N^n = \mathbf{R}_P + \frac{1-\delta}{\delta}a_P\phi_P^0 \tag{6.32}$$

Here, ϕ_P^0 represents the value of ϕ from the previous iteration and δ is the under-relaxation factor ($0 < \delta \leq 1$). Additional terms cancel out when steady-state is reached ($\phi_P^n = \phi_P^0$).

In this study, the iterative solution procedure used to solve the system of algebraic equations is the **C**onjugate **G**radient (**CG**) method, originally proposed by Hestens and Steifel [91]. It guarantees that the exact solution will be obtained in a number of iterations smaller or equal to the number of equations in the system. The convergence rate of the solver depends on the dispersion of the eigenvalues of the matrix [**A**] in Eqn. (6.28) and and can be improved through pre-conditioning. For symmetric matrices, the **I**ncomplete **C**holesky preconditioned **C**onjugate **G**radient (**ICCG**) solver will be used. The method is described in detail by Jacobs [24]. The adopted solver for asymmetric matrices is the **Bi-CGSTAB** by van der Vorst [60].

6.3.3 Second Order Backward Differencing

Since the variation of ϕ in time is assumed to be linear, Eqn. (6.24) provides a second order accurate representation of the time derivative at $t + \frac{1}{2}\Delta t$ only. Assuming the same value for the derivative at time t or $t + \Delta t$ reduces the accuracy to first order. However, as was mentionned before, if the temporal derivative is discretized to second order, the whole discretization of the transport equation will be second order without the need to centre the spatial terms in time. The scheme so produced is called **B**ackward **D**ifferencing (**BD**) and uses three time levels.

$$\phi^{n-2} = \phi^{t-\Delta t} \tag{6.33}$$

$$\phi^{n-1} = \phi^{t} \tag{6.34}$$

$$\phi^{n} = \phi^{t+\Delta t} \tag{6.35}$$

To calculate the temporal derivative. Now time level $n-2$ expressed as a Taylor expansion around n is written as:

$$\phi^{n-2} = \phi^{n} - 2\left(\frac{\partial \phi}{\partial t}\right)^{n} \Delta t + 2\left(\frac{\partial^2 \phi}{\partial t^2}\right)^{n} \Delta t^2 + O(\Delta t^3) \tag{6.36}$$

Recall also that the Taylor expansion for time $n-1$ around n with a third order truncation error is given by:

$$\phi^{n-1} = \phi^n - \left(\frac{\partial \phi}{\partial t}\right)^n \Delta t + \frac{1}{2}\left(\frac{\partial^2 \phi}{\partial t^2}\right)^n \Delta t^2 + O(\Delta t^3) \tag{6.37}$$

Combining equation (6.36) and (6.37) produces a second order approximation of the temporal derivative at the new time, n:

$$\left(\frac{\partial \phi}{\partial t}\right)^n = \frac{\frac{3}{2}\phi^n - 2\phi^{n-1} + \frac{1}{2}\phi^{n-2}}{\Delta t} \tag{6.38}$$

By neglecting the temporal variation in the face fluxes and derivatives, Eqn. (6.38) produces a fully implicit second order accurate discretiszation of the general transport equation,

$$\frac{\frac{3}{2}\phi^n - 2\phi^{n-1} + \frac{1}{2}\phi^{n-2}}{\Delta t} VP + \sum_f F\phi_f^n - \sum_f (\Gamma_\phi)_f S \cdot (\nabla \phi)_f^n = S_c VP + S_P V_P \phi_P^n \tag{6.39}$$

Analysis has shown [66] that the Backward Differencing method, although cheaper and considerably easier to implement than the Crank-Nicholson method. Given its ease of implementation and comparatively low cost, the Backward Differencing scheme is thus the preferred method.

6.4 PISO procedure

In this study the **PISO** (**P**ressure **I**mplicit with **S**plitting of **O**perators) procedure proposed by Issa [110] is used to couple the pressure to the velocity via flux conservation. The pressure equation is derived as a semi-discretized form of the momentum equation (6.23) using the discretization techniques described in previous sections.

$$a_P \overline{\mathbf{U}}_P = \mathbf{H} - \nabla \overline{p} \tag{6.40}$$

Here the pressure gradient term remains undiscretized and both sides have been divided through with the cell volume to allow face interpolation of the coefficients. a_P consists of the sum of the coefficients of $\overline{\mathbf{U}}_P$,

Dividing both sides of Eqn. (6.40) by a_P produces an expression for $\overline{\mathbf{U}}$:

$$\overline{\mathbf{U}} = \frac{\mathbf{H}}{a_P} - \frac{\nabla \overline{p}}{a_P} \tag{6.41}$$

Interpolating Eqn. (6.41) to express the face velocity gives,

$$\overline{\mathbf{U}}_f = \left(\frac{\mathbf{H}}{a_P}\right)_f - \left(\frac{\nabla \overline{p}}{a_P}\right)_f \tag{6.42}$$

The face flux $\mathbf{F}$ is calculated using Eqn. (6.42) as follow:

$$\mathbf{F} = S.\mathbf{U}_f \tag{6.43}$$

Using the techniques introduced in Eqn. (6.6) the discretized form of the continuity equation $\nabla \cdot \overline{\mathbf{U}} = 0$ can be written as:

$$\nabla \cdot \overline{\mathbf{U}} = \sum_f \mathbf{S} \cdot \overline{\mathbf{U}}_f = 0 \tag{6.44}$$

Substituting $\overline{\mathbf{U}}_f$ from Eqn. (6.42) into the above relation produces the pressure equation:

$$\nabla \cdot \left(\frac{1}{a_P} \nabla \overline{p}\right) = \nabla \cdot \left(\frac{\mathbf{H}}{a_P}\right) = \sum_f \mathbf{S} \cdot \left(\frac{\mathbf{H}}{a_P}\right)_f \tag{6.45}$$

The Laplacian on the l.h.s. of Eqn. (6.45) and the pressure gradient on the r.h.s. of Eqn. (6.40) can be discretized in a manner similar to the diffusion term in section 6.2 resulting in the final form of the Navier-Stokes system:

$$a_P \overline{\mathbf{U}}_P = \mathbf{H} - \sum_f \mathbf{S} \cdot \overline{p}_f \tag{6.46}$$

$$\sum_f \mathbf{S} \cdot \left(\frac{1}{a_P}\right)_f (\nabla \overline{p})_f = \sum_f \mathbf{S} \cdot \left(\frac{\mathbf{H}}{a_P}\right)_f \tag{6.47}$$

The procedure used to solve the unknown variables $\overline{p}$ and $\overline{\mathbf{U}}$ is depicted as a flowchart in Fig. 6.4.

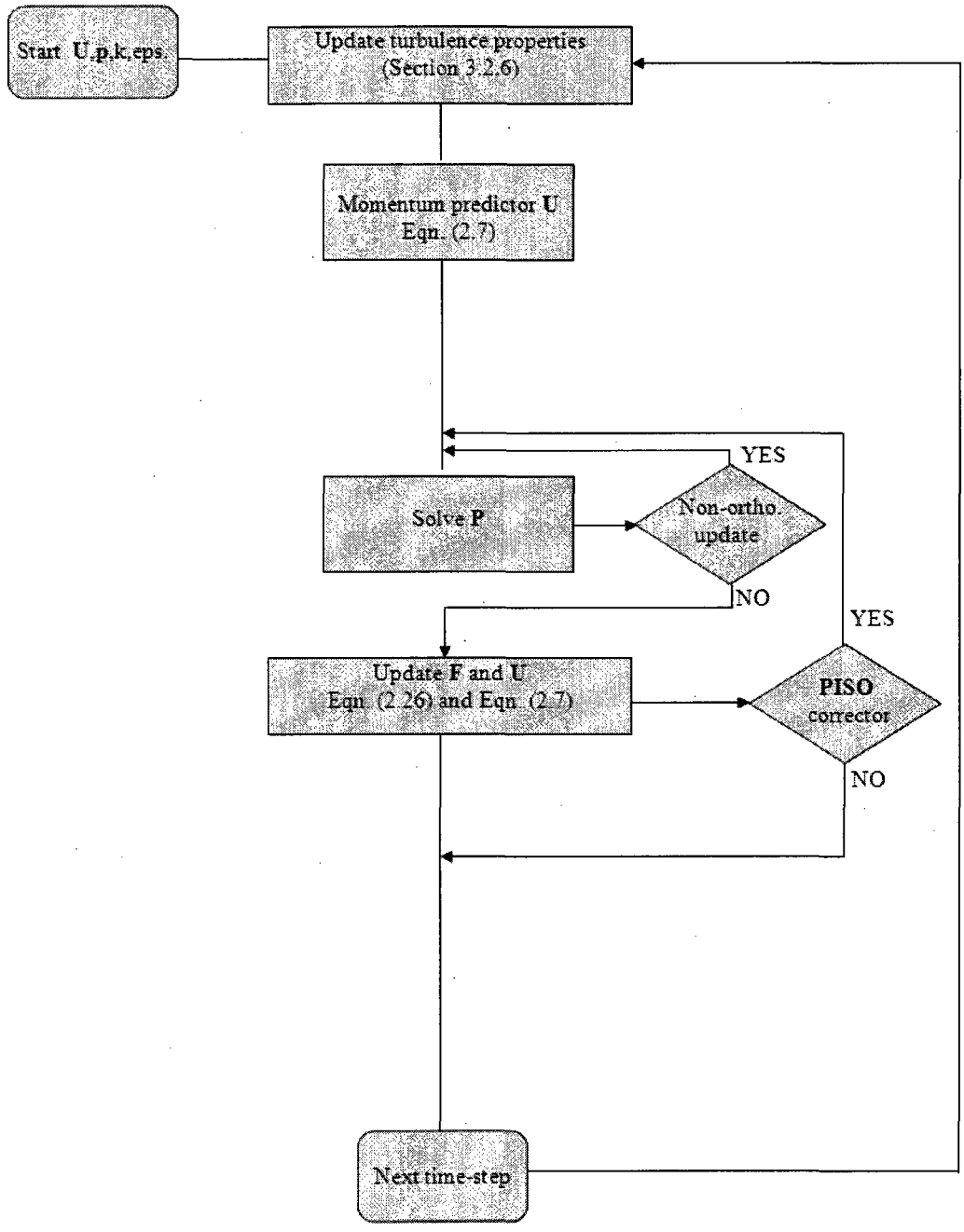

Figure 6.4: **PISO** solution procedure

The individual steps of the solution procedure are described below:

1. The procedure starts with the initial conditions for the unknown flow variables ($\overline{\mathbf{U}}$, $\overline{p}$, k, ϵ, F,...etc.).

2. The momentum predictor step solves a tentative velocity using the old-time values of $\overline{p}$ and face flux F with Eqn. (6.46). Solution of the matrix is achieved by employing an iterative **C**onjugate **G**radient method (**CG**). Convergence time is accelerated by preconditioning this matrix using the procedures of **Bi-CGSTAB** detailed by Van der Vorst [60] which is applicable to asymmetric matrices.

3. The tentative velocity serves to update the off-diagonal matrix components, $\mathbf{H}$ (Eqn. (??))

4. This is in turn used in the solution of the pressure equation (6.47). The system matrix for the pressure equation is solved using the **I**ncomplete **C**holeski preconditioned **C**onjugate **G**radient (**ICCG**) method Jacobs [24].

5. Due to the explicit nature of the non-orthogonal component of the face interpolation of $\overline{p}$, the pressure equation has to be solved iteratively. Typically, a single or at most two corrector steps are sufficient to converge the non-orthogonal component.

6. The solution of the pressure is followed by the projection of the velocities and fluxes into a divergence free form Eqn. (6.46) and Eqn. (6.42) respectively.

7. Steps 4-7 are now repeated iteratively until the dependent variables stop changing.

8. Finally, the calculation moves to the next time step, where the current values are used as initial guesses for the next cycle of the solution.

6.5 SIMPLE Algorithm

If a steady-state problem is being solved iteratively, it is not necessary to fully resolve the linear pressure-velocity coupling, as the changes between consecutive solutions are no longer small. Non-linearity of the system becomes more important, since the effective time-step is much larger Jasak [64].

The SIMPLE algorithm by Patankar [128] is formulated to take advantage of these facts:

• An approximation of the velocity field is obtained by solving the momentum equation. The pressure gradient term is calculated using the pressure distribution from the previous iteration or an initial guess. The equation is under-relaxed in an implicit manner (see Eqn. (6.32)), with **the velocity under-relaxation factor** α_U.

• The pressure equation is formulated and solved in order to obtain the new pressure distribution.

• A new set of conservative fluxes is calculated using Eqn. (6.43). As it has been noticed before, the new pressure field includes both the pressure error and convection-diffusion error. In order to obtain a better approximation of the <correct> pressure field, it would be necessary to solve the pressure equation again. On the other hand, the non-linear effects are more important than in the case of transient calculations. It is enough to obtain an approximation of the pressure field and recalculate the $H(U)$ coefficients with the new set of conservative fluxes. The pressure solution is therefore under-relaxed in order to take into account the velocity part of the error:

$$P^{new} = P^{old} + \delta_P(P^p - P^{old}) \tag{6.48}$$

Where

- p^{new} is the approximation of the pressure field that will be used in the next momentum predictor.

- p^{old} is the pressure field used in the momentum predictor.

- p^P is the solution of the pressure equation.

- δ_P is the pressure **under-relaxation** factor, $(0 < \delta_p \leq 1)$.

Perić [81] gives an analysis of the under-relaxation procedure based on the expected behaviour of the second corrector in the PISO sequence. The recommended values of under-relaxation factors are (Perić [81]):

- $\delta_p = 0.2$ for the pressure
- $\delta_p = 0.8$ for momentum

6.6 Closure

The discretisation of the temporal and spatial terms based on the face addressing procedure has been described in this chapter. Several methods of temporal discretisations have also been examined. Also a discretisation procedure for coupled systems of equations has been presented. The adopted treatment of the pressure-velocity system is based on the PISO algorithm for transient calculations and the SIMPLE approach for steady-state flows. calculations has been summarised.

Chapter 7

Results and discussions

7.1 Part I: Turbulence modelling

In this first part we present and analyze the results obtained with the mathematical model of turbulence on bubbly flow.

7.1.1 Grid mesh dependence investigation

In order to study the influence of mesh resolution on the predicted results, three different grid have been generated, arbitrarily they are named: coarse, medium and fine Fig. (7.1). Pfleger and Becker [17], Buwa and Ranade [134] discussed the effects of the grid dependence on the flow properties (gas hold-up and liquid velocity profiles) and they reported that the agreement of the predictions with the measurements data deteriorates with grid refinement. It should be noted that the numerical diffusion in coarse grid simulation suppresses the effect of many of the physical model (for example, the lift and virtual mass, the turbulence dispersion of gas bubbles). However grid refinement reduces significantly the numerical

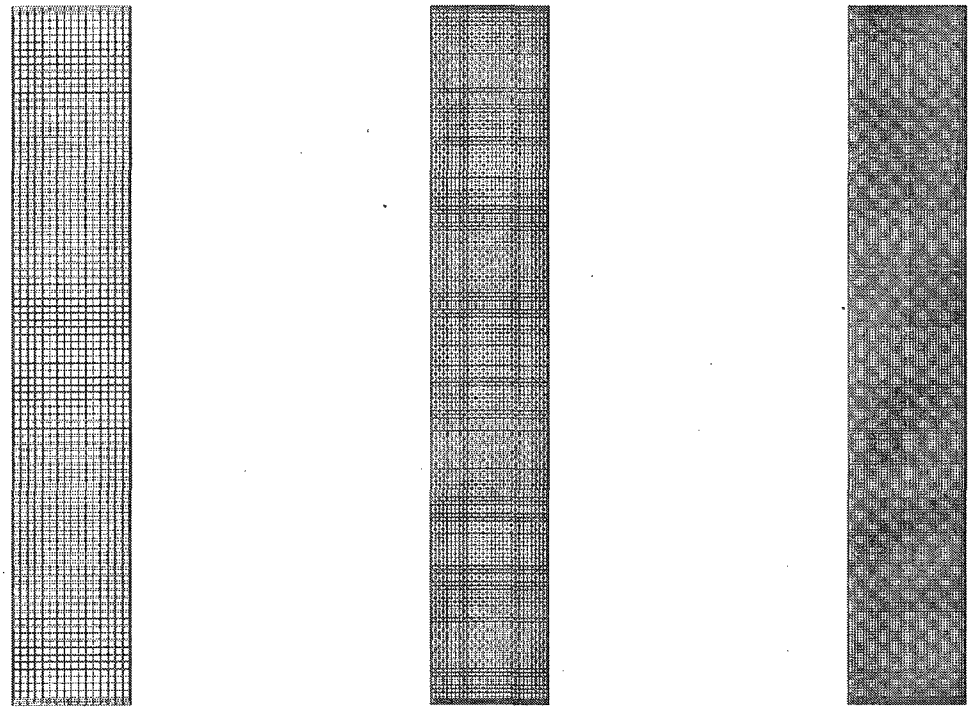

Figure 7.1: Grid meshes used. From the left to right coarse (16×96×4), medium (29×171×7), fine ($40 \times 240 \times 10$)

diffusion, although it is not eliminated, and the effects of physical models mentioned above become evident.

In the present study, two different inlet gas velocity (0.14 cm/s and 0.73 cm/s) are used. For a qualitative comparison, the comparison is limited for one inlet gas velocity chosen for two different liquid levels ($H/W = 2.25$ and $H/W = 4.5$) and it can be seen that the results are good in the case of the medium grid for all these cases. When $H/W = 2.25$, the gas volume fraction profile Fig. 7.2 is again good in the case of the medium grid, better than the coarse and fine grids. The same conclusion for the gas and liquid velocity profiles (Fig. 7.3 and Fig. 7.4). For the turbulence properties (kinetic energy, dissipation rate, turbulent viscosity and turbulent intensity) the predicted results are shown in Figures (7.5, 7.6, 7.7 and 7.8) respectively. In the case of $H/W = 4.5$ for the same superficial gas velocity (0.14 cm/s) the results obtained by the model are shown in Figures (7.9, 7.10, 7.11, 7.12, 7.13, 7.14 and 7.15). They show that the turbulence properties increase with the refinement of grid mesh causing divergence.

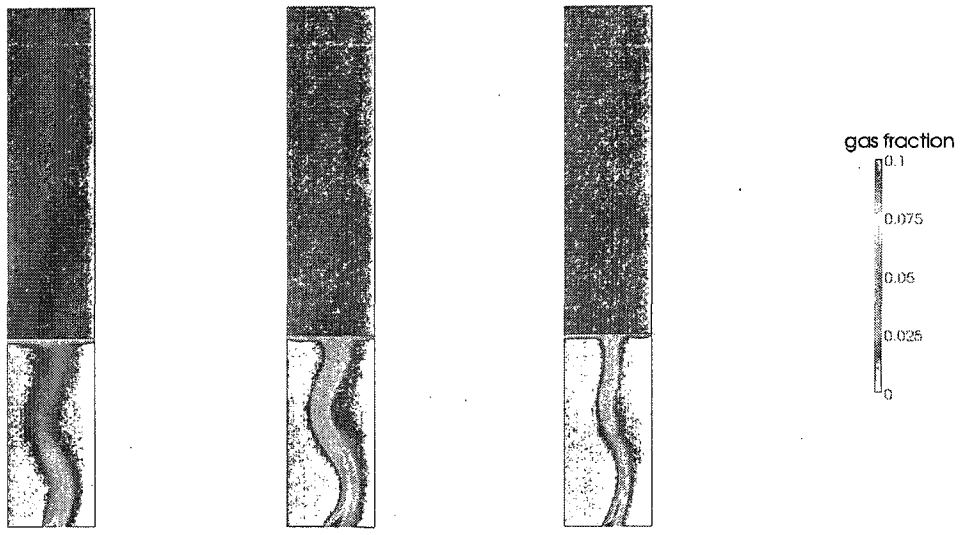

Figure 7.2: Gas hold-up [−] mesh refinement tests in the case of $U_{d,s} = 0.14\ cm/s$ and $H/W = 2.25$. Coarse (left), medium (center), fine (right).

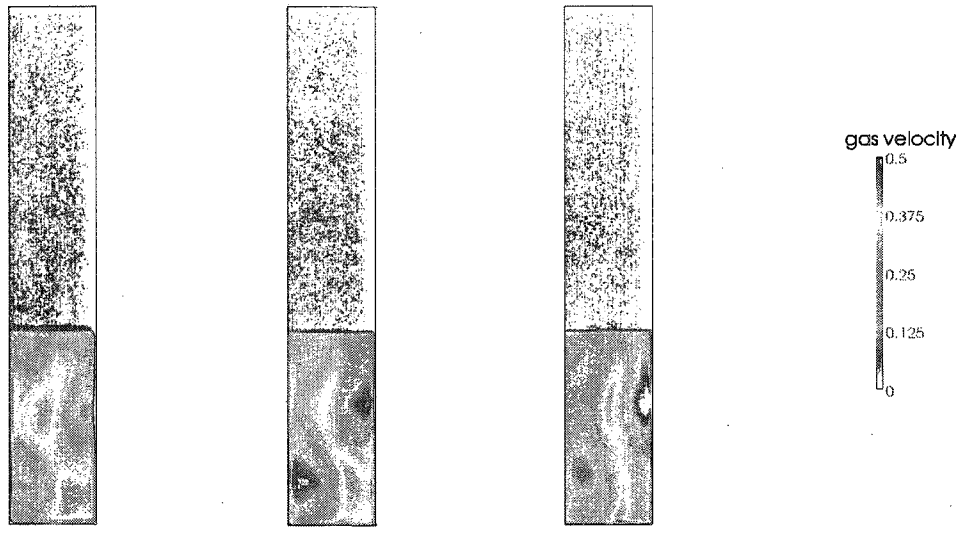

Figure 7.3: Gas velocity $[m/s]$ mesh refinement tests in the case of $U_{d,s} = 0.14\ cm/s$ and $H/W = 2.25$. Coarse (left), medium (center), fine (right).

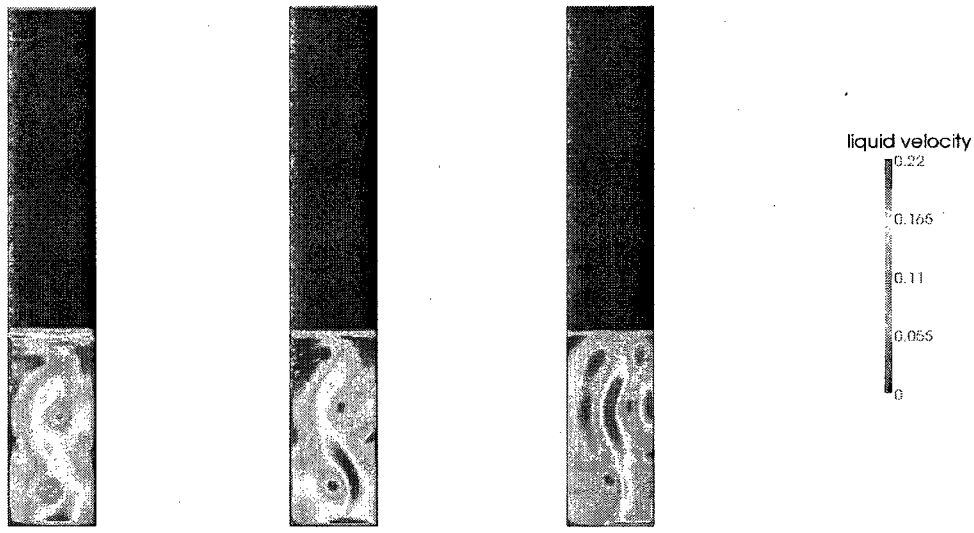

Figure 7.4: Liquid velocity $[m/s]$ mesh refinement tests in the case of $U_{d,s} = 0.14\ cm/s$ and $H/W = 2.25$. Coarse (left), medium (center), fine (right).

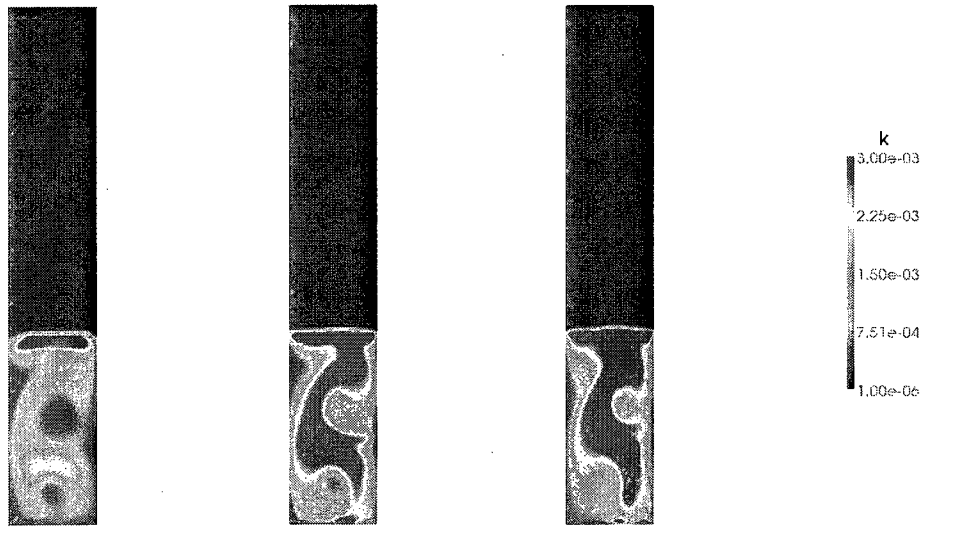

Figure 7.5: Kinetic energy $[m^2/s^2]$ mesh refinement tests in the case of $U_{d,s} = 0.14\ cm/s$ and $H/W = 2.25$. Coarse (left), medium (center), fine (right).

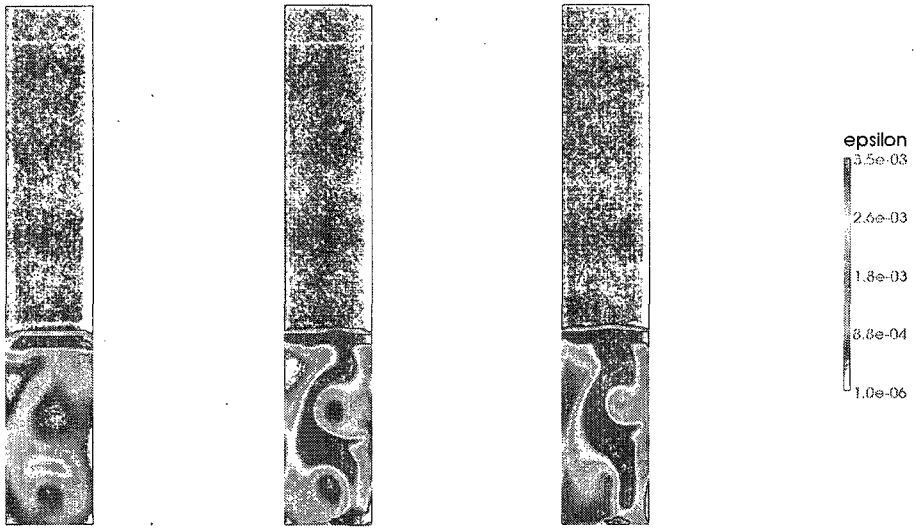

Figure 7.6: Dissipation rate $[m^2/s^3]$ mesh refinement tests in the case of $U_{d,s} = 0.14\ cm/s$ and $H/W = 2.25$. Coarse (left), medium (center), fine (right).

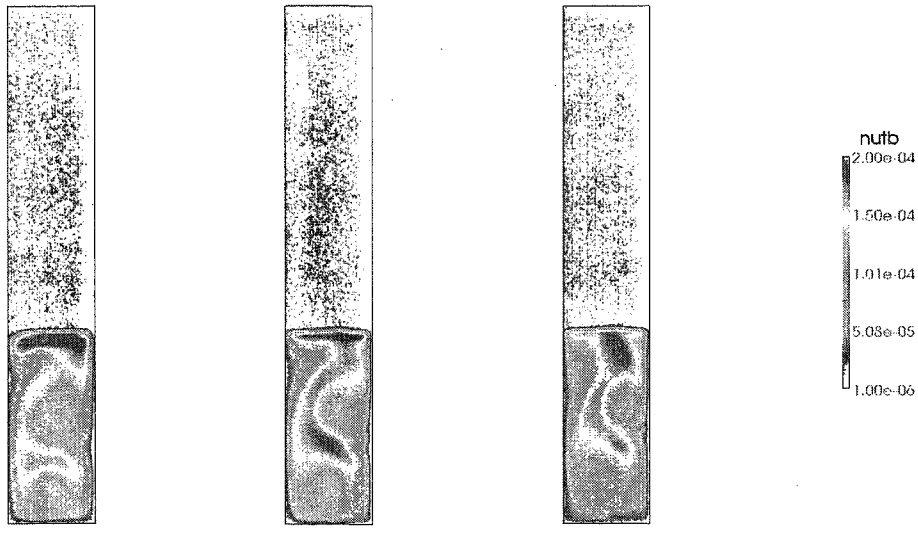

Figure 7.7: Turbulent viscosity $[m^2/s]$ mesh refinement tests in the case of $U_{d,s} = 0.14\ cm/s$ and $H/W = 2.25$. Coarse (left), medium (center), fine (right).

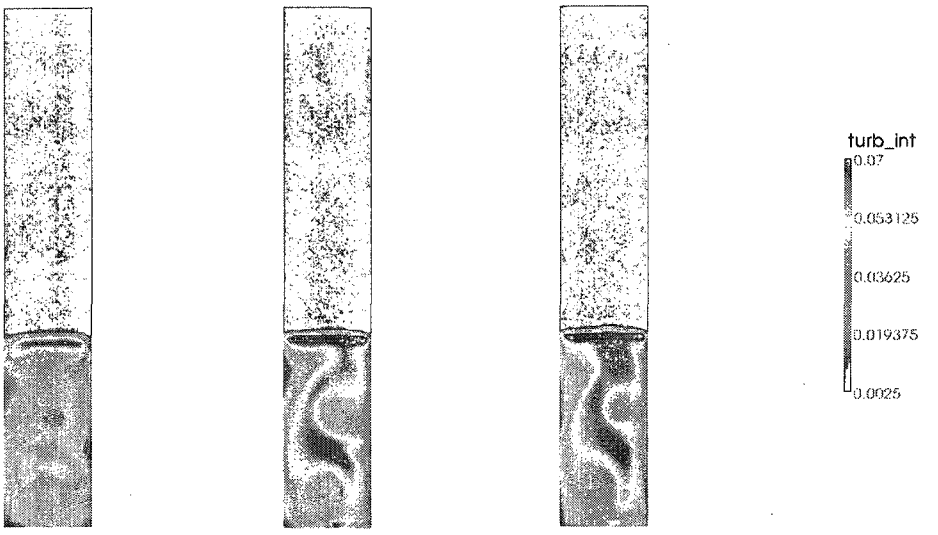

Figure 7.8: Turbulent intensity $[m/s]$ mesh refinement tests in the case of $U_{d,s} = 0.14\ cm/s$ and $H/W = 2.25$. Coarse (left), medium (center), fine (right).

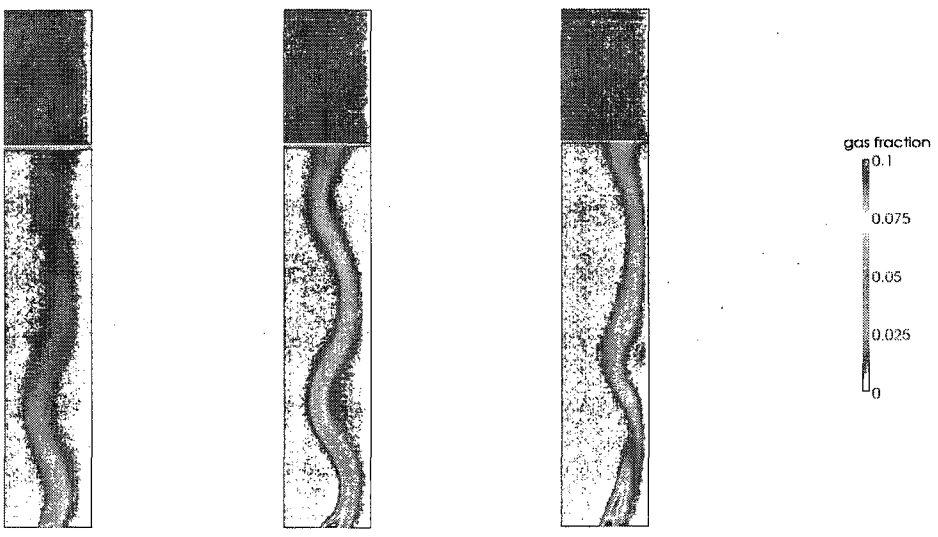

Figure 7.9: Gas volume fraction $[-]$ mesh refinement tests in the case of $U_{d,s} = 0.14\ cm/s$ and $H/W = 4.5$. Coarse (left), medium (center), fine (right).

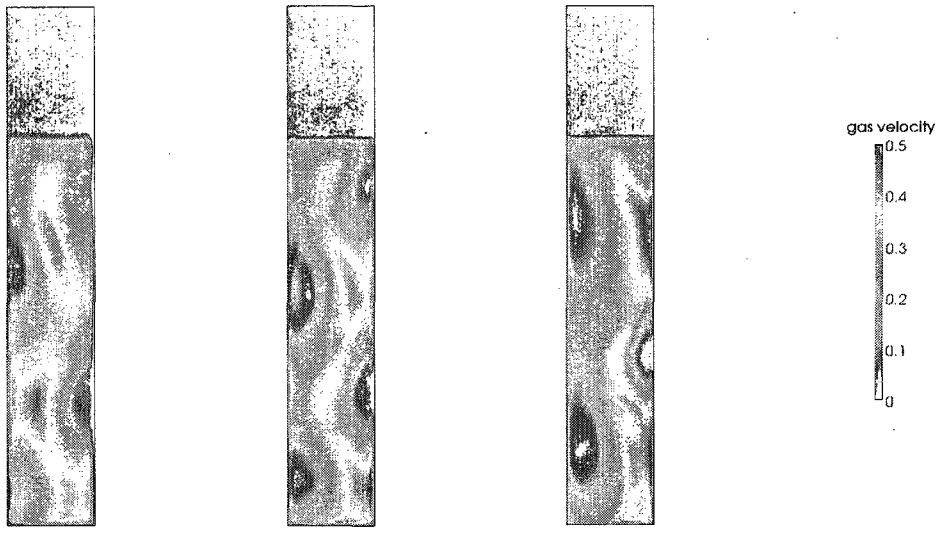

Figure 7.10: Gas velocity $[m/s]$ mesh refinement tests in the case of $U_{d,s} = 0.14\ cm/s$ and $H/W = 4.5$. Coarse (left), medium (center), fine (right).

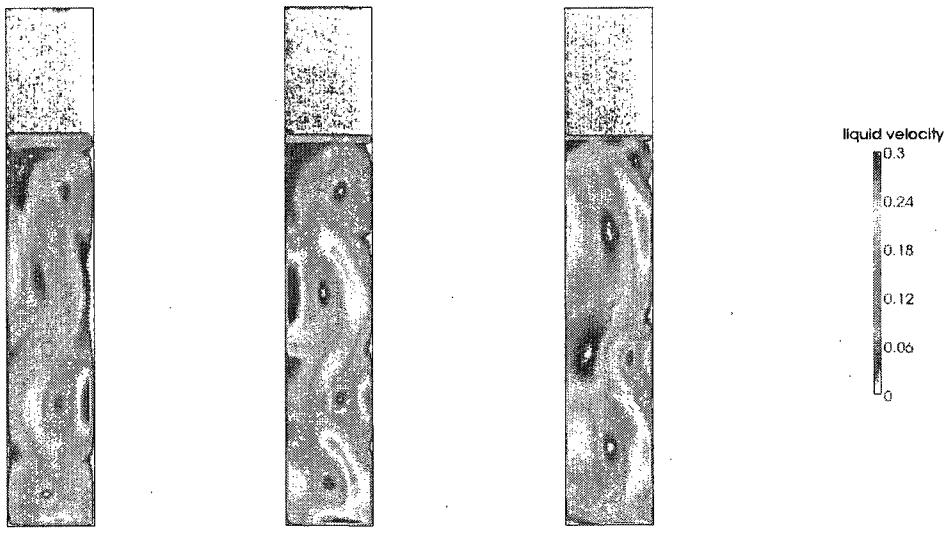

Figure 7.11: Liquid velocity $[m/s]$ mesh refinement tests in the case of $U_{d,s} = 0.14\ cm/s$ and $H/W = 4.5$. Coarse (left), medium (center), fine (right).

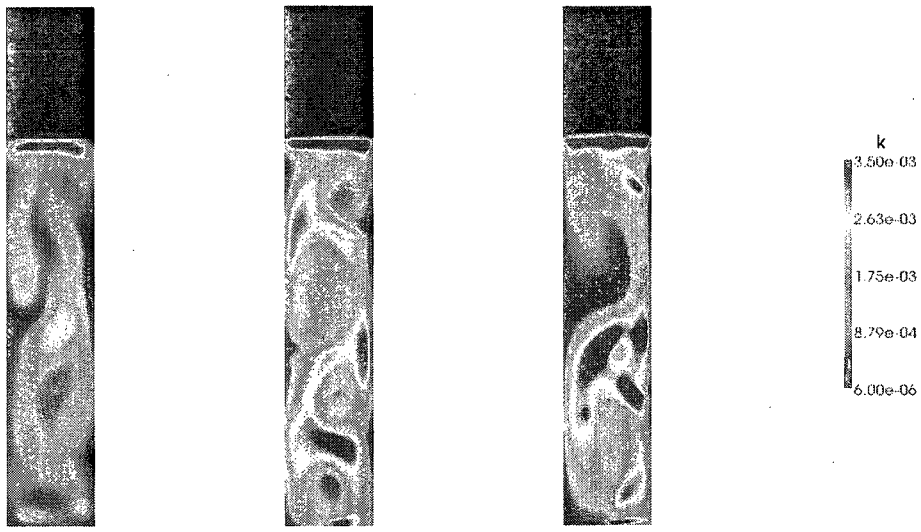

Figure 7.12: Kinetic energy $[m^2/s^2]$ mesh refinement tests in the case of $U_{d,s} = 0.14\ cm/s$ and $H/W = 4.5$. Coarse (left), medium (center), fine (right).

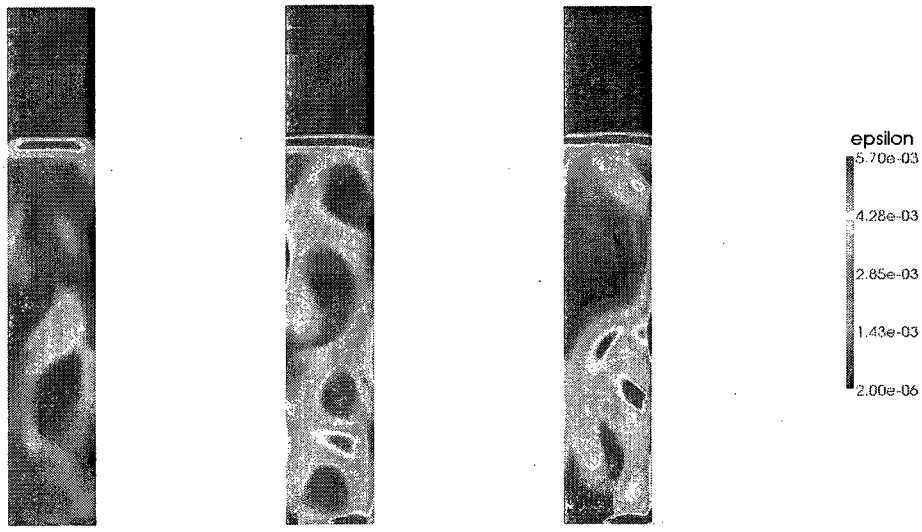

Figure 7.13: Dissipation rate $[m^2/s^3]$ mesh refinement tests in the case of $U_{d,s} = 0.14\ cm/s$ and $H/W = 4.5$ ($H_L = 0.90\ m$). Coarse (left), medium (center), fine (right).

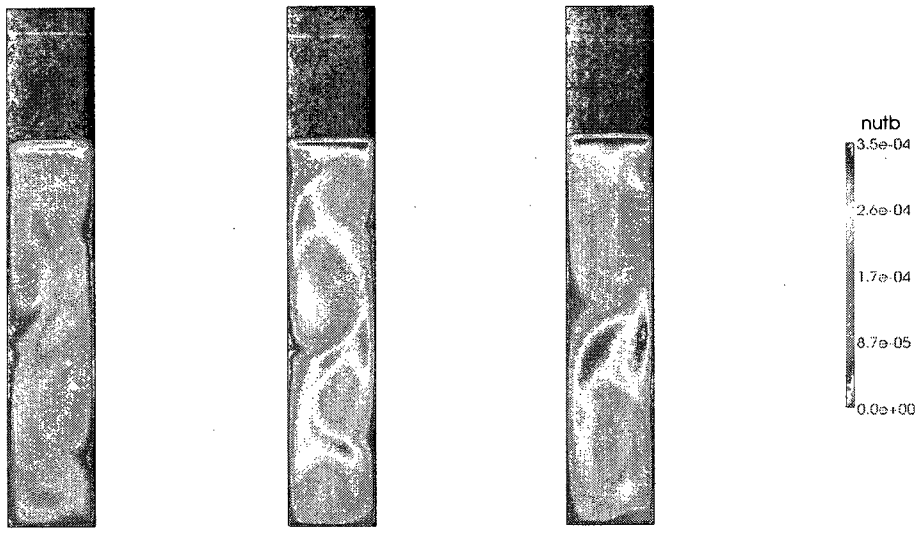

Figure 7.14: Turbulent viscosity $[m^2/s]$ mesh refinement tests in the case of $U_{d,s} = 0.14\ cm/s$ and $H/W = 4.5$. Coarse (left), medium (center), fine (right).

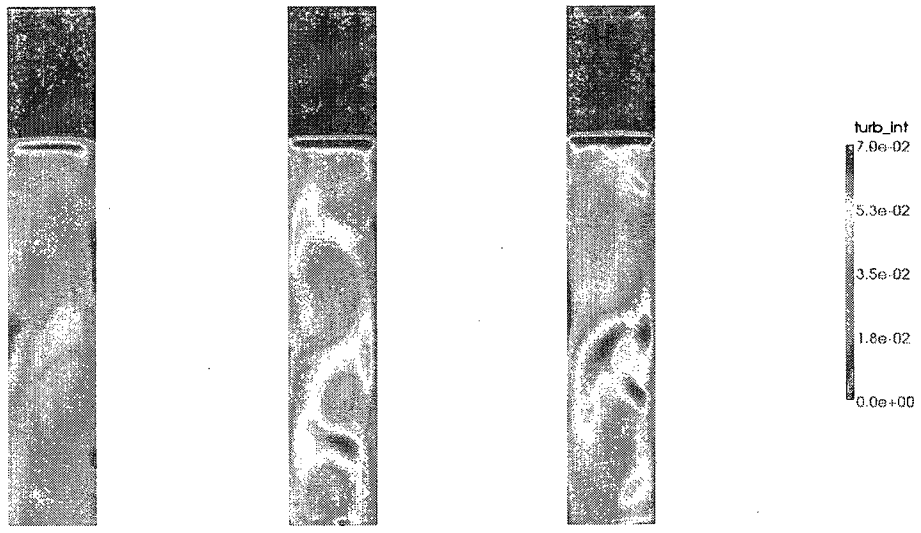

Figure 7.15: Turbulent intensity $[m/s]$ mesh refinement tests in the case of $U_{d,s} = 0.14\ cm/s$ and $H/W = 4.5$. Coarse (left), medium (center), fine (right).

Pfleger and Becker [17], Buwa et al. [133] reported that the agreement between their model and the measurements deteriorates with grid refinement, this is confirmed by the present study. In the case of $H/W = 2.25$ and for a quantitative comparison, the Fig. 7.16, shows the predicted and measured data for vertical liquid velocity. The model's predictions are in good agreement when using the coarse and medium grids, not for the fine grid, the numerical error is greater due to increase by refinement of meshing. In the Fig. 7.16, the better results are obtained also when using the medium grid. When the superficial velocity increases ($U_{d,s} = 0.73\ cm/s$), the model predicts equivalent results for all types of grid mesh and the gas volume fraction profiles are in good agreement with the measurements (see Fig. 7.17).

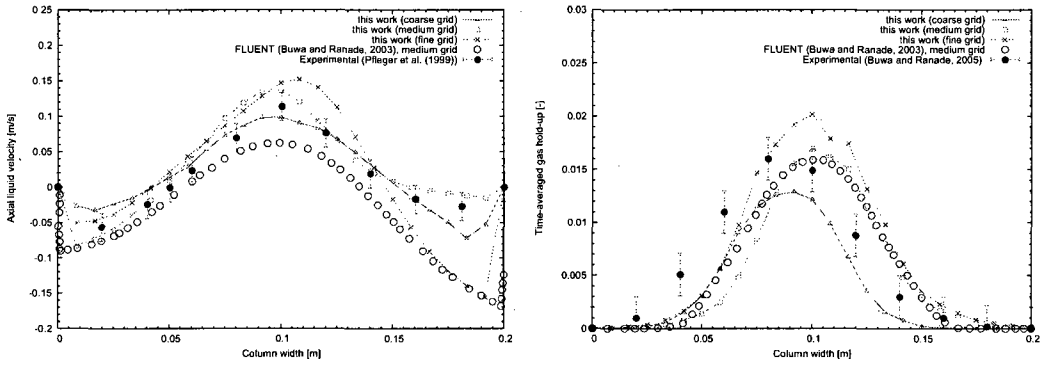

(a) (b)

Figure 7.16: E-E simulation at $H/W = 2.25$, $U_{d,s} = 0.14\ cm/s$ for $Y = 0.37\ m$

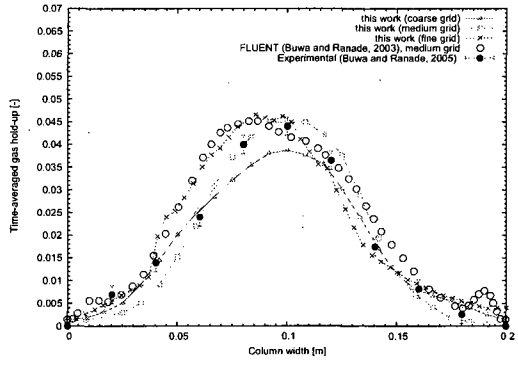

Figure 7.17: Euler-Euler simulation at $H/W = 2.25\ m$, $U_{d,s} = 0.73\ cm/s$ for $Y = 0.37\ m$ from the bottom

In cases $H/W \doteq 4.5$ and $U_{d,s} = 0.14\ cm/s$, the Fig. 7.18 shows that volume fraction profiles are in agreement when using the medium grid. In the case of $U_{d,s} = 0.73\ cm/s$, we can see that all grids give good results in comparison to the experimental results and model of Buwa et al. [134]. So, it appears that in the low superficial gas velocity range the medium grid mesh is more effective than the fine grid. When increasing superficial gas velocity, the difference between grid mesh refinement is not as important. Consequently, the medium mesh grid is chosen in the present study to validate turbulence modelling.

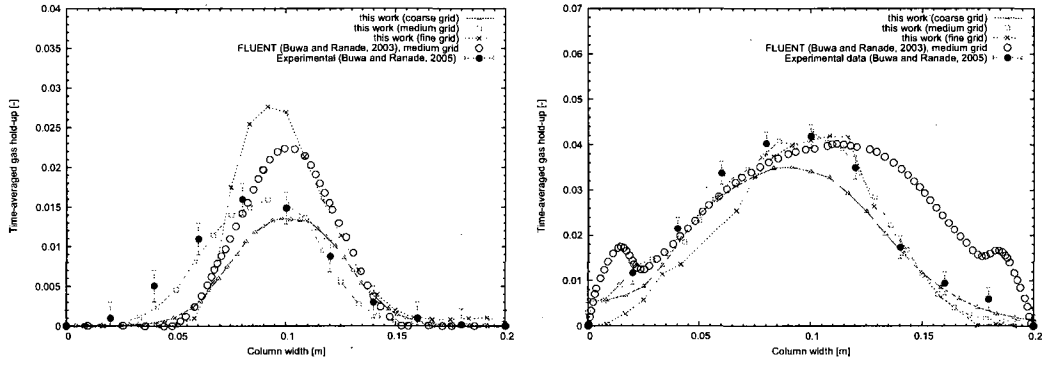

(a) (b)

Figure 7.18: E-E simulation at $H/W = 4.5$. $U_{d,s} = 0.14\ cm/s$ (a) and $U_{d,s} = 0.73\ cm/s$ (b) for $Y = 0.675\ m$

The tables 7.1 and 7.2 gives the percentage difference between three different grid mesh in the case of bubble column. Here the gas hold-up and liquid velocity are choosen to show the quantitative difference and approve our choice of midium grid mesh.

Table 7.1: Percentage difference of gas hold-up values between model and experimental measurement of Buwa et al. [135].

grid definition	Model [-]	Experimental [-]	difference [%]
Coarse	0 - 0.0130		0 - 18.75 %
Medium	0 - 0.0165	0 - 0.016	0 - 3 %
Fine	0 - 0.0210		0 - 23.8 %

Table 7.2: Percentage difference of liquid velocity values between model and experimental measurement of Buwa et al. [135].

grid definition	Model [m/s]	Experimental [m/s]	difference [%]
Coarse	-0.06 - 0.10		16 - 17 %
Medium	-0.08 - 0.13	-0.05 - 0.12	7 - 15 %
Fine	-0.16 - 0.16		25 - 38 %

7.1.2 Flow results visualization: model versus experimental

In this work we propose a new turbulence models for bubble column flows. In order to test and validate the developed model, we define in the table 7.3 three closures A, B and C in which the turbulent transport equations are modeled using the open-source CFD package OpenFOAM.

Table 7.3: Different closures used in bubble column modeling. NC: not considered, C: considered, B.I.T. : bubble induced turbulence

Closure A Robert and Oliver ([49])	Closure B Rusche ([56])	Closure C (Present model)
C_D Schiller-Naumann	C_D Schiller-Naumann	C_D Schiller-Naumann
$C_l = 0.5$	C_l Tomiyama correlation	C_l Tomiyama correlation
$C_{vm} = 0.5$	$C_{vm} = 0.5$	$C_{vm} = 0.5$
Π_ϵ^{dis} NC	Π_ϵ^{dis} C	Π_ϵ^{dis} C
Π_k^{dis} NC	Π_k^{dis} C	Π_k^{dis} C
Π_ϵ^{i} C	Π_ϵ^{i} NC	Π_ϵ^{i} C
Π_k^{i} C	Π_k^{i} NC	Π_k^{i} C
B.I.T. NC	B.I.T. NC	B.I.T. C

In the following we attempt to validate the extended $k - \epsilon$ model proposed earlier.

7.1.3 Results and discussion

The results are compared to the experimental data and previously published results obtained by [134; 135]. The bubble diameter is set to a fixed value of 5 mm in order to validate the turbulence effect on the gas-liquid systems behavior. We are well aware that the size distribution of bubbles could play an important role on the turbulence. In the present thesis, the population balance modelling has been addressed in chapter 6, but is not considered in the turbulence model validation in order to compare the turbulence model with the current state of the scientific literature where turbulence models including PBM are absent.

For the case of $H/W = 2.25$, the comparison of measured [134; 135; 18] and the current model predict time-averaged gas hold-up and vertical liquid velocity profiles is shown in Fig. (7.21) for a superficial gas velocity of 0.14 cm/s. The vertical liquid velocity measured by

Pfleger et al. [18] are presented on Fig. 7.21 (a) with the model's results. Fig. 7.21 (b) shows a comparison of the measured time-averaged gas hold-up Buwa and Ranade [135] and the model's results obtained at a liquid height of 0.37 m from the column bottom. The Fig. 7.22 confirms the good agreement between measured and modelling results for different conditions both for case (a) and (b).

Calculations are also performed with and without the virtual mass force term. It is observed that the time-averaged properties (vertical liquid velocity and gas hold-up) are not sensitive to the virtual mass (see Figures 7.25 and 7.26). They show that the bubbly flows characteristics are not sensitive to the virtual mass force. This observation is confirmed by Buwa and Ranade ([133], [134], [135]) and Joshi [66].

By definition, the virtual mass force can be understood by considering the change in kinetic energy of fluid surrounding an accelerating bubble. The effect of the virtual mass force is much larger for a bubble in liquid than for a drop in gas due to the higher liquid density surrounding the bubble. The virtual mass coefficient is often set to 0.5 for rigid, spherical particles in the literature [23; 22; 123].

To understand the lift force effect on the hydrodynamic of the multiphase flows, the influence of the lift coefficient C_l on the hydrodynamic of gas bubbles is studied. The equation of the lift force is a conventional lift force interpretation based on the relative velocity, liquid velocity gradient and lift coefficient. When a bubble is rising in an infinite medium, the pressure distribution is symmetric and there is no net force in the radial direction. However, when a bubble is rising near the wall, the velocity gradient due to the presence of the wall will increase the pressure at the wall side and generates a net transverse force acting on the bubble Ranade [136]. We examine here the lift force using three closures: The Tomiyama correlation (closure 1), the classical value of 0.5 (closure 2) and without lift force (closure 3). The predicted value using Tomiyama correlation is about 0.288 for a bubble size of 5 mm

(compared to the commonly used value of 0.5 found in the literature; for example, see Joshi [66]). Note that Buwa and Ranade have used a value of 0.28 in their modeling of bubble column. Based on the previously published work of Buwa and Ranade [134], we investigate the effect of the lift force using the different closures cited above. In the case of $H/W = 2.25$ (low liquid level), the figures 7.23 (a) and (b) show that the Tomiyama correlation (closure 1) appears to give better results in comparison with the other closures. As the lift force depends on the velocity gradients in the liquid phase the effect of the lift force becomes evident in the case of $H/W = 4.5$ (high liquid level) for two different superficial gas velocity at 0.14 cm/s and 0.73 cm/s as is shown in the figures 7.24 (a) and (b). The results obtained with the Tomiyama [4] correlation are in good agreement with the measurements of Buwa and Ranade [135].

Based on the work of Robert and Oliver [49], the drift velocity accounts for the dispersion of bubbles due to transport by turbulent fluid motion. The drift velocity scales the fluid viscous force against the surface tension force. Due to correlation between the distribution of bubbles and the turbulent fluid motion (see Robert and Oliver [49]), U_{drift} represents the dispersion of the bubbles due to transport by fluid turbulence. This is an important effect since the mass balance does not contain a diffusive term that would be responsible for the dispersion of bubbles. Figures (7.27, 7.28) show the results obtained with the proposed model with different correlations from the literature, compared to experimental results. The predicted profiles of gas hold-up and liquid velocity are clearly improved when using the drift velocity.

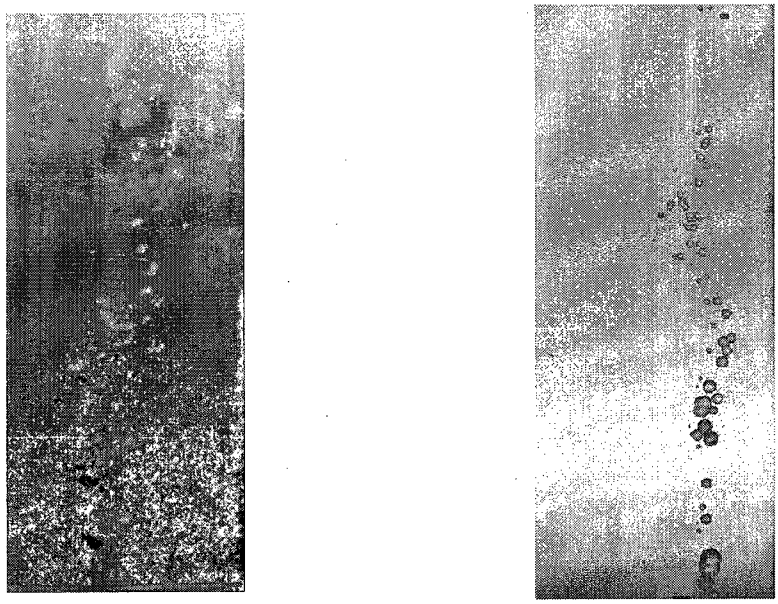

(a) (b)

Figure 7.19: Qualitative comparison of bubbles behavior between experimental results (a) and present model (b). Conditions are $H/W = 2.25$, $U_{d,s} = 0.14\ cm/s$.

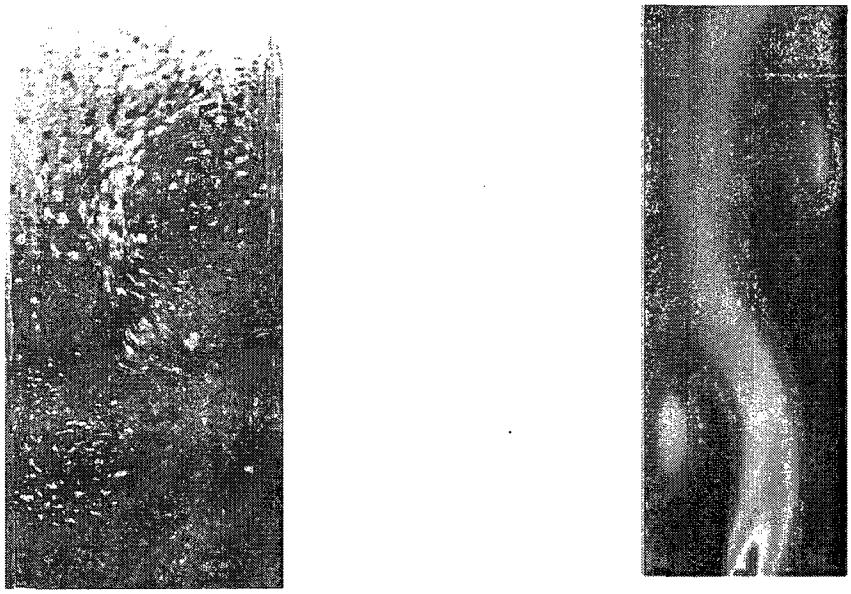

(a) (b)

Figure 7.20: Qualitative comparison of gas volume fraction between experimental results (a) and present model (b). Conditions are $H/W = 4.5,\ U_{d,s} = 0.73\ cm/s$.

The computational results published by Buwa et al. [132] and the predictions of the current model are shown in figures 7.19 and 7.20. Predicted instantaneous bubbles and gas volume fraction distribution show that meandering motion of the bubble plume is captured in satisfactory qualitative agreement with experiment.

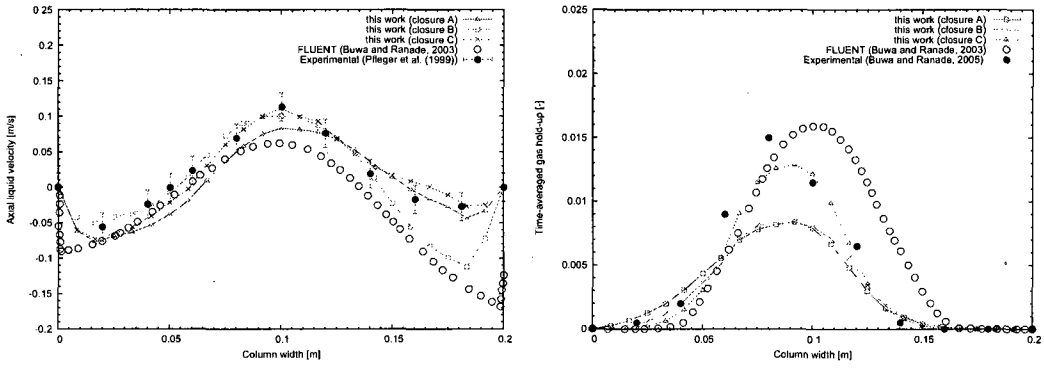

(a) (b)

Figure 7.21: E-E simulation at $H/W = 2.25$, $U_{d,s} = 0.14\ cm/s$ for $Y = 0.37\ m$

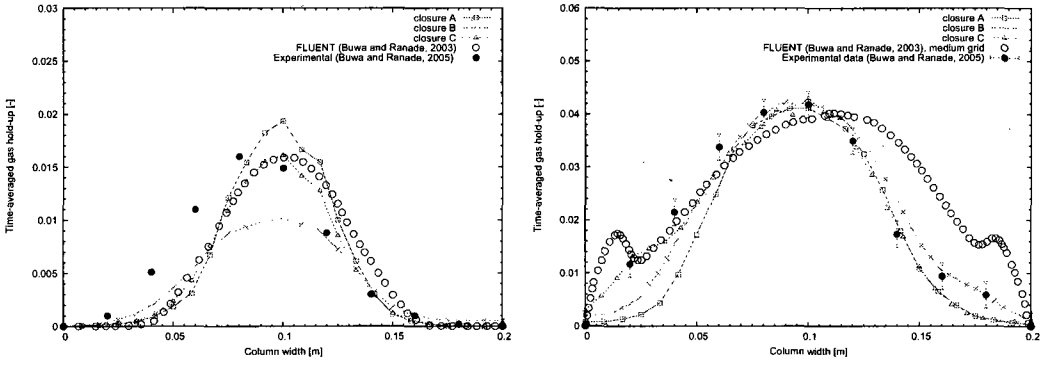

(a) (b)

Figure 7.22: E-E simulation at $H/D = 4.5$. $U_{d,s} = 0.14\ cm/s$ (left) and $U_{d,s} = 0.73\ cm/s$ (right) for $Y = 0.675\ m$

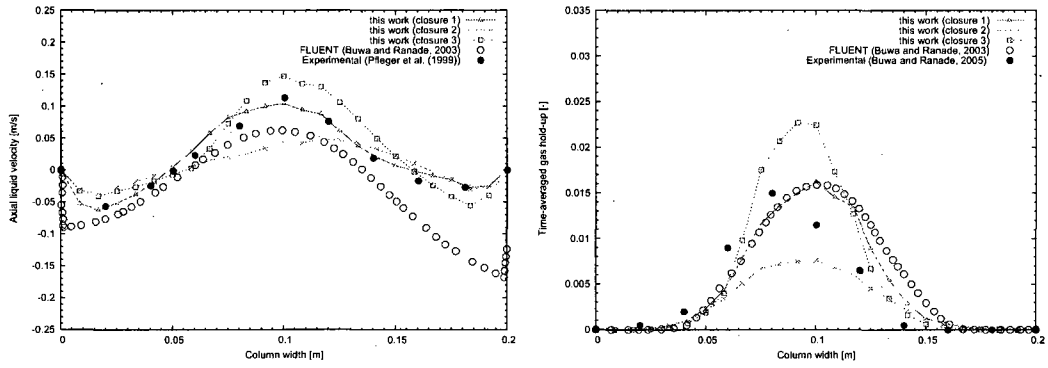

(a) (b)

Figure 7.23: E-E simulation at $H/W = 2.25$, $U_{d,s} = 0.14\ cm/s$ for $Y = 0.37\ m$

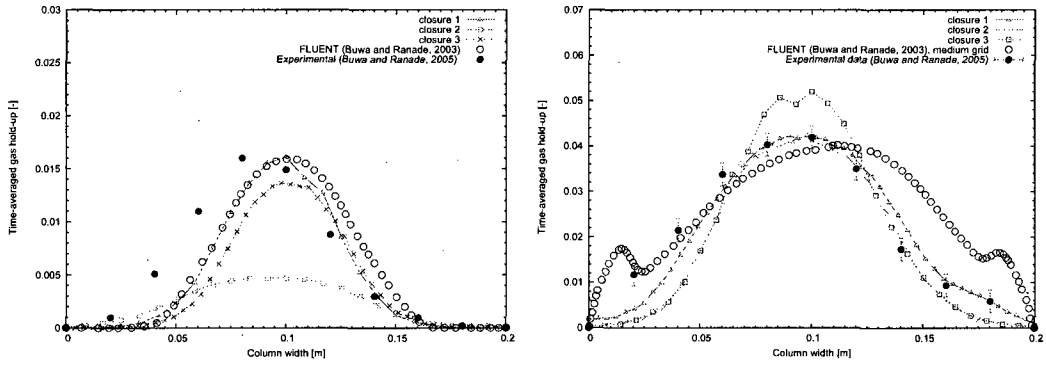

(a) (b)

Figure 7.24: E-E simulation at $H/W = 4.5$. $U_{d,s} = 0.14\ cm/s$ (left) and $U_{d,s} = 0.73\ cm/s$ (right) for $Y = 0.675\ m$

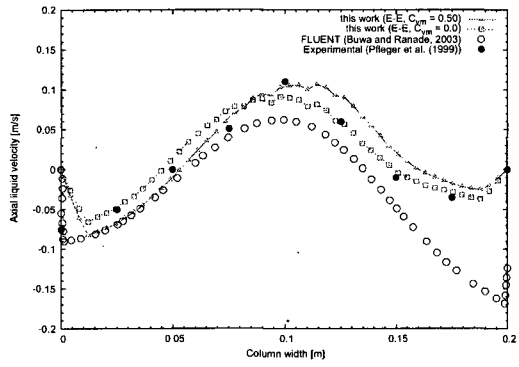

(a)

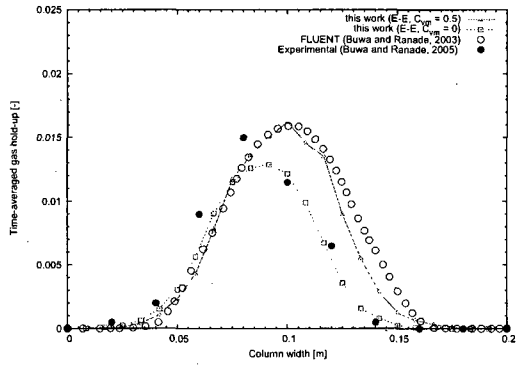

(b)

Figure 7.25: E-E simulation at $H/W = 2.25$, $U_{d,s} = 0.14\ cm/s$ for $Y = 0.37\ m$

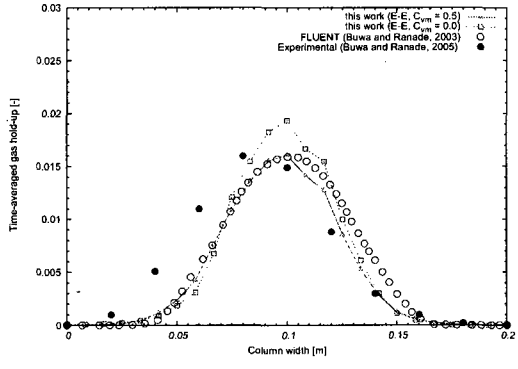

(a)

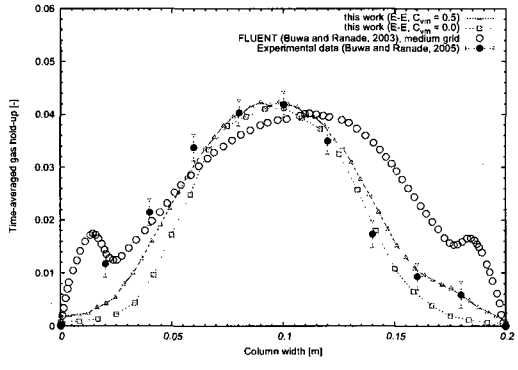

(b)

Figure 7.26: E-E simulation at $H/W = 4.5$, $U_{d,s} = 0.14\ cm/s$ (a) and $U_{d,s} = 0.73\ cm/s$ (b) for $Y = 0.37\ m$

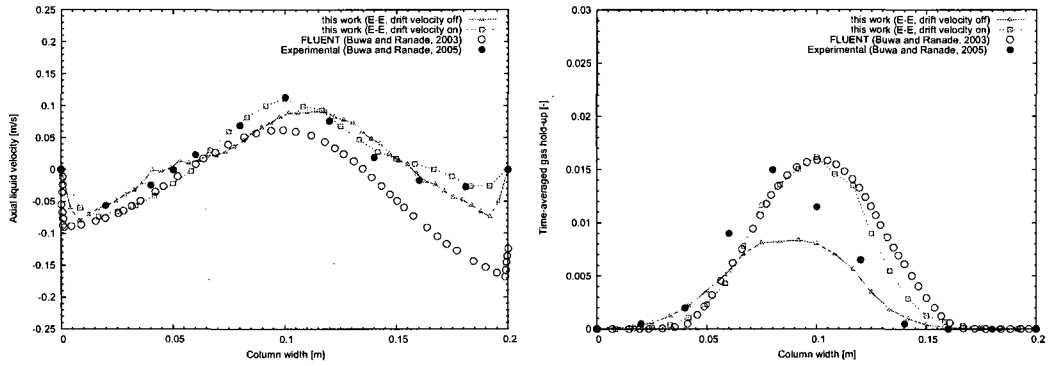

(a) (b)

Figure 7.27: E-E simulation at $H/W = 2.25$, $U_{d,s} = 0.14\ cm/s$ for $Y = 0.37\ m$

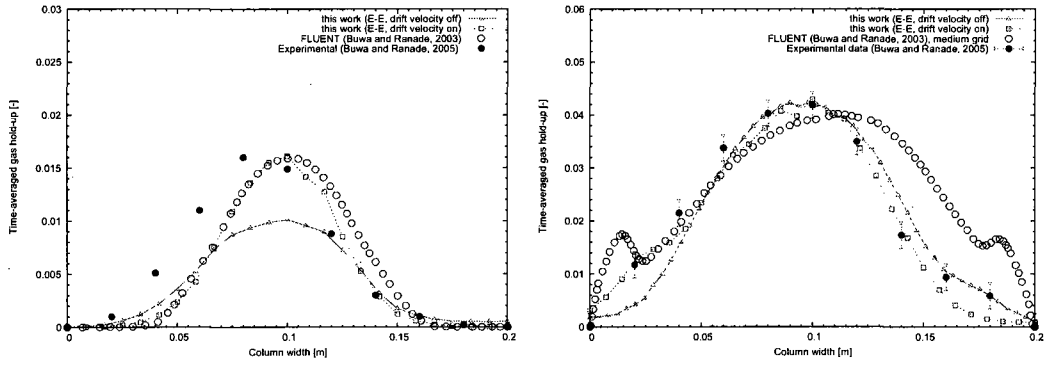

(a) (b)

Figure 7.28: E-E simulation at $H/W = 4.5$. $U_{d,s} = 0.14\ cm/s$ (left) and $U_{d,s} = 0.73\ cm/s$ (right) for $Y = 0.675\ m$

7.2 Conclusion

The hydrodynamic behavior of gas-liquid flows in bubble columns is studied and explained using an Eulerian-Eulerian formulation. The predicted gas hold-up and phases velocities profiles are in good agreement with the available measurements. The addition of source terms in the standard $k-\epsilon$ model of turbulence to take into account certain aspects of turbulence specific to two-phase flows is found to be adequate and satisfactory. The effect of the so-called drift velocity is studied using different correlations available in the scientific literature.

7.3 Part II: Population balance modelling

In this second part, the population balance equation is added to the model and solved using the Direct Quadrature of MOments Method (DQMOM) and the Class Method (CM). The following algorithm shows the steps of population balance modelling. The Fig. 7.29 show the PBE-CFD equations coupling for bubbly flows and are implemented in the open source package OpenFOAM. First, the turbulence properties are updated and it is followed by the calculation of axial liquid and gas velocities, pressure correction and velcoity correction in that order. The next step is the solution of equations for $k-\epsilon$ model. Finally, the bubble size distribution is calculated by the solution of population balance equation.

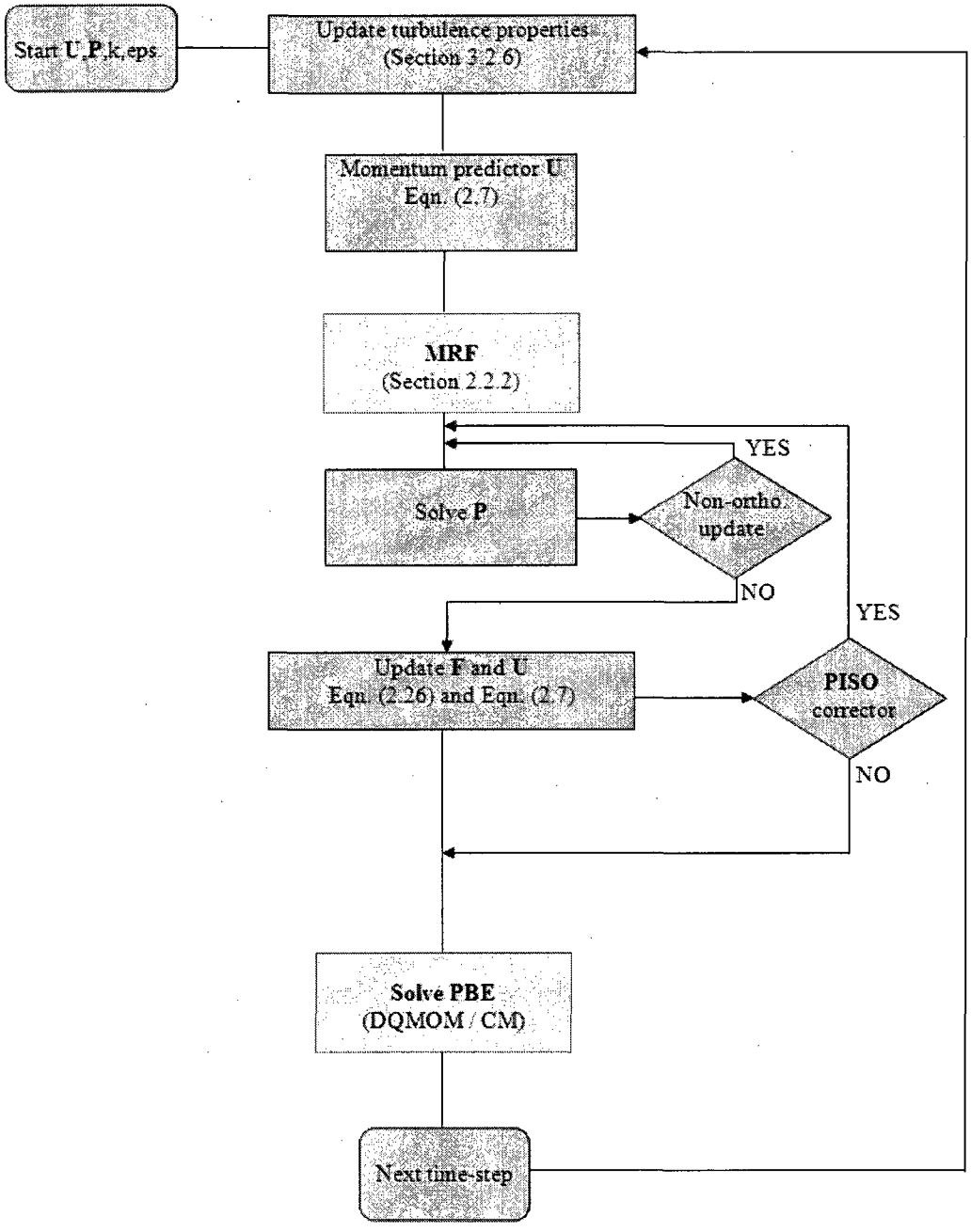

Figure 7.29: **PISO** solution procedure coupled with **PBE** and **MRF** technique

7.3.1 Test case A: Bubble Column

Gas-liquid reactors in the form of bubble columns have an enormous importance in the process and associated industries. Hence, they received considerable attention, both in terms of experimental and theoretical efforts. For bubble columns, a number of experimental data sets are available from the literature, which contain local measurements of velocities, phase fraction, bubble size and often turbulence quantities. Some of these extend to very high phase fractions ($> 40\%$). These have been utilized by a number of authors [63; 119; 58; 59; 137; 10] as test cases in their numerical studies.

Setup

The bubble column used in the experimental study of Pfleger et al. [18] has been modeled to carry out the investigations. The apparatus is a rectangular laboratory-scale bubble column with the dimensions 20×120×5 cm (W×H×D) and is filled with two different levels of water $H/W = 2.25$ and $H/W = 4.5$. Air is introduced into the system through a perforated section of (0.6×1.8 cm) in the xz plane. The Fig. 7.30 show the rectangular bubble column used here to validate the population balance modelling using the direct quadrature method of moments and the method of classes. The geometry is meshed using OpenFOAM package and the grid medium is choosen to validate predicted results as described in the latest section. The porosity of the perforated section is calculated as:

$$Porosity = \frac{Area_{section}}{Area_{plate}} \approx 0.0108 \tag{7.1}$$

Then, the resulting superficial gas velocity is calculated by

$$U_{d,s} = Porosity \times U_{d,in} \tag{7.2}$$

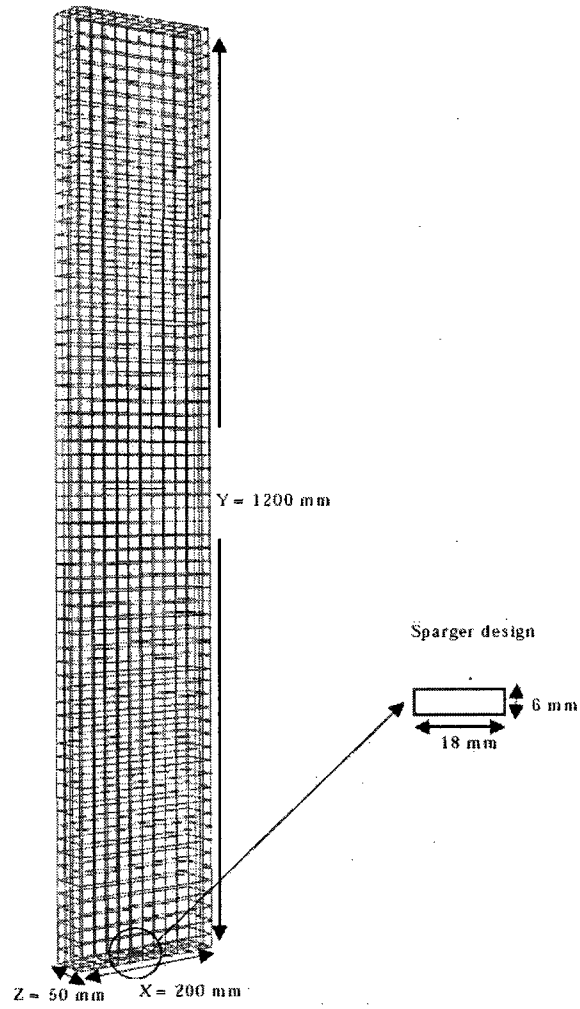

Figure 7.30: Rectangular laboratory-scale bubble column (right) and perforated section inlet (left).

The gas-liquid flow is modelled using the two-fluid model Euler-Euler approach (see Chapter 3); the initial bubble size at the inlet is set to 5 mm as used by Buwa and Ranade [135].

The domain is discretized into 16×96×4 control volume giving a total of 6144 cells. The time step is set to $\Delta t = 0.01\ s$ resulting in a maximum Courant number between $Co = 0.40$ and 0.70 depending on the gas flow rate.

In order to validate the model, the data available in the literature [17; 132; 90] are used for qualitative and quantitative comparison. The bubble column geometry is same as that used by Pfleger et al. [18]. As in the experiments of Buwa and Ranade [135], the air-water system is chosen and the superficial gas velocity is varied from 0.14 to 0.73 cm/s (corresponding 12 to 67 cm/s used as inlet-velocity in the model). Two closures A and B are used to validate the predicted results with measurements data, in the first one (closure A), the population balance equation is solved using the method of classes (CM), and in the second closure (B), the direct quadrature method of moments (DQMOM) is used to solve the PBE.

In method of classes used in the tested case of bubble column, the bubbles are divided into $n = 2r + 1$ classes Bannari et al. [102], with n add in order to have symmetry. As described before (see details in Bannari et al. [102]) a distribution on pivoted grid point x_i with $x_{i+1} = sx_i$ and a value of $s > 1$ is used, where i refer to the class index. With the assumption of spherical bubbles, the following formulation can be written as $(4/3)\pi(d_{i+1}/2)^3 = (4s/3)\pi(d_i/2)^3$. In this relation, s is calculated to ensure that $d_n = d_{2r+1} = d_{max}$ and $d_r = d_mean$. This gives the following relation:

$$d_i = s^{(i-r-1/3)} d_{mean} \tag{7.3}$$

and

$$s = \left(\frac{d_{max}}{d_{mean}}\right)^{3/r} \tag{7.4}$$

Table 7.4: Values of s and the corresponding classes used with CM

Number of classes	7	15	25
Value of r	3	7	12
Value of s	2	1.3459	1.1892

In this study, the initial inlet bubble diameter is set to 5 mm as in Buwa and Ranade [133] and Buwa et al. [132]. The Table 7.4 gives the value of s used with the corresponding class. At the inlet, the mean diameter is used, and the same gas velocity is considered for all size groups. This assumption is applied because of its simplification to reduce the gas phase momentum equations to a single as described above in this work. Laakkonen et al [79] found that more than 80 classes should be used to minimize the discretization errors. However for practical reasons (i.e. to reduce the computational effort) the number of classes was limited to 25 as shown in table 7.4.

Results

As expected, population balance of bubble size distribution gives better agreement than a single bubble size. In the test cases for 7, 15 and 25 classes, the last two gives better results by comparison with the data of Buwa and Ranade [135]. In the tested cases for $H/W = 2.25$ and $H/W = 4.5$ at two different gas flow rates, the predicted liquid velocity and gas hold-up profiles are shown in Fig. 7.33 and Fig. 7.34. To predict the Sauter mean diameter, we use the direct quadrature method of moments DQMOM. Until now, this technique has not been tested and validated on bubbles size distribution in presence of complex phenomena such as coalescence and breakage due to bubble-bubble interactions. The figures 7.31 and 7.32 show the predicted results obtained with CFD package OpenFOAM. In the Fig. 7.31, DQMOM and 25 classes give better agreement between them in term of a qualitative comparison. The Fig. 7.32 comme to confirm this interpretation.

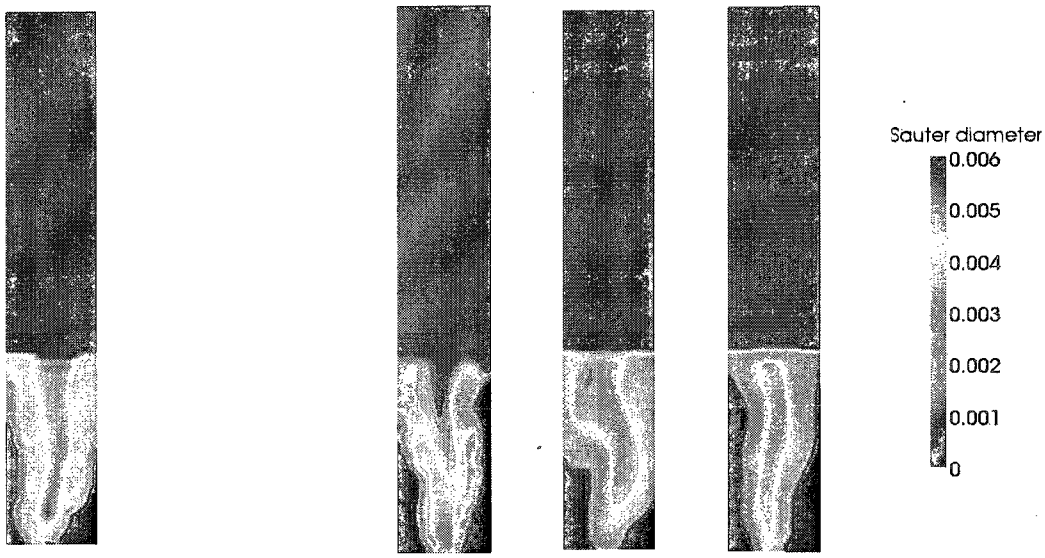

DQMOM 7 classes 15 classes 25 classes

Figure 7.31: Predicted Sauter mean diameter using DQMOM and the method of classes (from left to right). In this case of $H/W = 2.25$ and $U_{d,s} = 0.14\ cm/s$.

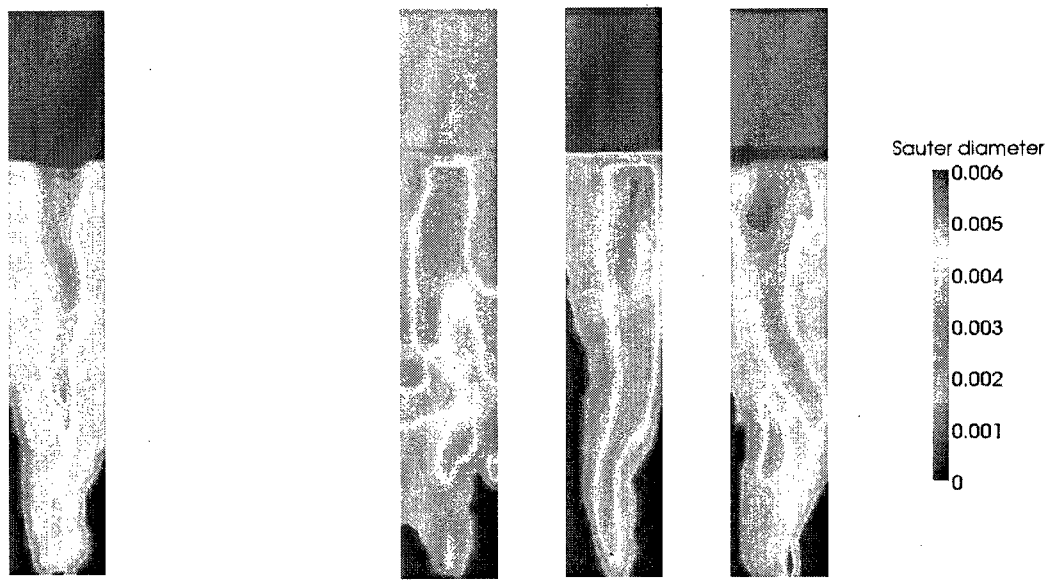

DQMOM 7 classes 15 classes 25 classes

Figure 7.32: Predicted Sauter mean diameter using DQMOM and 7, 15, 25 different classes (from left to right). In this case of $H/W = 4.5$ and $U_{d,s} = 0.14\ cm/s$.

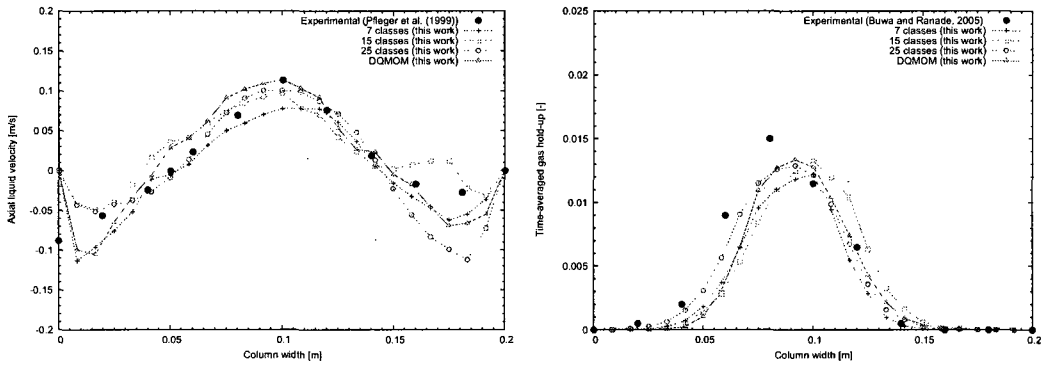

Figure 7.33: Liquid velocity (left) and gas hold-up (right) profiles using the present model. $H/W = 2.25$, $U_{d,s} = 0.14\ cm/s$ for $Y = 37\ cm$ from the bottom.

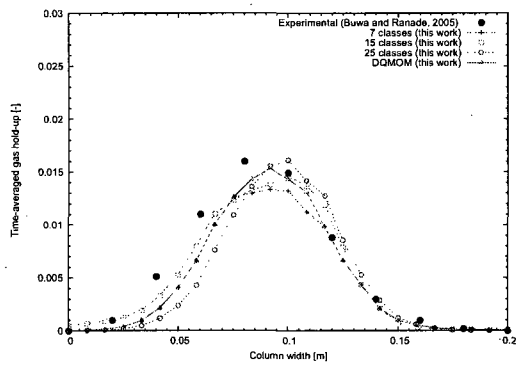

Figure 7.34: Gas hold-up (right) profiles using the present model. $H/W = 4.5$, $U_{d,s} = 0.14\ cm/s$ for $Y = 37\ cm$ from the bottom.

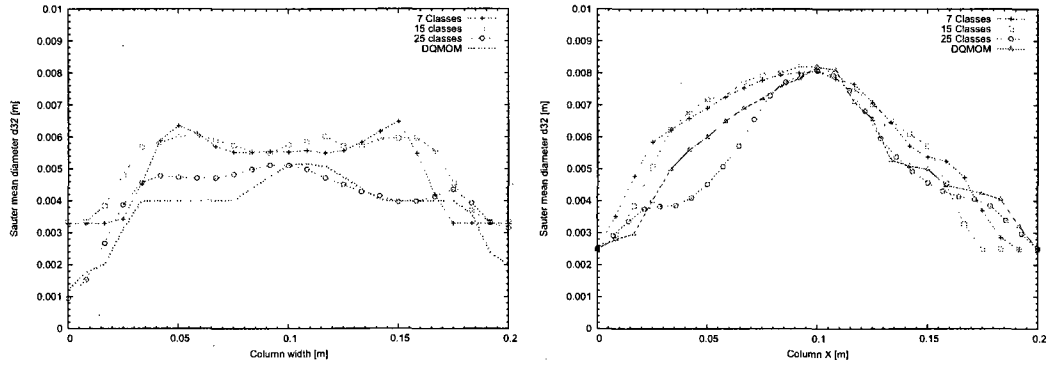

Figure 7.35: Sauter mean diamgter profiles using the present model. $H/W = 2.25$, $U_{d,s} = 0.14\ cm/s$ (left) and $H/W = 4.5$, $U_{d,s} = 0.14\ cm/s$ (right).

The Fig. 7.35 show the predicted Sauter mean diamter using DQMOM and CM with different number of calsses at an H/W ratio of 2.25 (left) and 4.5 (right). The obtained results confirm that the DQMOM is in good agreement when increasing the number of classes. The use of **DQMOM** permits to predict a bubble size distribution (BSD) at any time and position in the case of bubble column ($H/W = 2.25$ and $U_{d,s} = 0.14\ cm/s$). The figures 7.36, 7.37, 7.38 and 7.39 show a sample of these distribution. Note that, the abscisas L_i and weights w_i are equivalent to bubble size and volume fraction respectively. The figures 7.40 and 7.41 show the percentage of volume of the classes in the bubble column obtained using CM at t–60 s.

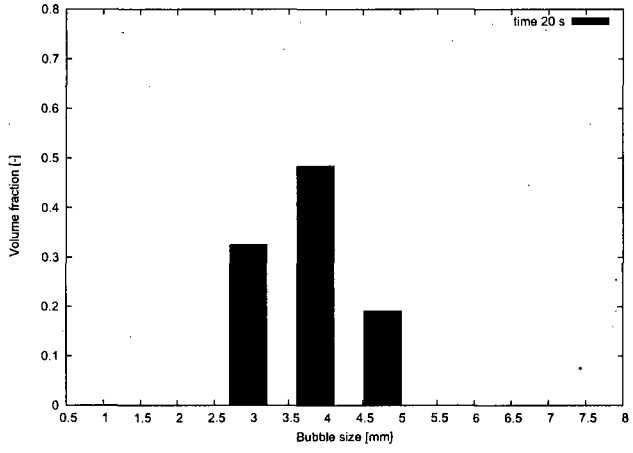

Figure 7.36: Bubble size distribution using DQMOM in time $t = 20s$ and position of $(0.1 \times 0.37 \times 0.025)m$.

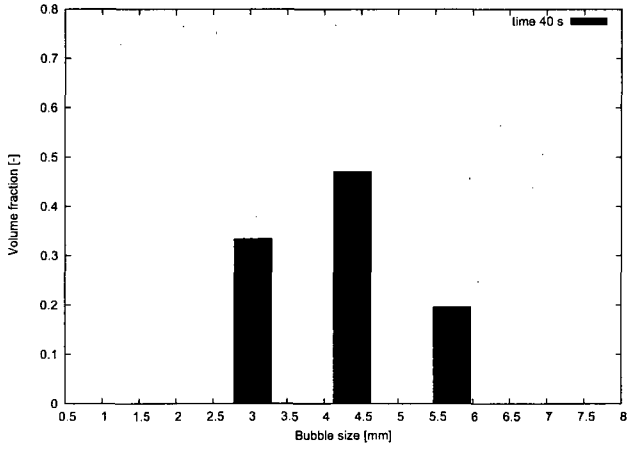

Figure 7.37: Bubble size distribution using DQMOM in time $t = 40s$ and position of $(0.1 \times 0.37 \times 0.025)m$.

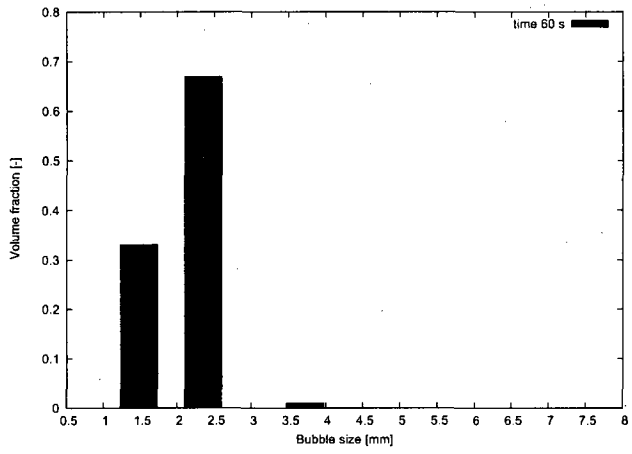

Figure 7.38: Bubble size distribution using DQMOM in time $t = 60s$ and position of $(0.1 \times 0.37 \times 0.025)m$.

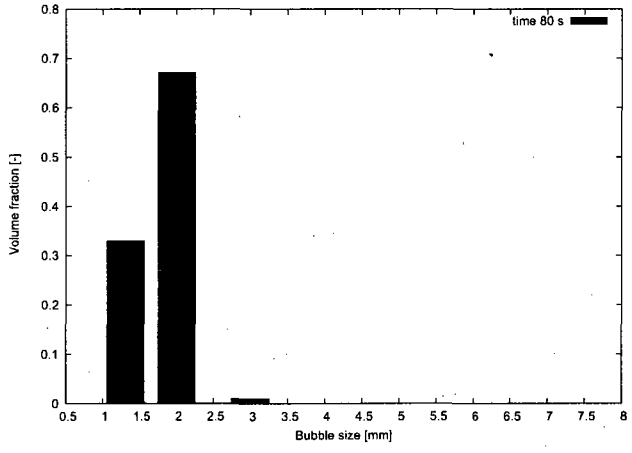

Figure 7.39: Bubble size distribution using DQMOM in time $t = 80s$ and position of $(0.1 \times 0.37 \times 0.025)m$.

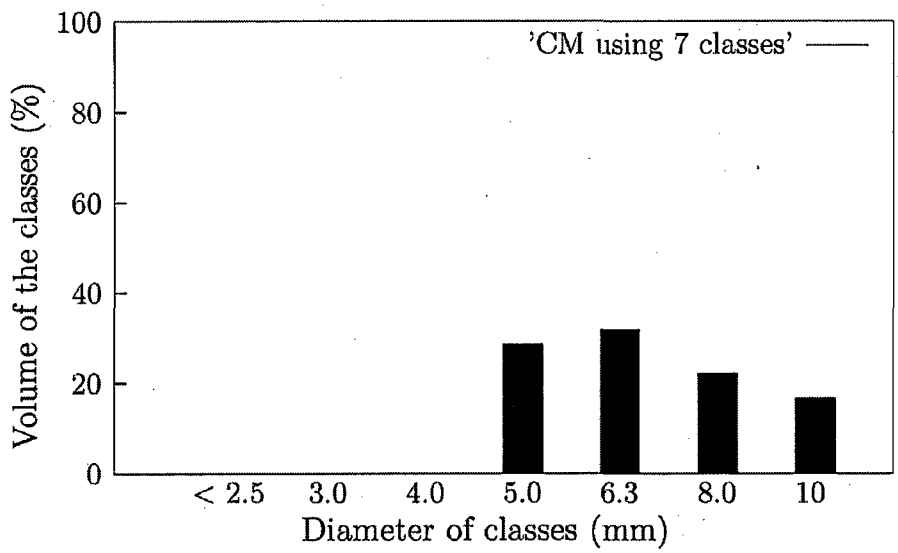

Figure 7.40: Bubble size distribution using CM (7 classes) in time $t = 60s$ and position of $(0.1 \times 0.37 \times 0.025)m$.

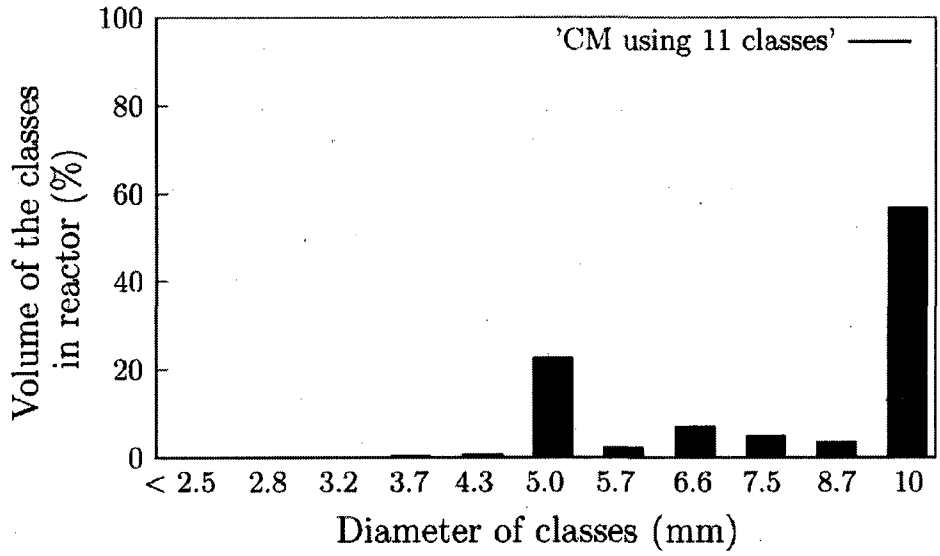

Figure 7.41: Bubble size distribution using CM (15 classes) in time $t = 60s$ and position of $(0.1 \times 0.37 \times 0.025)m$.

Discussion

The model developed shows that in the case A (bubble column), good agreement is obtained when the direct quadrature method of moments (DQMOM) is used and the results are compared with the available experimental results as well as the method of Classes (CM). It performs much better than using a constant bubble size while requiring only marginally higher computational effort, When using the method of classes, both the 15 classes and 25 classes are in agreement with the experimental results but as expected the 25 classes is more accurate, though it requires a significant computational effort. In a previous study Bannari et al. [102], the authors showed that for a given geometry of bubble column flow reactor a good compromise between computational effort and precision the 15 classes choice was a good choice for solving the population balance equation but other authors mention that up to 80 classes could be necessary to obtain sufficient accuracy. In order to have a method that represents adequately the population without the large computational effort associated with such a large number of additional equations, the DQMOM appears as a very interesting solution method.

7.3.2 Test case B: Double-turbine Stirred-tank Reactor

In this section, we attempt to validate the application of DQMOM for bubble coalescence-breakup phenomena. Until now, no studies have been made in this domain apart from a few studies made on the aggregation and fragmentation of solid particles (in the scale of nano and micro), for example see [107; 33]. However, the error generated by the application of DQMOM in the scale of millimeter (our case) is greater and a direct application of DQMOM is not recommanded to describe the bubbles size distribution.

Table 7.5: Transport properties

Fluids	Density (kg/m^3)	Dynamic viscosity ($Pa.s$)	Surface tension (N/m)
Water (20^oC)	998.2	1.0×10^{-3}	0.073
Air (20^oC)	1.225	1.7894×10^{-5}	-

Setup

The experimental set-up of Alves et al. [127; 126] is used. The solution domain is shown in Fig. 7.42. It consists of a flat bottom stirred cylindrical vessel with diameter T of 0.292 m and liquid height H = 2T . A double six bladed standard Rushton impellers with diameter of D = T/3 were located respectively at 0.146 and 0.438 m above the tank base. The impeller blade width, l, and the impeller blade height, w, are equal respectively to D/4 and D/5. The tank is equipped with four baffles of 0.1T width uniformly spaced around the periphery. Gas is supplied through a small sparger, which is located between the tank base and the lower impeller Kerdouss et al. [44]. The model results are compared to the experimental data of Alves et al. [127] for a stirred tank filled with tap water with a total height of 0.584 m, gas flow rate of 1.67×10^4 m^3/s and an impeller rotation speed of 7.5 s^{-1} corresponding to a turbulent Reynolds number, $Re = \rho_c N D^2/\mu_c = 7.1 \times 10^4$. The water and gas properties are set in the Table 7.5.

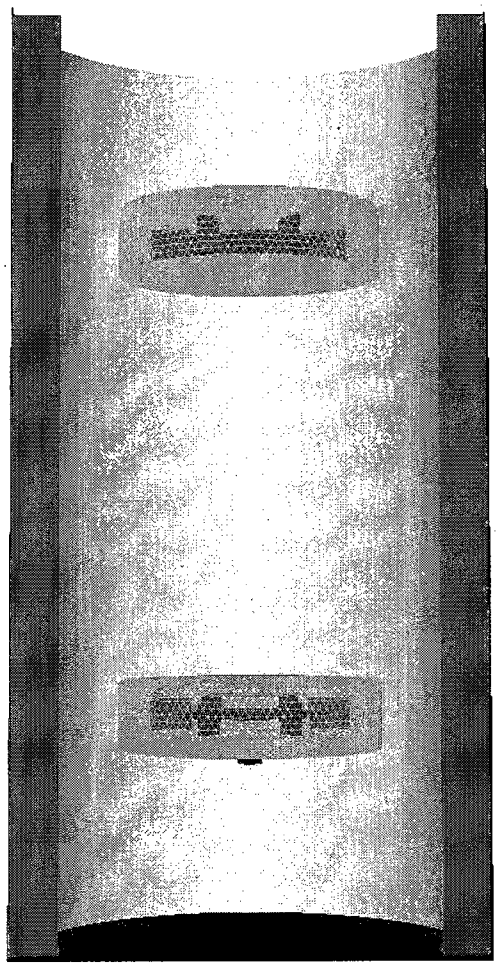

Figure 7.42: Solution domain used. The model is solved on the discretized geometry.

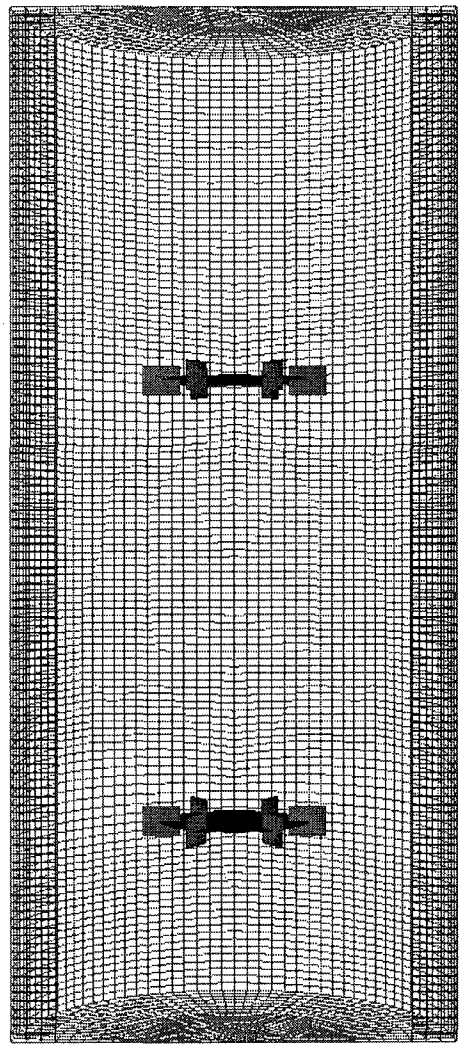

Figure 7.43: Structured mesh grid used in the present model.

d_{32}, denote the Sauter mean diameter predicted by using the DQMOM and CM described in last section.

In the case of CM as used by Kerdouss et al. [45], the Sauter diameter d_{32} is calculated by combining Eqn. (7.5) and Eqn. (7.6) described as follows:

$$n = \frac{6\alpha_d}{\pi d_{32}^3} \tag{7.5}$$

and

$$\frac{\partial n}{\partial t} + \nabla \cdot \left(n\overrightarrow{\mathbf{U}_d} \right) = S_{br} - S_{co} \tag{7.6}$$

n, is the bubble number density. S_{br} and S_{co} are respectively the bubble breakage and coalescence rates. Following Wu et al. [100] bubble break-up rate can be written as

$$S_{br} = C_{br} n \frac{(\epsilon d)^3}{d_{32}} \left(1 - \frac{We_{crit}}{We} \right)^{1/2} Exp\left(- \frac{We_{crit}}{We} \right) \tag{7.7}$$

and the coalescence rate is given by:

$$S_{co} = C_{co} \eta_{co} d^2 (\epsilon d)^{1/3} n^2 \frac{1}{(1 - \alpha_d^{1/3})} \tag{7.8}$$

where $C_{br} = 0.075$ and $C_{co} = 0.05$ are adjustable parameters fitted to the experimental data of Alves et al. [127]. η_{co} is the coalescence efficiency set to unity [100; 52]. We is the Weber number defined as

$$We = \frac{\rho_c u_t^2 d}{\sigma} \tag{7.9}$$

where We_{crit} is the critical value of the Weber number, and is set to 1.2 Kerdouss et al. [44]. The velocity of eddies u_t is given by

$$u_t = 1.4(\epsilon d)^{1/3} \tag{7.10}$$

In the case of DQMOM, d_{32} is determined by the following formula

$$d_{32} = \frac{m^{(3)}}{m^{(2)}} \tag{7.11}$$

where $m^{(3)}$ and $m^{(2)}$ represent the first lower order moments.

Results

In this study, the modeling of the agitated reactor with double turbine is made under the same boundary conditions summarized in the Table 3.3.

All the forces of drag, lift and virtiual mass are considered in this model and predicetd results a qualitative comparison is made in this section. The Fig. 7.44 show the predicted results of Sauter mean diameter using the two techniques DQMOM and CM for solving the population balance equation.

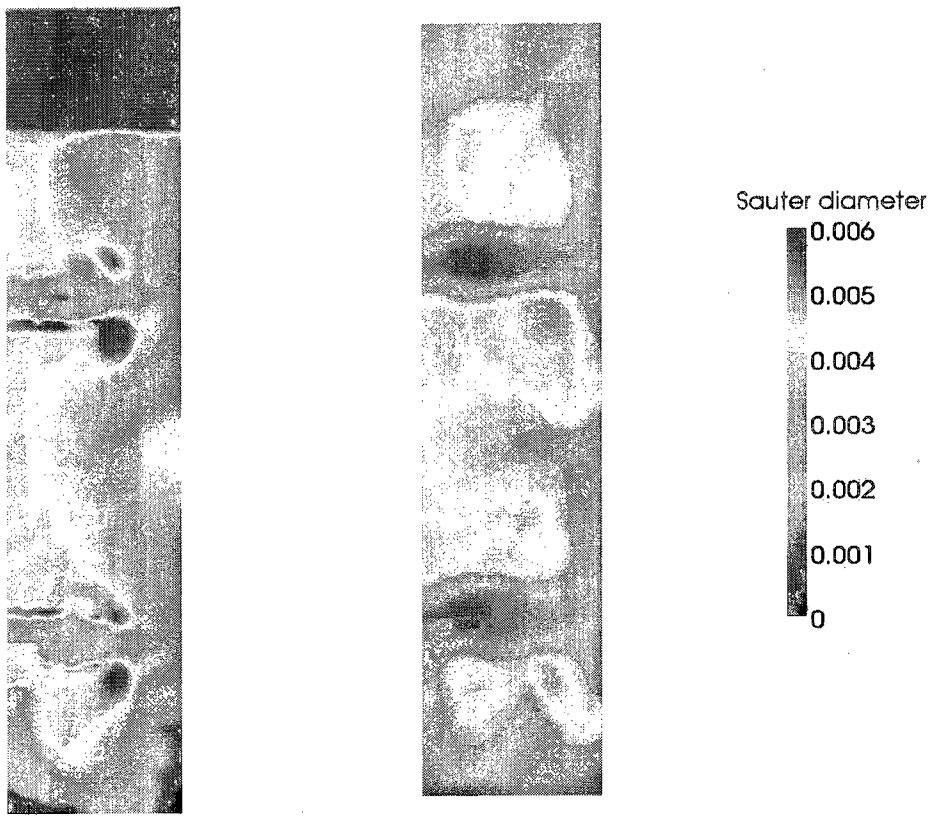

Figure 7.44: Contours of Sauter mean diameter at the mid plane (z=0) using **DQMOM** (left) and **CM** (right). The values of d_{32} are between 1 and 6 mm (blue to red color).

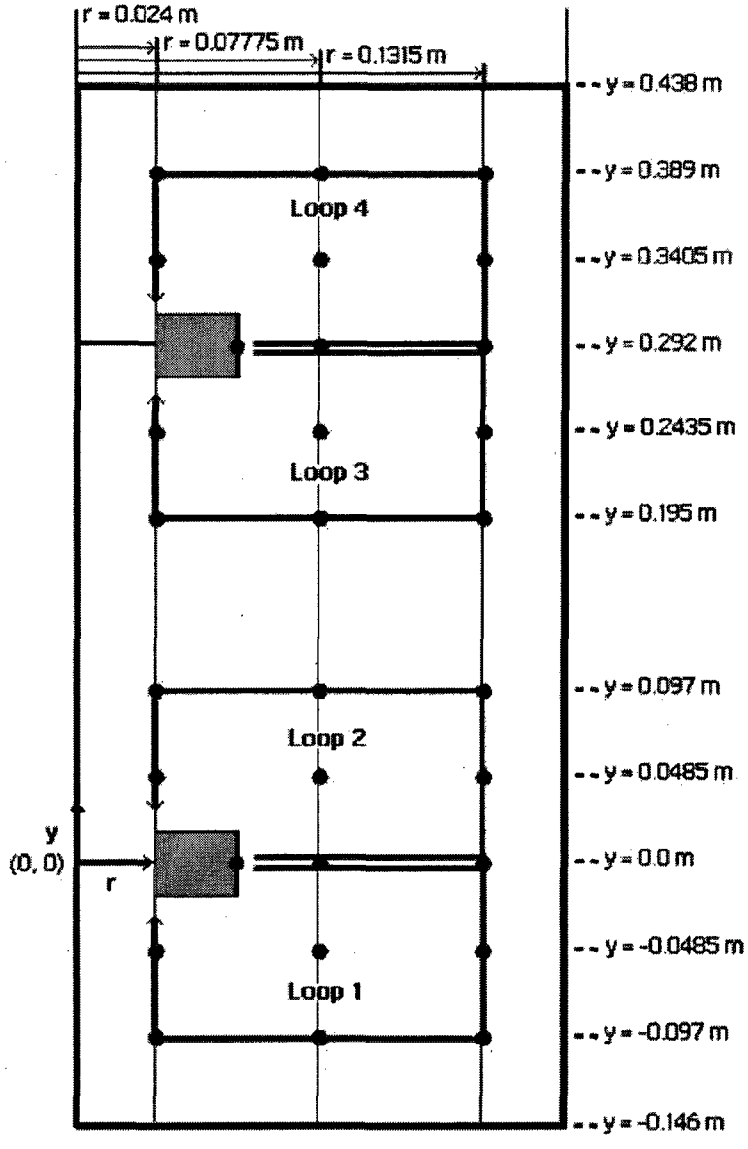

Figure 7.45: Identification of different loops and radial positions by Alves [126].

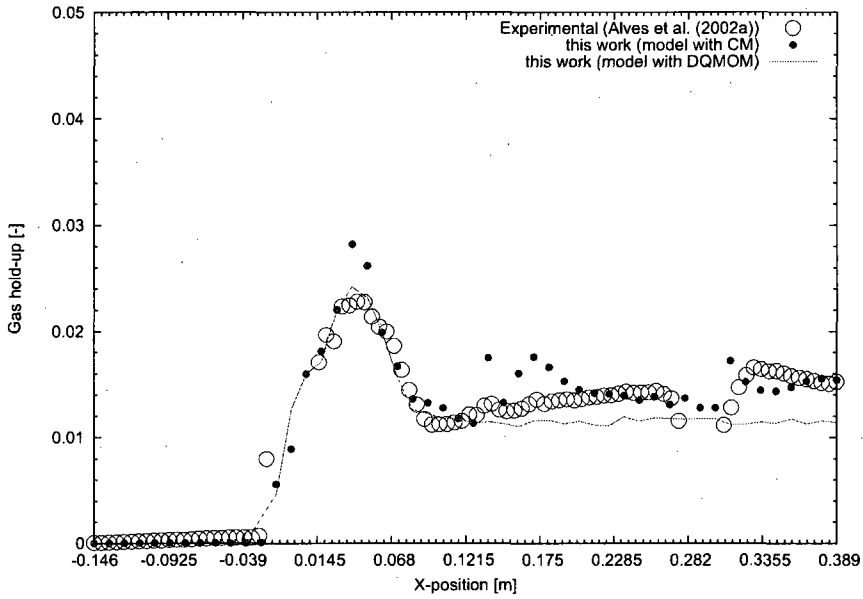

Figure 7.46: Predicted gas hold-up using DQMOM and CM ($r = 2.4\ cm$).

Figures 7.46, 7.47 and 7.48 show the predicted gas hold-up in a horizontal planes at three different radial position: $r = 0.024\ m$, $r = 0.07775\ cm$ and $r = 0.1315\ cm$. Figures 7.49, 7.50, 7.51 and 7.52 show the predicted local bubble mean diameter d_{32} in a vertical mid-plane between two baffles as these 'loops' were defined in the work of [127] . These figures show quantitative comparison between the modeling results and measurements Alves et al. [127]. In the loops 2 and 4, the surface mean diameter increases because coalescence dominate breakage in these circulation zones. In loop 3, a large bubble size is found (5.3 mm), this is caused by the local build-up of air trapped in the circulation zone located between impellers. Also in the first loop, the bubble size increases in this zone due to the position of the gas sparger (inlet) and gas build-up. The predicted results are in good agreement, as well with the measurements as other modeling results from the literature [127; 126; 44].

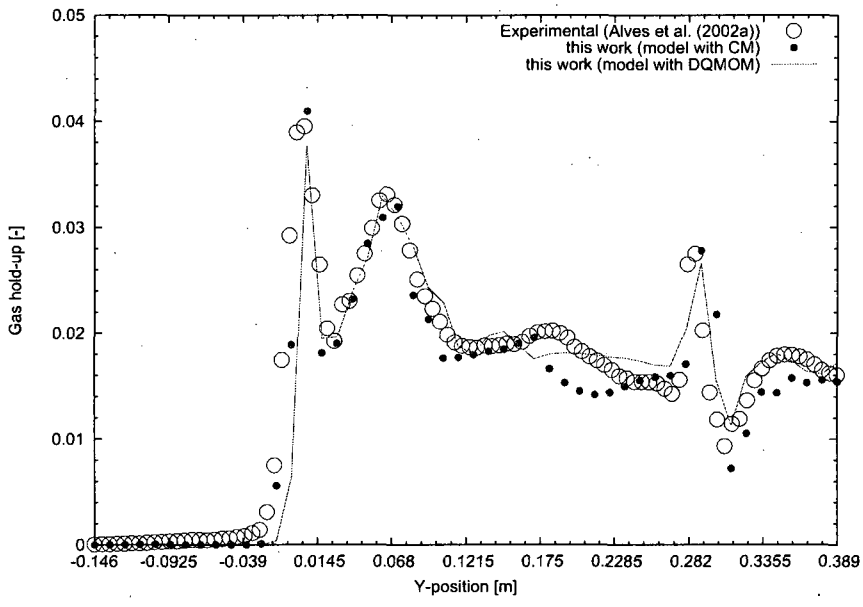

Figure 7.47: Predicted gas hold-up using DQMOM and CM ($r = 7.7\ cm$).

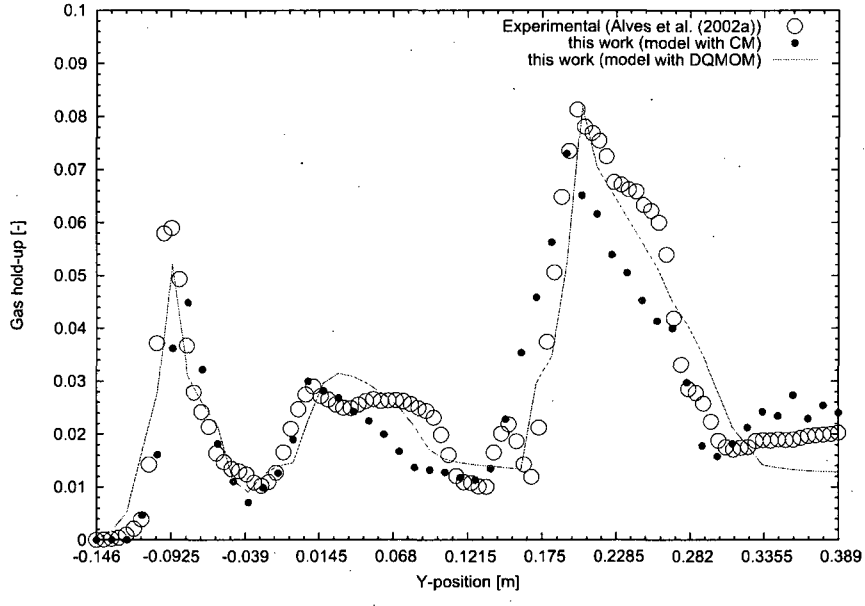

Figure 7.48: Predicted gas hold-up using DQMOM and CM ($r = 13.1\ cm$).

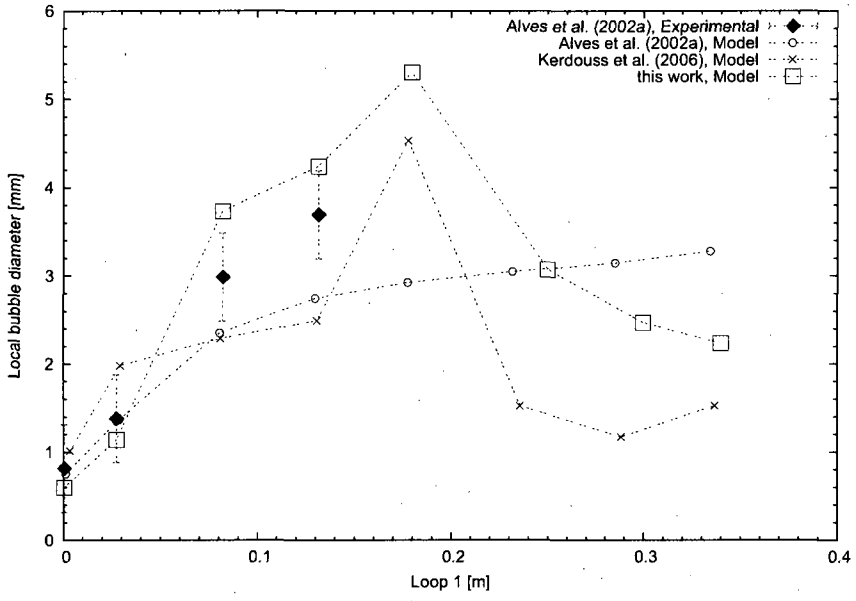

Figure 7.49: Predicted bubble diameter using DQMOM as a function of position along liquid circulation loop 1

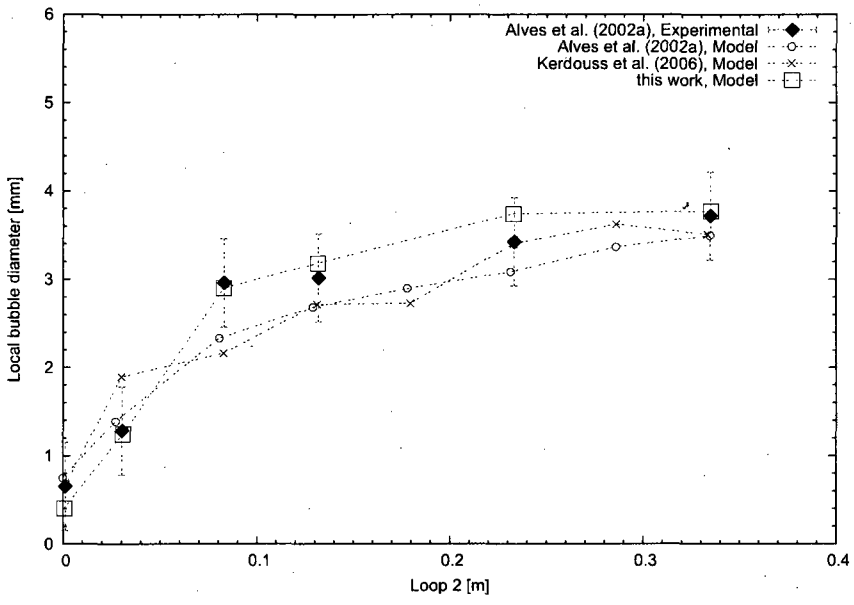

Figure 7.50: Predicted bubble diameter using DQMOM as a function of position along liquid circulation loop 2

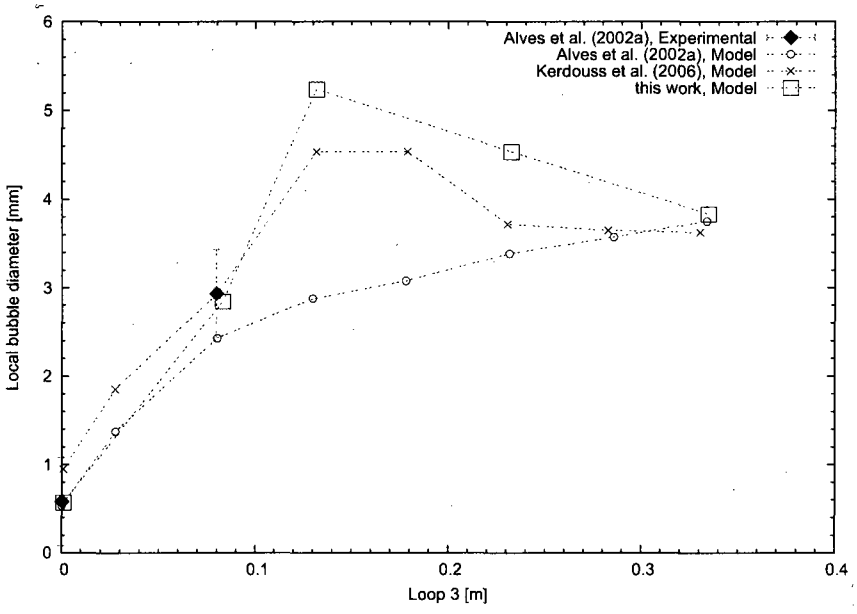

Figure 7.51: Predicted bubble diameter using DQMOM as a function of position along liquid circulation loop 3

Discussion

In the case of the aerated stirred tank reactor with a double turbine, the DQMOM gives again good results when compared to the experimental data and models published by [127; 44]. For quantitative comparison the Sauter mean diameter is chosen for its wide application for determining the mass transfer coefficient. Different loops are used to compare the present model with available measurements from the literature, agreement is again good.

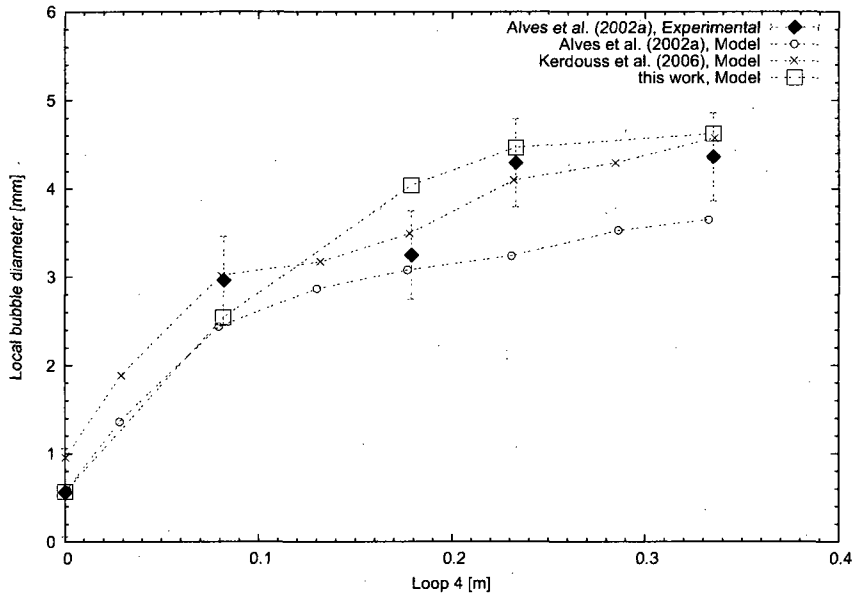

Figure 7.52: Predicted bubble diameter using DQMOM as a function of position along liquid circulation loop 4

7.3.3 Test case C: Air-lift bioreactor

Air-lift reactors are attractive for slow reactions since they consist of recycle streams that allow for larger residence time within a small reactor volume when compared to bubble columns. They are also attractive in processes where a certain degree of agitation is required with the use of mechanical stirrers due to the nature of reactants handled, such as the culture of biological organisms and wastewater treatment. In this work, investigations of hydrodynamic properties such as the gas holdup, liquid velocity, mass transfer coefficient and bubble size distribution, are outlined. The basic philosophy behind our investigation resides in understanding the influence of bubble size distribution on the hydrodynamics and mass transfer characteristics of air-lift reactors.

Experimental Set-up

An airlift reactor (35L capacity) is shown in Fig. 7.53. It is made of an inner cylinder with (63.11 $cm \times 11$ cm) ($H \times D$). The inner cylinder is positioned at 5.23 cm from the bottom and an external cylinder of (101.85 $cm \times 17.67$ cm) ($H \times D$).

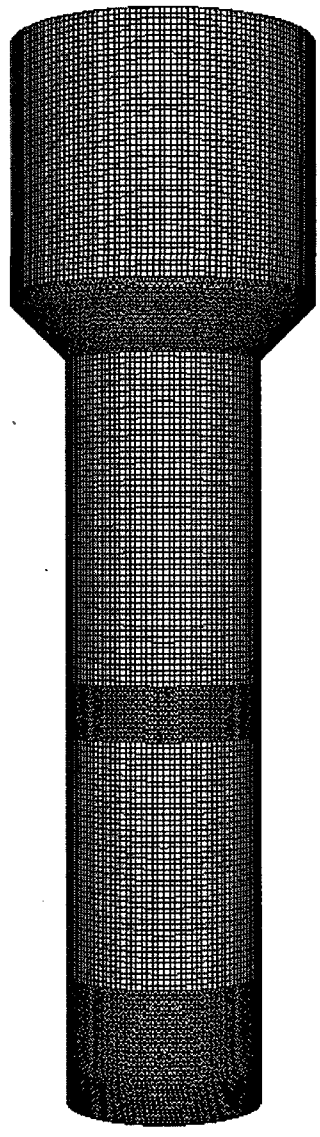

Figure 7.53: Airlift reactor structured mesh grid

In order to ensure a high mass transfer rate into the medium, Fisher brand gas diffusing stones (spherical and porous) were added to make the air inlet more diffuse and more uniformly distributed. It contains an average pore size $60\mu m$ and particle retention $25\mu m$. The three spherical porous gas diffusion pellets and the injection of the air is as shown in the Fig. 7.54.

Reactor modelling

To predict the volumetric mass transfer coefficient, $\mathbf{k_La}$, the model developped in this thesis is used. It has been in the previous sections tested on bubble column and a double-turbine stirred reactor and validated with the available experimental data from the scientific literature. In the present case, calculations are carried out for the geometry presented above with initial liquid volume of 21 L. The flow rate is set to 8 L/min with the same transport properties of fluids as used in this study (see Table 7.5). Preliminary tests on grid convergence (space and time accuracy) were made to ensure that the number of cells used is sufficient for numerical convergence and accuracy but are not presented in the following.

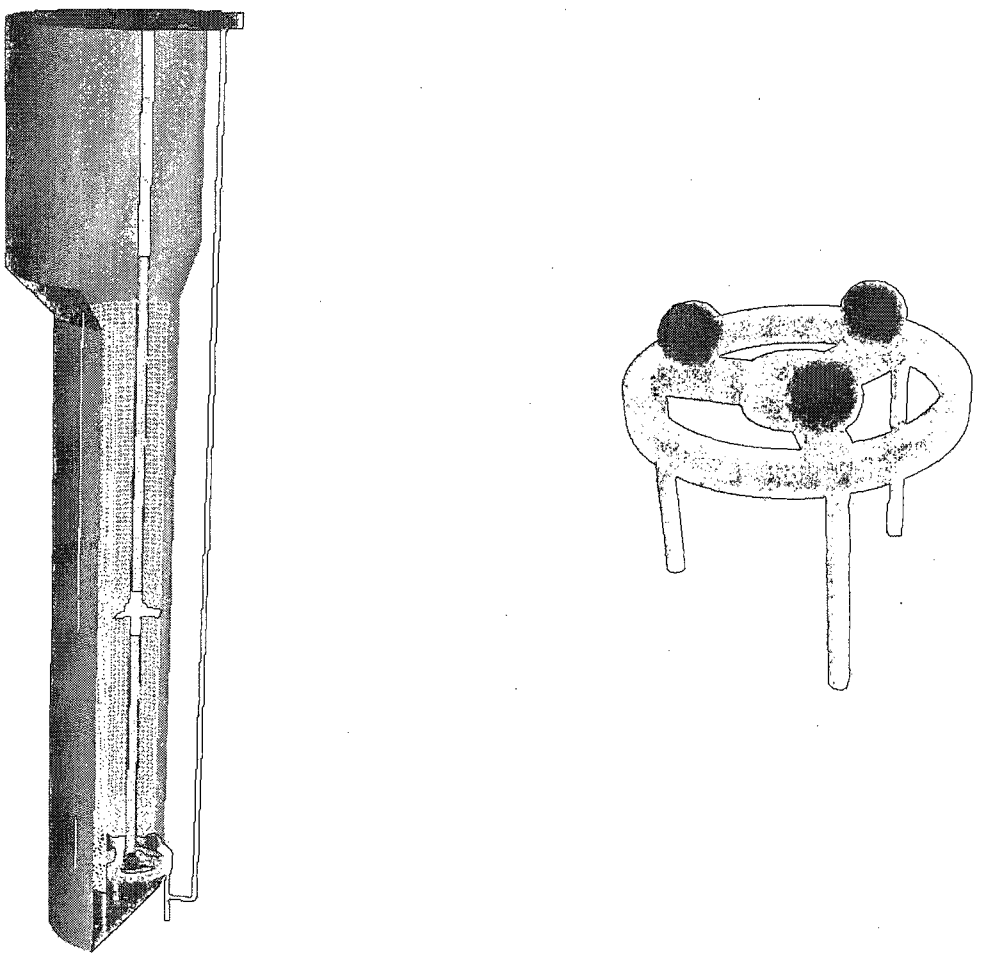

Figure 7.54: Geometry used in the present model. Airlift bioreactor (left) and gas diffusing of Fisher brand (right).

Table 7.6: Informations about grid mesh

Total number of cells	hex.	tet.	pyr.	$V_{reactor}$ (model)	$V_{reactor}$ (Exp.)	mesh quality
509978	227445	275944	6589	34.61L	35L	99.98%

Where $V_{reactor}$ represent the total volume of airlift reactor.

The population balance equation is solved by using the method of classes (11 classes) and DQMOM with three nodes ($N = 3$) in which the source terms are the result of the interactions between bubbles-bubbles and bubbles-liquid due to the turbulence intensity. All walls are treated as non slip boundaries using standard wall function as described before for the turbulence model. The gas flow rate at the sparger is defined as inlet velocity of type boundary condition with the gas volume fraction equal to unity. The initial bubbles size at the inlet is set to fixed value of 1 mm.

Results and discussion

The Multiple Rotating Frame (MRF) technique is used to represent the rotating movement of impeller as used in the test case B. The Population Balance Equation (PBE) is used in order to describe and follow the fluid dynamics and bubbles interactions in time and space. PBE is solved using two approximate methods known as the Direct Quadrature Method Of Moments (DQMOM) and the Method of Classes (CM) where the continuous distribution of bubble sizes is approximated through a discrete number of size, with the exchange between different classes with coalescence and break-up phenomena. In this test case (C), the predicted results are obtained with model using the DQMOM and CM with 11 classes. Figure 7.55 show the predicted results of Sauter mean diameter and mass transfer coefficient ($\mathbf{k_L a}$) through three different positions.

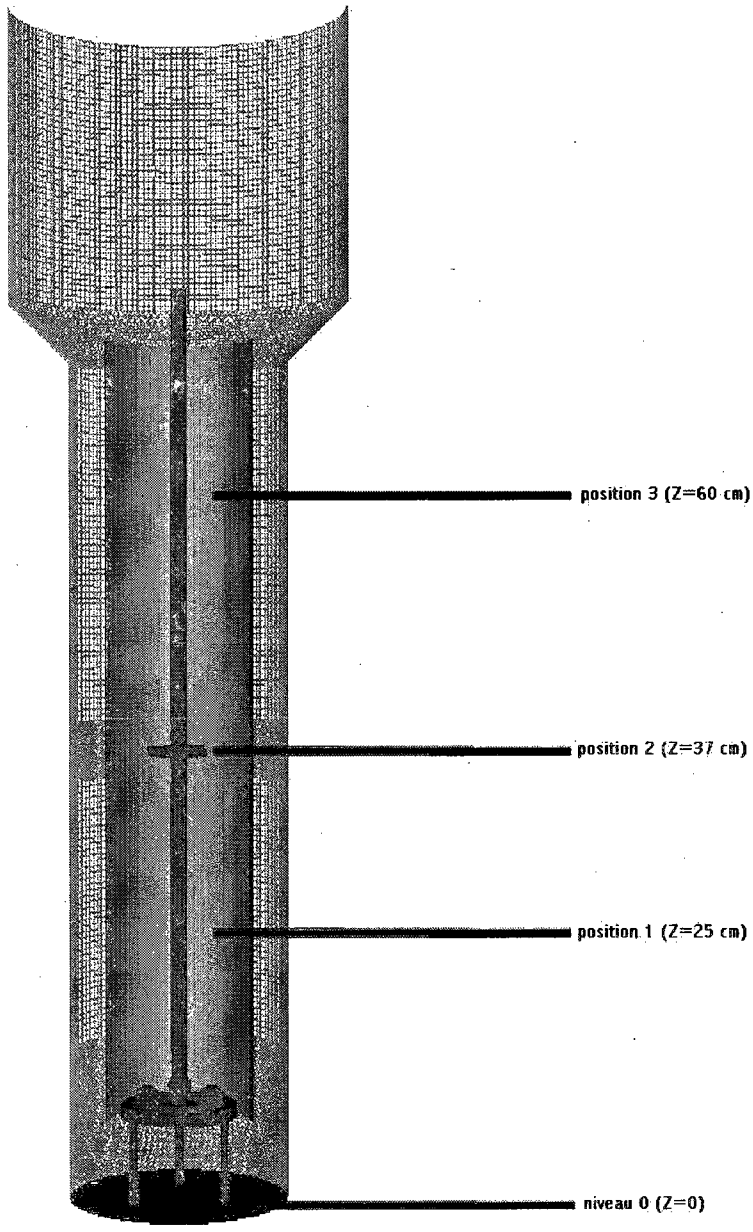

Figure 7.55: Identification of different positions used in airlift bioreactor

In this study, Higbie's penetration model (Higbie, 1935) is used to calculate the gas-liquid mass transfer coefficient $\mathbf{k_L a}$. This model is widely used by several authors and it is valid for a large turbulence range:

$$\mathbf{k_L a} = \frac{2}{\sqrt{\pi}} \sqrt{\mathbf{D}_{O_2}} \left(\frac{\epsilon \rho_c}{\mu_c} \right)^{1/4} \mathbf{a} \tag{7.12}$$

Where $\mathbf{a}$ is the interfacial area calculated as:

$$\mathbf{a} = 6\alpha_d / d_{32} \tag{7.13}$$

Here, $\mathbf{D}_{O_2}$ is the diffusion coefficient of oxygen in water set to 2.05×10^{-9} m^2/s ($P = 1bar$ and $T = 25^oC$) from the experimental conditions.

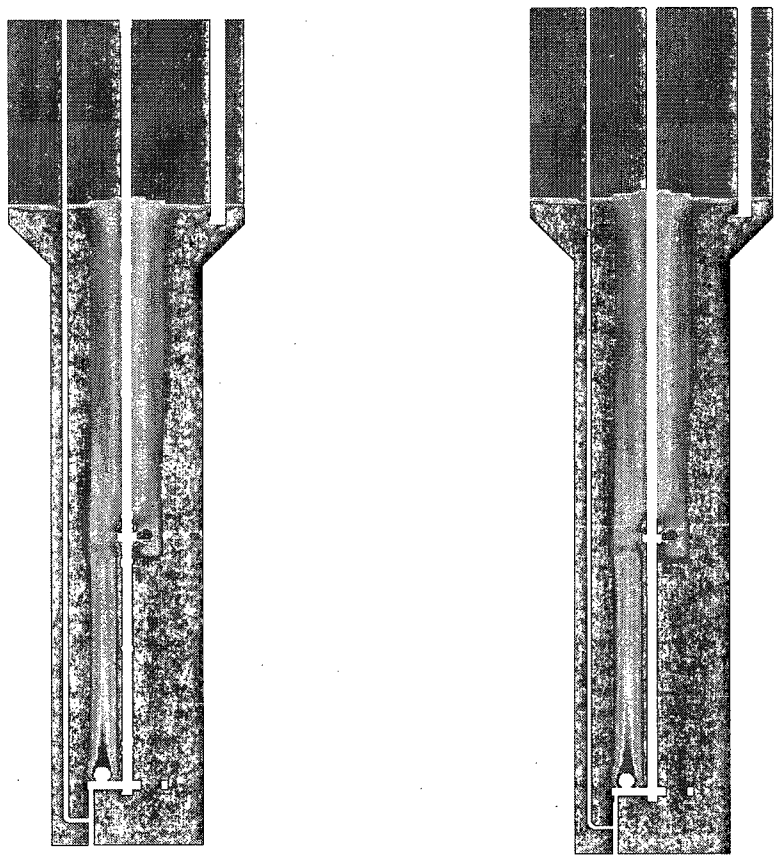

Figure 7.56: Contour of gas hold-up using CM (left) and DQMOM (right).

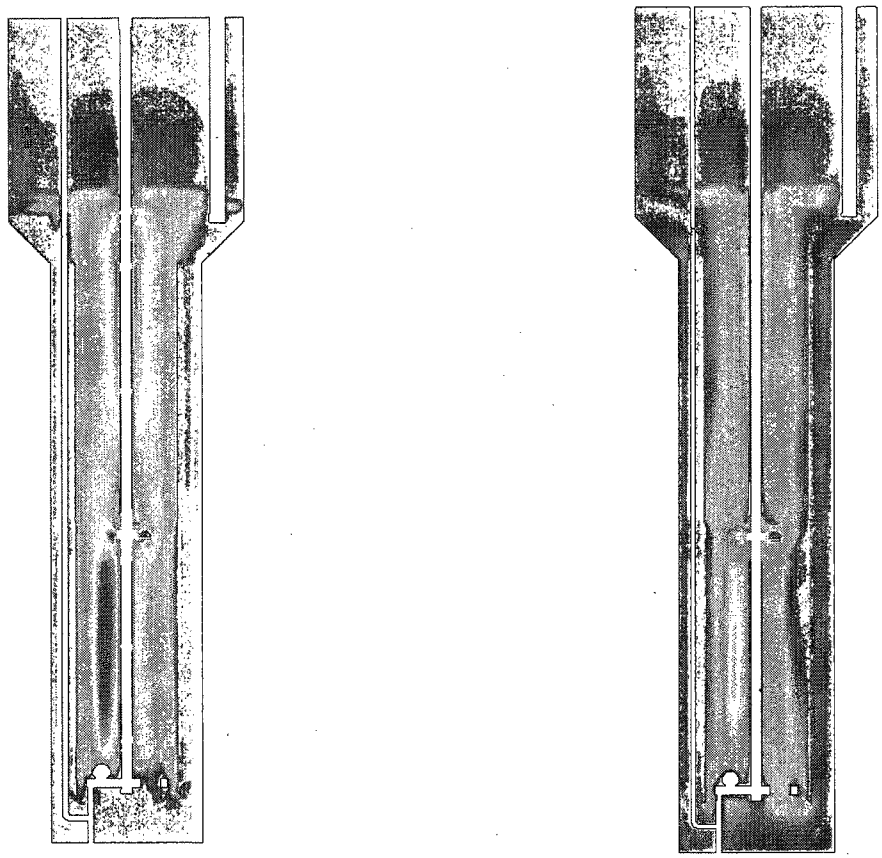

Figure 7.57: Gas velocity profiles using CM (left) and DQMOM (right).

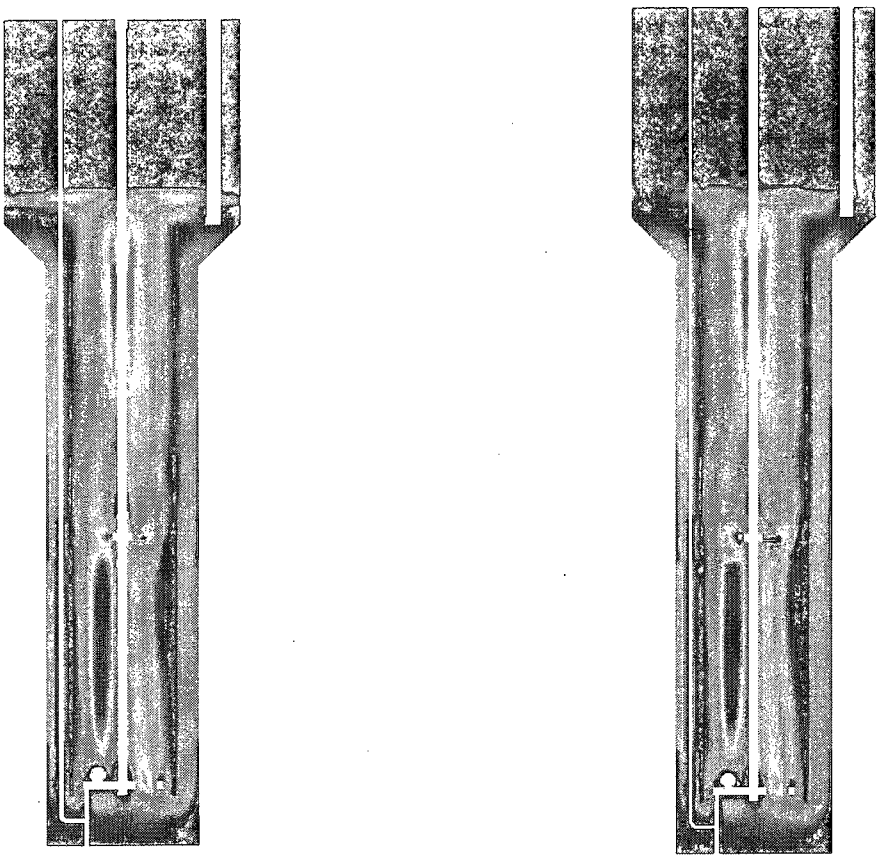

Figure 7.58: Liquid velocity profiles using CM (left) and DQMOM (right).

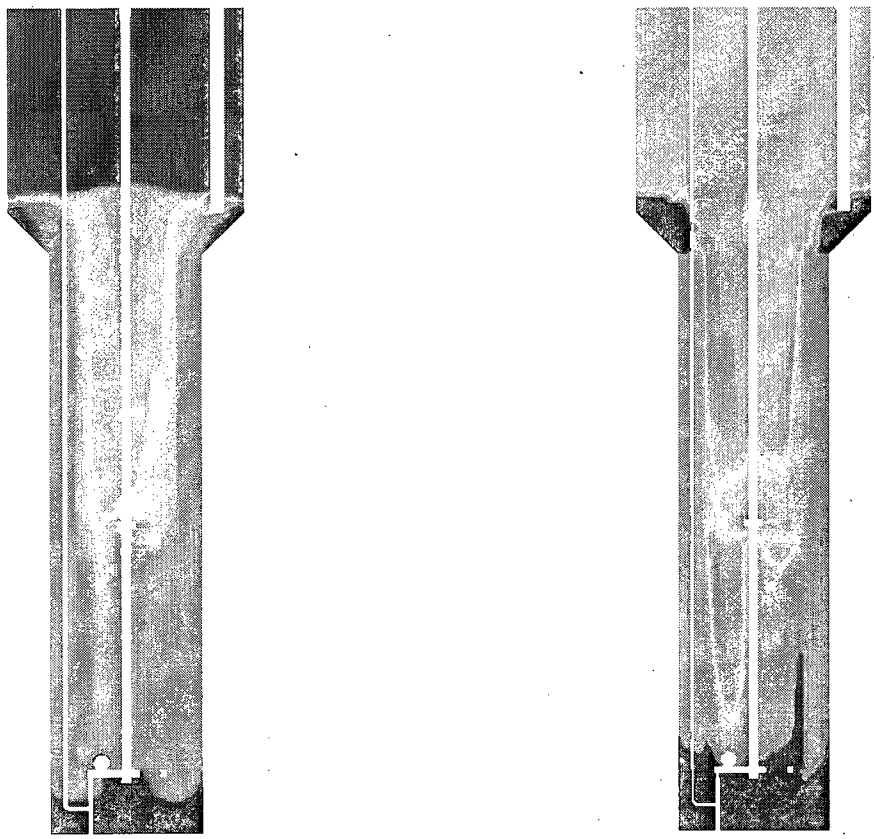

Figure 7.59: Contour of Sauter mean diameter d_{32} using CM (left) and DQMOM (right).

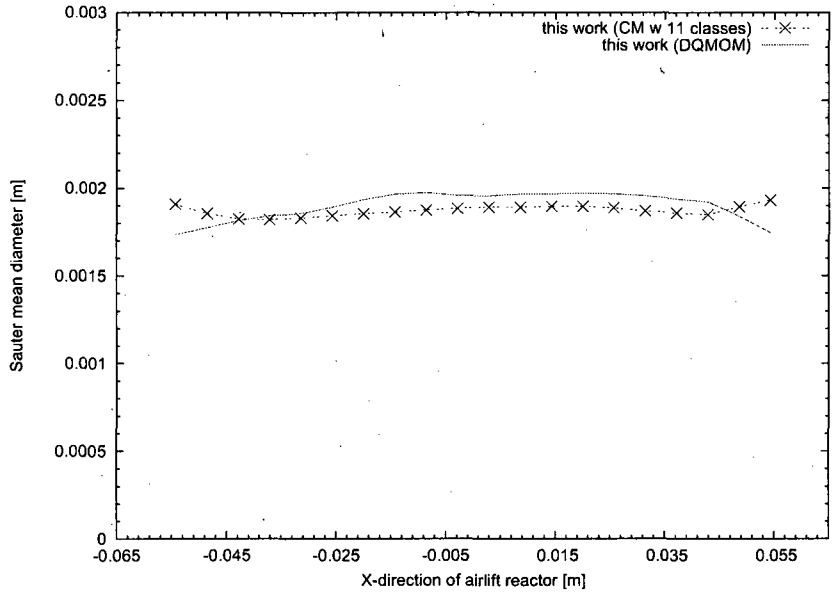

Figure 7.60: Predicted Sauter mean diameter using **DQMOM** and **CM** as a function of X-position (position 1).

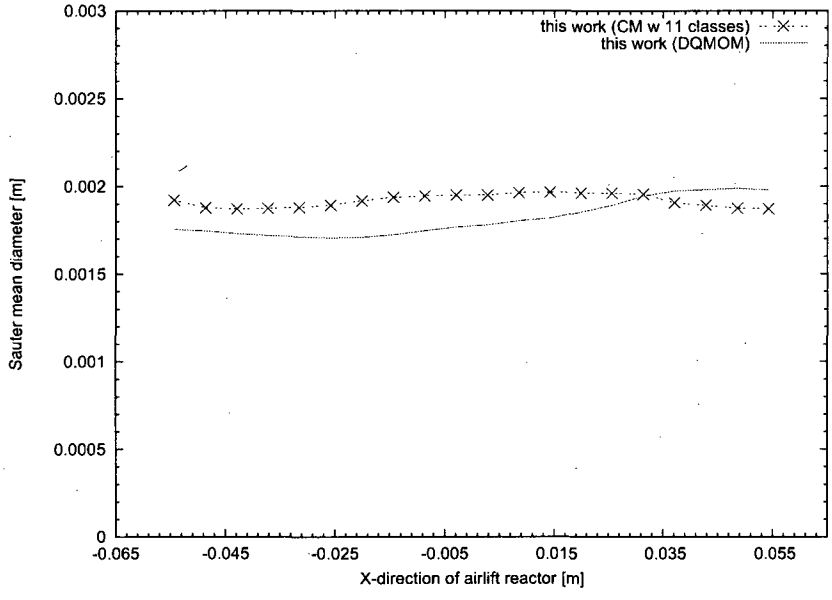

Figure 7.61: Predicted Sauter mean diameter using **DQMOM** and **CM** as a function of X-position (position 2).

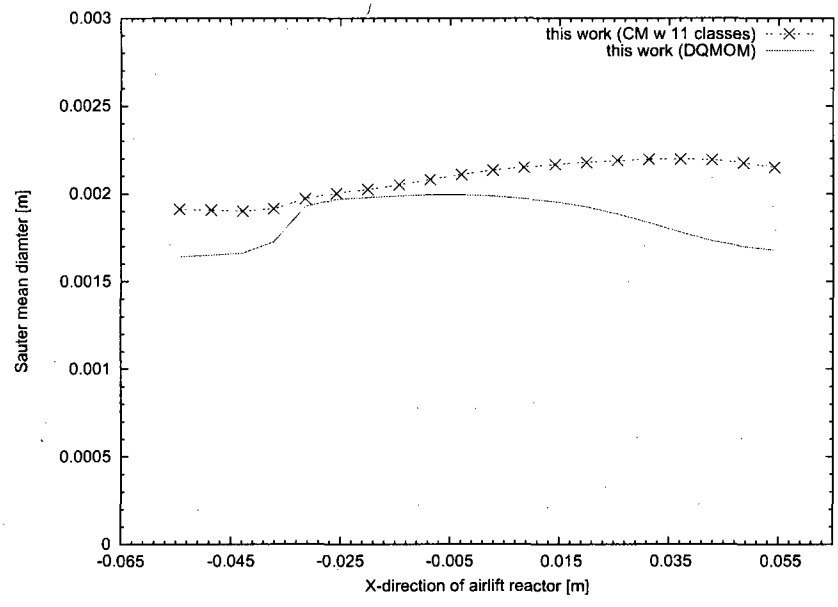

Figure 7.62: Predicted Sauter mean diameter using **DQMOM** and **CM** as a function of X-position (position 3).

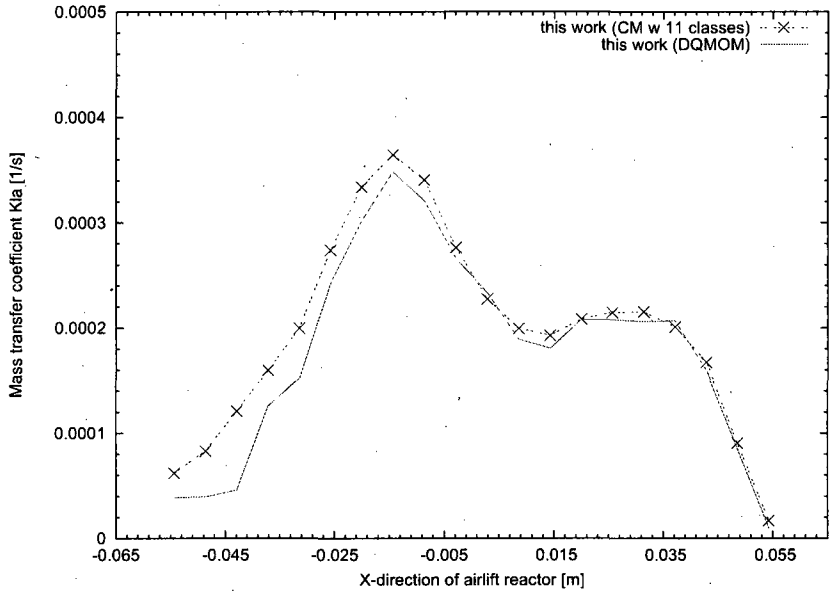

Figure 7.63: Predicted mass transfer coefficient $\mathbf{k_L a}$ using **DQMOM** and **CM** as a function of X-position (position 1).

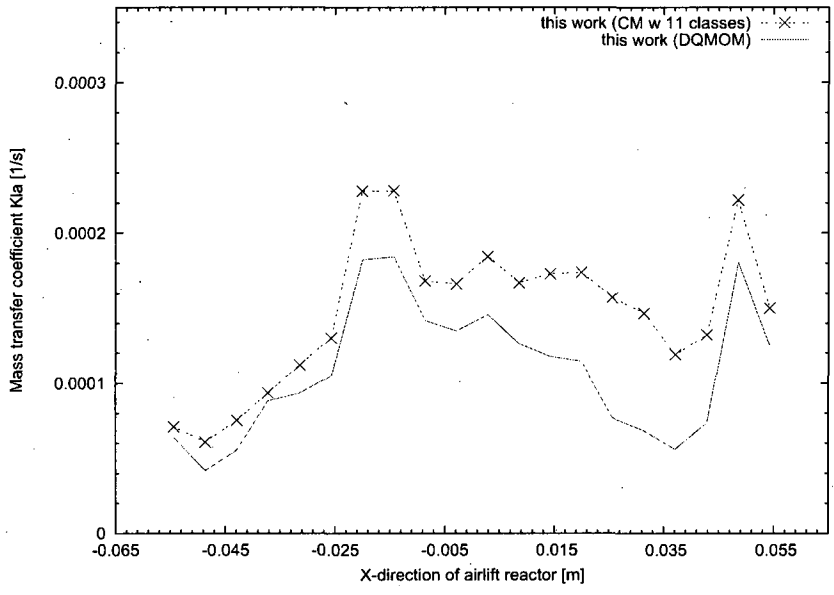

Figure 7.64: Predicted mass transfer coefficient $\mathbf{k_L a}$ using **DQMOM** and **CM** as a function of X-position (position 2).

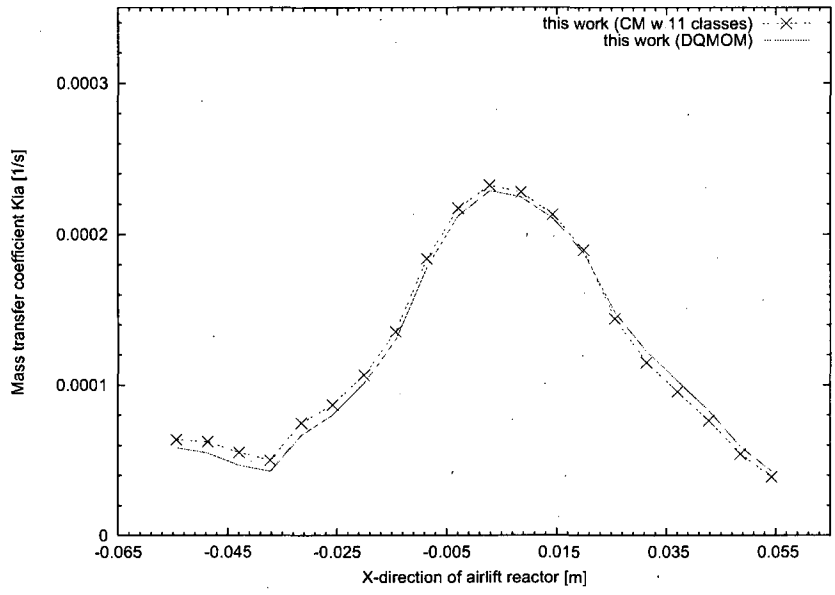

Figure 7.65: Predicted mass transfer coefficient $\mathbf{k_L a}$ using **DQMOM** and **CM** as a function of X-position (position 3).

7.4 Closure

The integration of the PBE and solving it by DQMOM have proved to be accurate while the computational requirement is only a small fraction of the effort needed to solve using the CM. Further experimental measurements in such complex geometries as the airlift bioreactor would clearly help in the validation of the model but using these preliminary results and the comparison with the CM have shown to be very promising. The DQMOM method could be used to obtain a better description of the flow in complex bubbly flows and thus to help design better reactors.

A numerical investigation is made in order to compare the claculation time requirement between DQMOM and CM for the three cases above (A, B and C). The results are shown

in figures (7.66, 7.67 and 7.68). The calculation is caried out using 18 parallel processors of the RQCHP[1] center.

[1] see https://rqchp.ca

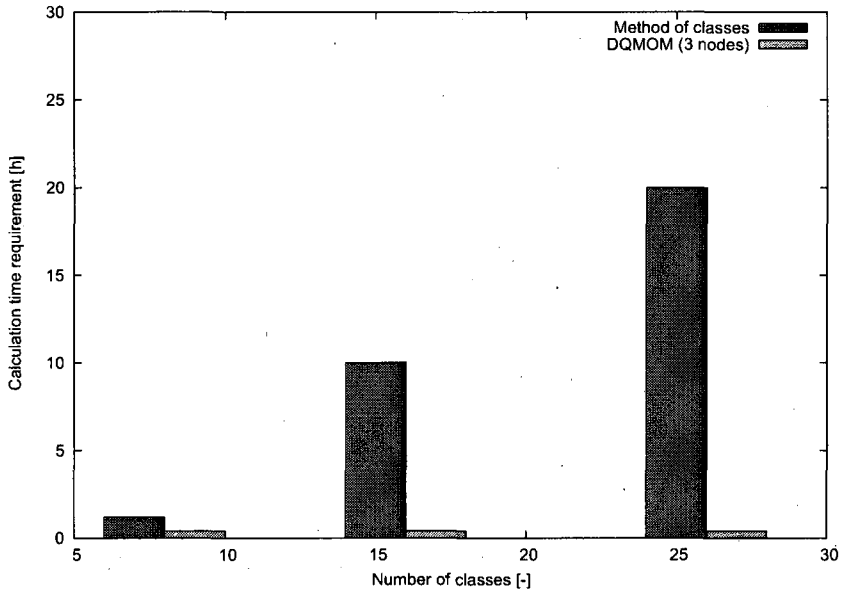

Figure 7.66: Computational time requirement comparison between **DQMOM** and **CM** (case of bubble column with coarse grid).

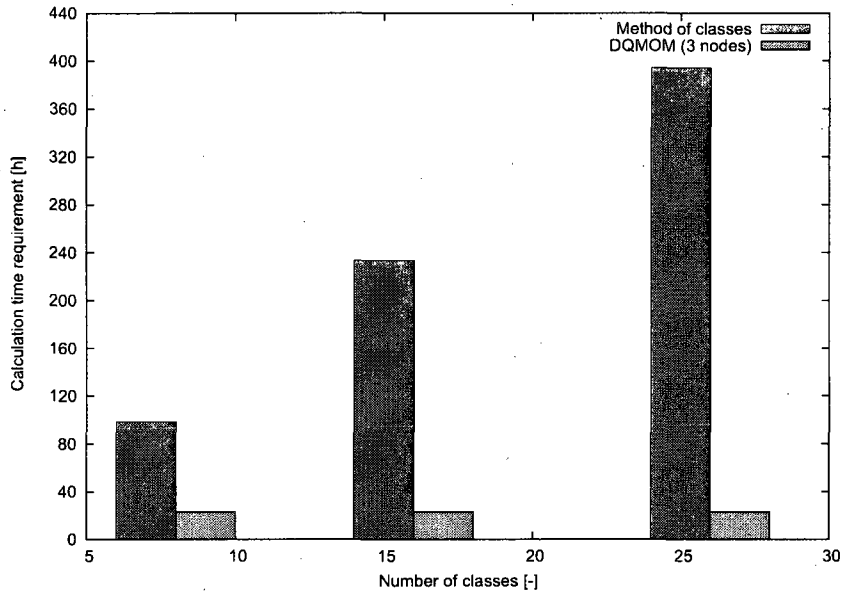

Figure 7.67: Computational time requirement comparison between DQMOM and CM (case of stirred-tank reactor).

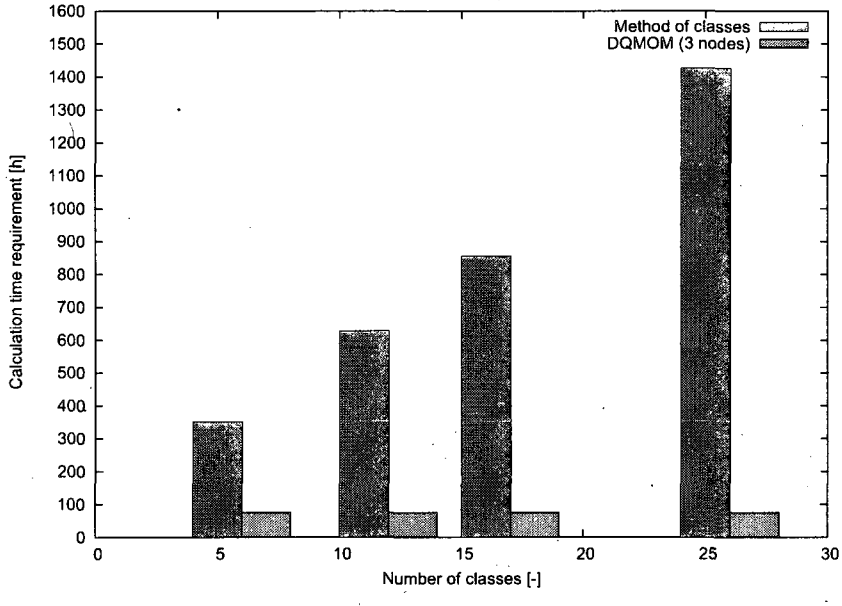

Figure 7.68: Computational time requirement comparison between DQMOM and CM (case of airlift reactor).

Chapter 8

Summary and conclusion

This research work has been concerned with the development and validation of mathematical model using CFD techniques for simulating dispersed two-phase flows at high phase fractions and high turbulence. In this study, two-fluid turbulence model have been extended from the standard $k-\epsilon$ model of Launder et al. [9]. The developed model was validated and utilized for bubbly flow applications.

This last chapter concludes the thesis and is divided in two sections. The first section summarizes the conclusions already made along this thesis and the second one makes suggestions for future work.

8.1 Conclusion

The results of the present study have been extensively assessed and discussed in the previous Chapters. In the following, the most important conclusions are summarized.

- The validity of the proposed model for turbulence was demonstrated. Better predictions for

the phase fraction and liquid velocity profiles in bubbly flows were obtained by comparison with existing two-phase turbulence models. In particular, the influence of the dispersed phase and the gas-liquid interfaces were considered in the proposed model.

• Numerical investigations of bubbly flows in a rectangular bubble column, double-stirred reactor and airlift reactor have shown that the proposed two-phase flow model including the full integration of source terms for multiphase flow was adequate for the prediction of the flow fields variables such as volume fractions and velocity profiles. Drift velocity and bubble induced turbulence are included in the extended model of turbulence. The integration of population balance equation in the model was successful.

• The lift models of Tomiyama identified in the literature yields better results for the bubbly flow than those obtained with conventional lift models. In particular, the magnitudes of the local volume fraction profiles are reduced noticeably.

• Drag correlations of Tomiyama was applied to large bubbles as used in this study at high phase fractions, it agrees with the experimental data reasonably well. However, the predicted results reveal that no great influence of virtual mass coefficient appears to exist on the hydrodynamic behavior in bubbly flows.

• A new numerical technique applicable for solving population balance equation is utilized to describe bubble size distribution under the effects of coalescence and break-up phenomena. The solution of the population balance equation by the DQMOM gives good results when compared to the experimental data and numerical models published in the literature. For quantitative comparisons, the Sauter mean diameter d_{32} is chosen for its wide application in chemical engineering industries (ex. calculation of mass transfer coefficient and drag force), the results are very much satisfactory again.

• Drastic reduction in computational time requirements is obtained when using the new

technique of DQMOM compared to the method of classes, while maintaining a very good accuracy when compared with existing models or available data. Much remains to be done in terms of validation but it clearly appears to be a very promising avenue.

8.2 Future works

Before we proceed with recommendations for the future work, the important role of measurements has to be emphasized. Many sub-models in the two-fluid model rely on the availability and accuracy of measurements. Therefore, only more extensive experimental data will reduce the uncertainty inherent in some of the models and/or will give evidence of phenomena currently unaccounted for. The author is not an expert in the experimental methods. Therefore, the suggestions which follow will be mainly directed towards researchers in the field of modelling and numerical methods:

- Validation of the current two-fluid model against a more complete set of experimental data. Several test cases were presented in this thesis (bubble column, double-turbine stirred reactor and air-lift reactor). Of the cases listed there, the following ones could yield new insights:

  - In the reactor with high turbulence (agitation), regions of high shear within the liquid phase are problematic for accurate prediction of bubble distribution.

  - Bubble-induced turbulence and large scale instabilities cause additional difficulties [43; 29], and must be studied in depth.

- Derivation of accurate and reliable correlations for the population balance equation taking in account more reliable models of coalescence and breakage. In particular, for bubbles, the effects of concentration, turbulence and the history of the bubble formation should be taken

into account in the correlations.

As it becomes more and more validated, the model can be used for several industrial applications such as polymersation, heat and mass transfer in chemical reactors, plasma, metallurgy (ex. purification of liquid aluminum), environment, pollution, aerosol.

The present study should be regarded as another step towards the accurate simulation of dispersed two-phase flows. The two-fluid model presented in here has addressed many important phenomena, such as turbulence, mass transfer coefficient, particles size distribution effects as well as grid mesh dependence. The inclusion of these into the framework of the two-fluid model is by no means uncharted territory and many researchers have made significant contributions towards it. However, it is unlikely that a single model will emerge eventually because of the many ways these phenomena interact with each other. More likely, several two-fluid models will co-exist, each specializing in the aspects most relevant to the particular industrial application in mind. In this respect, it is the hope of the author that this study might serve as a toolbox to other modelers and engineers in industry who attempt the prediction of two-phase flows with good accuracy.

Chapter 9

Sommaire et conclusion

Ce travail de recherche a été décernés au développement et la validation d'un modèle mathématique utilisant des techniques de la mécanique des fluides computationelle 'CFD' pour simuler les écoulements diphasiques dispersés à une grande fraction volumique et avec présence de la turbulence. Dans cette étude, le modèle standard de turbulence à deux équations $k - \epsilon$ issu des travaux de Launder et al. [9] à été modifié. Le modèle développé à été testé et validé pour des écoulements dispersés bulle-liquide.

Ce dernier chapitre conclut la thèse et il est divisé en deux sections. La première section résume les conclusions déjà entamées tout au long de la thèse, et la seconde est consacrée à des suggestions pour les travaux futurs.

9.1 Conclusion

Les résultats de la présente étude ont été largement évalués et discutés dans les chapitres précédents. Par conséquent, les conclusions les plus importantes sont résumées dans ce chapitre.

• La validité du modèle proposé pour la turbulence a été démontrée. De meilleures prévisions pour la fraction volumique de la phase dispersée et les profils de vitesse des liquides ont été obtenues en comparaison avec des résultats obtenus par les modèles de turbulence existants. En particulier, l'influence de la phase dispersée et l'interfaces gaz-liquide sur l'écoulement qui ont été pris en compte dans le modèle proposé.

• Des investigations numériques sur l'écoulement de bulles dans une colonne à bulle, réacteur agité et bioréacteur airlift ont montré que le modèle proposé à deux phases en incluant des termes sources, pour tenir en compte l'influence de la phase dispersée et l'interface gaz-liquide sur les écoulements complexes, était adéquat concernant la prédiction de certaines variables tels que les fractions volumiques et les profils de vitesse. La vitesse de dérive et la rotation des bulles due à la turbulence sont inclus dans le modèle développé. L'implémentation de l'équation du bilan de population dans le modèle a été l'objet principal de cette thèse.

• Le modèle de Tomiyama pour le coefficient de soulèvement 'lift' tiré de la littérature donne de meilleurs résultats pour les écoulements à bulles que celles obtenues avec des modèles classiques. En particulier, les profils de la fraction volumique des bulles sont sensiblement réduits.

• La corrélations de Tomiyama pour la force de traînée a été appliquée pour les grosses bulles. Les résultats du modèle sont en accord avec les données expérimentales. Toutefois, les résultats prédit par le modèle révèlent que une grande influence de la masse virtuelle coefficient semble exister sur le comportement hydrodynamique de l'écoulement des bulles.

• Une nouvelle méthode numérique pour résoudre l'équation du bilan de population est utilisée pour décrire la distribution de taille des bulles sous l'effet des phénomènes de coalescence et de fragmentation. La solution de l'équation du bilan de population par la DQMOM donne de bons résultats lorsqu'on les comparent aux données expérimentales et à d'autres modèles

numériques publiés dans la littérature. Pour faire des comparaisons quantitatives, le diamètre moyen de Sauter $d_{(32)}$ est choisi pour ses nombreuses applications dans les industries de génie chimique (ex. calcul du coefficient de transfert de masse et de force de traînée). À nouveau les résultats sont très satisfaisants.

• Une réduction considérable en temps de calcul est obtenue en utilisant la nouvelle technique de DQMOM par rapport à la méthode des classes, tout en maintenant une très bonne précision en comparaison avec les modèles existants ou des données exérimentales disponibles dans la litérature. Malgré ces résultats, Il reste beaucoup à faire en termes de validation de cette méthode sur d'autres applications industrielles, mais il semble clairement être une voie de recherche très prometteuse.

9.2 Travaux futurs

Avant de procéder à des recommandations pour les travaux futurs, le rôle important des mesures expérimentales doit être souligné. De nombreux modèles numériques ont été développé sur la base de la disponibilité et la précision des mesures. Par conséquent, seulement un plus grand nombre de données expérimentales permettront de réduire l'incertitude inhérente à certains de ces modèles numériques. L'auteur de cette thèse n'est pas un expert dans l'expérimentation et par la suite les suggestions suivantes seront principalement résumées pour les chercheurs dans le domaine de la modélisation numérique et la mécanique des fluides computationelle CFD:

• Validation de l'actuel modèle pour un ensemble complet de données expérimentales. Plusieurs cas de test ont été présentés dans cette thèse (colonne à bulles, réacteur agité à double turbine et bioréacteur airlift). Parmi les cas qui y sont énumérés, les cas suivants pourraient donner de nouvelles indications:

•• Dans le réacteur agité à forte turbulence, les régions qui présentent un cisaillement élevé au sein de la phase liquide sont problématiques pour la prévision précise de la distribution des bulles.

•• La turbulence induite par la rotation des bulles et quelques instabilités à grande échelle entraîne des difficultés supplémentaires [43; 29], et doivent être étudiés en profondeur.

• Développement de nouvelles corrélations précises et fiables pour l'équation du bilan de population est prise en compte dans cette étude ainsi des modèles modèrnes de coalescence et fractionnement des bulles sont implémentés dans ce modèle mathématique. En particulier, pour les bulles, les effets de la concentration, la turbulence et l'histoire de la formation des bulles doivent être pris en compte dans le futur.

Le modèle peut être utilisé pour plusieurs applications industrielles telles que la polymérisation, le transfert de chaleur et de masse dans les réacteurs chimiques, plasma, la métallurgie (ex. purification de l'aluminium liquide), environnement, pollution et les aérosoles.

La présente étude doit être considérée comme un nouveau pas vers une simulation numérique précise des écoulements dispersés. Le modèle à deux phases présenté ici a abordé de nombreux phénomènes importants, comme la turbulence, le coefficient de transfert de masse, la distribution des tailles de particules ainsi que la dépendance du maillage. L'inclusion de tous ces paramètres dans le modèle est loin d'être un domaine inconnu et de nombreux chercheurs ont apporté des contributions significatives. Toutefois, il est peu probable qu'un modèle unique finira par être le meilleur en raison de nombreuses façons de programmation et que la plupart des phénomènes interagissent les uns avec les autres. À cet égard, l'espoir de l'auteur est que le modèle développé sera utilisé comme une référence à d'autres chercheurs du CFD.

Appendix A

Product Difference Algorithm

The PD algorithm proceeds in a sequence of steps biginning with setting up a triangular array of elements P(i,j). Elements of the first column are :

$$P(i,1) = \delta_{i,1} \tag{A.1}$$

where $\delta_{i,1} = 0$ for $i \neq 1$ and $\delta_{i,1} = 1$ for $i = 1$. The second column contains the moments with alternating sign:

$$P(i,2) = (-1)^{i-1} m(i-1) \tag{A.2}$$

The rest of elements of matrix P(i,j) are obtained from :

$$P(i,j) = P(1,j-1)P(i+1,j-2) - P(1,j-2)P(i+1,j-1) \tag{A.3}$$

The coefficients of the continued fraction (α_i) are generated by setting the first element equal to zero and computing the others according to the following relationship :

$$\alpha_i = \frac{P(1,i+1)}{P(1,i)P(1,i-1)}; \qquad i \in 2,...,2N \tag{A.4}$$

A symmetric tridiagonal matrix is obtained from sums and products of α_i,

$$a_i = \alpha_{2i} + \alpha_{2i-1}; \qquad i \in 1,...,2N-1 \tag{A.5}$$

and

$$b_i = \sqrt{(\alpha_{2i+1}\alpha_{2i-1})}; \qquad i \in 1, ..., 2N-2 \tag{A.6}$$

where a_i and b_i are the diagonal and the codiagonal of Jacobi matrix respectively. When the tridiagonal matrix is determined, generation of the weights and abscissas is done by finding its eigenvalues and eigenvectors. In fact, the eigenvalue are the abscissas and the sqare of the first component of the jth eigenvectors v_j are the weights ($L[i] = d[i]$, $w[i] = m_0(v[i][1])^2$). Here, $d[i]$ and $v[i][j]$ are the obtained eigenvalues and eigenvectors from Jacobi matrix available in the code OpenFOAM.

A.1 Linear System solution

The solution of the linear system generated by the Eqn.(??) is obtained using Gauss-Seidel method implemented in the present work as follow:

- construct a symmetric matrix $A[i][j]$, $i = 0, ..., 2N-1$, $j = 0, ..., 2N-1$, where N is the node of the quadrature approximation used in DQMOM.
- filling the matrix $A[i][j]$ with coefficients obtaining by developing the Eqn.(??).
- Solve the formed linear system using Gauss-Seidel method. As default, the Gauss-Seidel method is not our subject in the present study.

A.2 Example of initial distribution of moments

By definition the moments distribution is given by:

$$m^{(k)}(t) \approx \sum_{i=1}^{n} L_i(t)^k w_i(t) \tag{A.7}$$

Table A.1 shows the results of intial distribution of moments. As verified, the moments (column 2) are recovered upon substitution of the abscissas (column 5) and weights (column

Table A.1: Initial distribution of first order of moments

k	$m^k(t=0)$	a_k	b_k	$L^{(k)}$	$w^{(k)}$
0	1.0				
1	5.0	5.0	2.88675	15.2853	0.0283736
2	33.3333	8.33343	4.7139	7.18626	0.452838
3	277.778	11.6673	0.0	2.52914	0.518788
4	2777.78				
5	32407.4				

6) into Eqn.(A.7). Columns 3 and 4 from the table A.1 contain a_k and b_k (positive root of b_k^2) calculated using the Product-Algorithm described in this appendix. Here, k represent the first order of moments ($k = 5$ in this study).

Appendix A

OpenFOAM CFD tools

A.1 Introduction

Open**FOAM** **F**ield **O**peration **A**nd **M**anipulation is first and foremost a C++ library, used primarily to create executables, known as applications. The applications fall into two categories: solvers, that are each designed to solve a specific problem in continuum mechanics; and tutorials, that are designed to perform tasks that involve cases applications. The OpenFOAM distribution contains numerous solvers and tutorials covering a wide range of problems encountered in chemical industries.

One of the strengths of OpenFOAM is that new solvers and utilities can be created by its users with some pre-requisite knowledge of the underlying method, physics and programming techniques involved.

OpenFOAM is supplied with pre- and post-processing environments. The interface to the pre- and post-processing are themselves OpenFOAM utilities, thereby ensuring consistent data handling across all environments. The overall structure of OpenFOAM is shown in

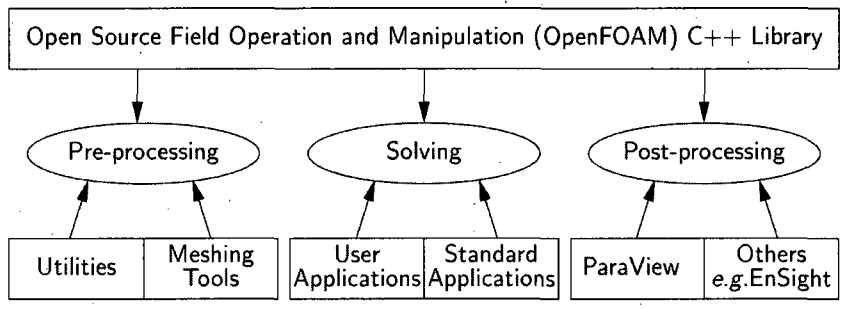

Figure A.1: Overview of OpenFOAM structure

Fig.A.1.

A.2 Application and libraries

In OpenFOAM, applications are split into two main categories:

solvers that are each designed to solve a specific problem in computational fluid dynamics.

tutorials that perform simple pre-and post-processing tasks, mainly involving data manipulation and algebraic calculations.

A.2.1 Object-orientation and C++

Progamming languages that are object-oriented, such as C++, provide the mechanism-classes to declare types and associated operations that are part of the verbal and mathematical languages used in science and engineering. C++ provides the mechanism of *template classes* such that the template class **Field**<**Type**> can represent a field of any <**Type**>, e.g. scalar, vector, tensor. The general features of the template class are passed on to any class created from the template. Templating and inheritance reduce duplication of code and

create class hierarchies that impose an overall structure on the code.

A.2.2 Equation representation

A central theme of the OpenFOAM design is that the solver applications, written using the OpenFOAM classes, have a syntax that closely resembles the partial differential equations being solved. For example the equation

$$\frac{\partial}{\partial t}(\rho \mathbf{U}) + \nabla \cdot (\phi \mathbf{U}) - \nabla \cdot (\mu \nabla \mathbf{U}) = -\nabla p \tag{A.1}$$

is represented by the code

```
solve
(
    fvm::ddt(rho, U)
  + fvm::div(phi, U)
  - fvm::laplacian(mu, U)
    ==
  - fvc::grad(p)
);
```

This and other requirements demand that the principal programming language of OpenFOAM has object-oriented features such as template classes, virtual functions and operator overloading. These features are not available in many languages that purport to be object-orientated but actually have very limited object-orientated capability, such as FORTRAN-90. C++, however, possesses all these features while having the additional advantage that it is widely used with a standard specification so that reliable compilers are available that produce

efficient executables. It is therefore the primary language of OpenFOAM.

A.3 OpenFOAM cases

The tutorial cases that accompany the OpenFOAM distribution provide useful examples of the case directory structures. The tutorials are located in the /OpenFOAM/user/run/tutorials directory, reached quickly by executing the tut alias at the command line. Users can view tutorial examples at the OpenFOAM documentation (see http://www.opencfd.co.uk/openfoam/doc/index.html).

A.3.1 File structure of OpenFOAM cases

constant directory that contains a full description of the case mesh in a subdirectory polyMesh and files specifying physical properties for the application concerned, e.g. *transportProperties*.

system directory containing individual files of data for particular fields. The data can be: either, initial values and boundary conditions that the user must specify to define the problem; or, results written to file by OpenFOAM. Also the user can find several numerical schemes in this directory, i.e. *fvSolution* and *fvScemes*.

A.3.2 Scalars, vectors and tensors notations

A *scalar* is a single number represented as such in a data file. A *vector* is a VectorSpace of rank 1 and dimension 3, and since the number of elements is always fixed to 3, the simple List format is used. Therefore a *vector* (1.0, 1.1, 1.2) is written:

(1.0 1.1 1.2)

In OpenFOAM, a *tensor* is a VectorSpace of rank 2 and dimension 3 and therefore the data entries are always fixed to 9 real numbers. Therefore the identity tensor, described in the Programmer's Guide of OpenFOAM tools, can be written:

```
(
    1 0 0
    0 1 0
    0 0 1
)
```

A.3.3 Dimensional units

In continuum mechanics, properties are represented in some chosen units, e.g. mass in kilograms (kg), volume in cubic metres (m^3), pressure in Pascals ($kgms^{-2}$). Algebraic operations must be performed on these properties using consistent units of measurement; in particular, addition, subtraction and equality are only physically meaningful for properties of the same dimensional units. As a safeguard against implementing a meaningless operation, OpenFOAM attaches dimensions to field data and physical properties and performs dimension checking on any tensor operation.

The Input/Output format for a *dimensionSet* is 7 scalars delimited by square brackets, e.g.

[0 2 -1 0 0 0 0]

where each of the values corresponds to the power of each of the base units of measurement listed in TableA.1. The table gives the base units for the Système International (SI) and the United States Customary System (USCS) but OpenFOAM can be used with any system of

Table A.1: Base units for SI and USCS

No.	Property	SI unit	USCS unit
1	Mass	kilogram (kg)	pound-mass (lbm)
2	Length	metre (m)	foot (ft)
3	Time	second (s)	second (s)
4	Temperature	Kelvin (K)	degree Rankine (^oR)
5	Quantity	kilogram-mole (kgmol)	pound-mole (lbmol)
6	Current	Ampere (A)	Ampere (A)
7	Luminous intensity	candela (cd)	candela (cd)

units. All that is required is that the input data is correct for the chosen set of units.

A.4 Mesh conversion in OpenFOAM

The user can generate meshes using other packages and convert them into the format that OpenFOAM uses. The mesh conversion codes have the naming convention available mesh converters are for example:

fluentMeshToFoam reads a Fluent.msh mesh file, working for both 2-D and 3-D cases;

gambitToFoam reads a GAMBIT.neu neutral file;

cfxToFoam reads a CFX mesh written in .geo format;

A.5 Post-processing

This section describes options for post-processing with OpenFOAM. OpenFOAM is supplied with a post-processing utility paraFoam that uses ParaView which is an open source

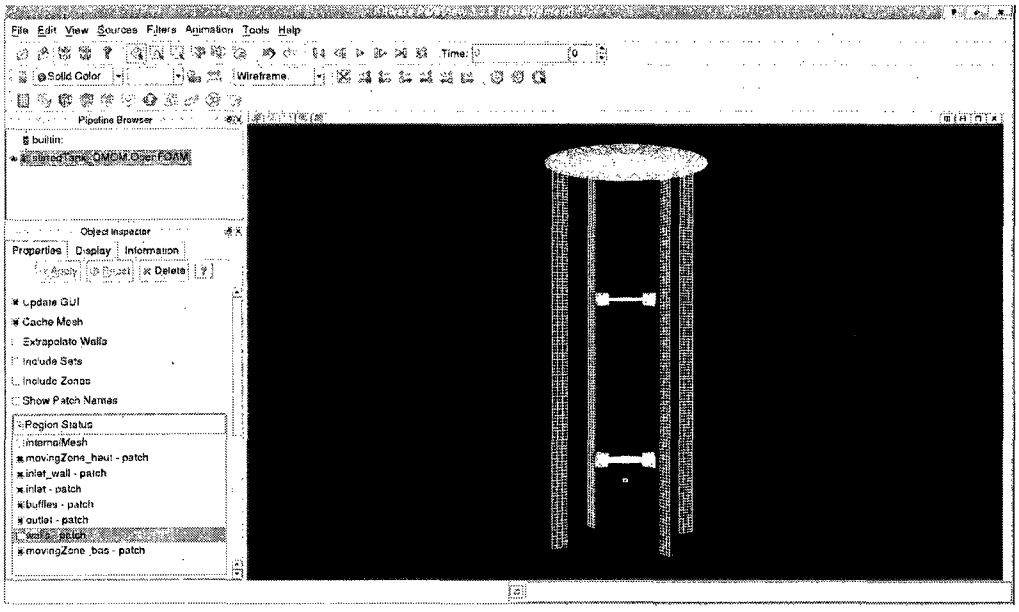

Figure A.2: The paraFoam window

visualisation application included in the CFD package.

A.5.1 Overview of paraFoam

paraFoam is strictly a script that launches ParaView using the reader module supplied with OpenFOAM. It is executed like any of the OpenFOAM utilities either by the single command from within the case directory or with the -case option with the case path as an argument, e.g.:

paraFoam -case <caseDir>

ParaView is launched and opens the window shown in FigureA.2. The case is controlled from the left panel, which contains several options for data analysis.

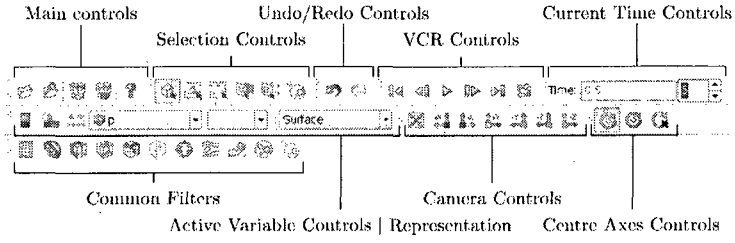

Figure A.3: Toolbars in ParaView

A.5.2 The button toolbars

The default layout with all toolbars is shown in FigureA.3 with each toolbar labelled. The function of many of the buttons is clear from their icon and, with tooltips enabled in the Help menu, the user is given a concise description of the function of any button.

Bibliography

[1] Bakker A. and van den Akker H.E.A. "a computational model for the gas-liquid flow in stirred reactors". *Chem. Eng. Res. Des., Part A: Trans. IChemE*, 72:594–606, 1994.

[2] Behzadi A., Issa R.I., and Rusche H. "modelling of dispersed bubble flow at high". *submitted to Chem. Eng. Sci.*, 1992.

[3] Sokolichin A. and Eigenberger G. "gas-liquid flow in bubble column and loop reactors (1994) i. detailed modelling and numerical simulation". *Chemical Engineering Science*, 49:5735–5747, 1994.

[4] Tomiyama A., Celata G.P., Hosokawa S., and Youshida S. "terminal velocity of single bubbles in surface tension force dominant regime". *International Journal of Multiphase Flow*, 28:1497–1519, 2002.

[5] Gosman A.D., R.I. Iss, Lekakou C., Looney M.K., and Politis S. "multidimensional modelling of turbulent two phase flows in stirred vissels". *AIChE Journal*, 38 (12):1946–1956, 1992.

[6] Chesters A.K. "an approximate bubble-eddy interaction model". *In Symp. Int. Union Th. Appl. Mech., Birmingham, UK, see [74]*, 1993.

[7] Stefano B. "computational fluid dynamics of gas-liquid flows including bubble population balance". *Ph.D. Thesis, Faculty of Enginnering and Science, Aalborg University*, 2005.

[8] Venneker B.C.H., Derksen J.J., and Van den Akker H.E.A. "population balance modelling of aerated stirred vessels based on cfd". *A.I.Ch.E. Journal*, 48:673–685, 2002.

[9] Launder B.E. and Spalding D.B. "the numerical computation of turbulent flows". *Comp. Meth. Appl. Mech. Eng.*, 3:269–289, 1974.

[10] Hjertager B.H. "computational fluid dynamics (cfd) analysis of multiphase chemical reactors". *Trends Chem. Eng.*, 4:45–92, 1998.

[11] Kralj C. "numerical simulation of diesel spray". *PhD thesis, Imperial College of Science, Technology and Medicine, University of London*, 1993.

[12] Martínez-Bazán C., Montan néz J.L., and Lasheras J.C. "on the breakup on an air bubble injected into a fully developed turbulent flow. part i: breakup freqency". *Journal of Fluids Mechanics*, 401:157, 1999a.

[13] Martínez-Bazán C., Montan néz J.L., and Lasheras J.C. "on the breakup on an air bubble injected into a fully developed turbulent flow. part ii: size pdf of the resulting daughter bubbles". *Journal of Fluids Mechanics*, 401:183, 1999b.

[14] Tsouris C. and Tavlarides L.L. "breakage and coalescence models for drops in turbulent dispersions". *A.I.Ch.E. Journal*, 40:395–406, 1994.

[15] Coulaloglou C.A. and Tavlarides L.L. "description of interaction processes in agitated liquid-liquid dispersions". *Chemical Engineering Science*, 32:1289–1297, 1977.

[16] Lathouwers D. "modelling and simulation of turbulent bubbly flow". *PhD thesis*, 1999.

[17] Pfleger D. and Becker S. "modelling and simulation of the dynamic flow behavior in bubble column". *Chemical Engineering Science*, 56:1737–1747, 2001.

[18] Pfleger D., Gomes S., Gilbert N., and Wagner H.G. "hydrodynamic simulations of laboratory scale bubble columns fundamental studies of the eulerian-eulerian modelling approach". *Chemical Engineering Science*, 54:5091–5099, 1999.

[19] Ramkrishna D. "solution of population balance equations". *Chemical Engineering Science*, 26, Issue 7:1134–1136, 1971.

[20] Ramkrishna D. "population balance". *Academic Press, San Diego*, 2000.

[21] Zhang D., Deen N.G., and Kuipers J.A.M. "numerical simulation of the dynamic flow behavior in a bubble column : A study of closures for turbulence and interface forces". *Chemical Engineering Science*, 61:7593–7608, 2000.

[22] Drew D.A. "continuum modeling of two-phase flows". *In R Meyer, editor, Theory of dispersed multphase flow*, pages 173–190, 1983.

[23] Drew D.A. "mathematical modeling of two-phase flow". *Ann. Rev. Fluid Mech.*, 15:261–291, 1983.

[24] Jacobs D.A.H. "preconditioned conjugate gradient methods for solving systems of algebraic equations". *Central Electricity Research Laboratories Repor*, page RD/L/N193/80, 1980.

[25] Spalding D.B. "numerical computations of multiphase flow and heat transfer". *In C. Taylor and K. Morgan, editors, Recent advances in numerical methods in fluids, Pineridge Press*, 1, 1981.

[26] Wilcox D.C. "turbulence modeling for cfd. second edition". *DCW Industries, Inc*, Second Edition, 1998.

[27] Lopez de Bertodano M., Lahey R.T.Jr., and Jones O.C. "development of a $k-\epsilon$ model for bubbly two-phase flow". *J. Fluids Eng., Trans. ASME*, 116(1):128–134, 1994.

[28] Lopez de Bertodano M., Lee S.-J., Lahey R.T.Jr., and Drew D.A. "the prediction of two-phase turbulence and phase distribution phenomena using a reynolds stress model". *J. Fluids Eng., Trans. ASME*, 112:107–113, 1990.

[29] Larue de Tournemine A. "bubble rise velocities". *Private Communication*, 2000.

[30] Aldis D.F. and Gidaspow D. "combustion of a polydispersed solid using a particle population balance". *Powder Technology*, 57,4:281–294, 1989.

[31] Marchisio D.L., Pikturna J.T, Fox R.O., and Vigil R.D. "quadrature method of moments for population balance equation". *AIChE Journal*, 49(5):1266–1276, 2005.

[32] Marchisio D.L. and Fox R. "multiphase reacting flows: Modelling and simulation". *International center for Mechanical Sciences*, 492:pp 44–48, 2007.

[33] Marchisio D.L., Vigil R.D., and Fox R.O. "quadrature method of moments for aggregation-breakage processes". *Journal of Colloid and Interfaces Science*, 258:322, 2003.

[34] Wang D.M. and Issa R. "two-phase turbulence modelling. a review". *Technical report, BRITE/EURAM II (BE 4098)*, pages II–14, 1992.

[35] L. Doubliez. "the drainage and rupture of a non-foaming liquid film formed upon bubble impact with a free surface". *International Journal of Multiphase Flow*, 17(6):783–803, 1991.

[36] Hill D.P. "the computer simulation of dispersed two-phase flows". *PhD thesis, Imperial College, University of London*, 1998.

[37] Patil D.P. and Andrews J.R.G. "an analytical solution to continuous population balance model describing floc coalescence and breakage - a special case". *Chemical Engineering Science*, 53:599–601, 1998.

[38] P. C. Duineveld. "bouncing and coalescence of two bubbles in water". *Ph.D. thesis, University of Twente, The Netherlands*, 1994.

[39] Olmos E., Gentric C., Vial C., Wild G., and Midoux N. "numerical simulation of multiphase flow in bubble column reactors. influence of bubble coalescence and break-up". *Chemical Engineering Science*, 56:6359–6365, (2001).

[40] Ervin E.A. and Tryggvason G. "the rise of bubbles in a vertical shear flow". *Journal of Fluids Engineering*, 119:443–449, 1997.

[41] A.F. Emery. "an evaluation of several differencing methods for inviscid fluid flow problems". *J. Comp. Physics*, 2:306–331, 1968.

[42] Crowe et al. and editors. "numerical methods in multiphase flows". *presented at the 1994 ASME Fluids Engineering Division Summer Meeting, Lake Tahoe, NV, USA*, 185, 1994.

[43] Augier F., Guiraud P., and Masbernat O. "volume fraction gradient induced flow patterns in a two-liquid phase mixing layer". *In Michaelides et al. [275].*

[44] Kerdouss F., Bannari A., and Proulx P. "cfd modelling of gas dispersion and bubble size in a double turbine stirred tank". *Chemical Engineering Science*, 61:3313–3322, 2006.

[45] Kerdouss F., Bannari A., Proulx P., Bannari R., Skrga M., and Labrecque Y. "two-phase mass transfer coefficient prediction in stirred vessel with a cfd model". *Computers and chemical Engineering*, 2007.

[46] Kerdouss F., Kiss L., Proulx P., Bilodeau J-F, and Dupuis C. "mixing characteristics of an axial-flow rotor: Experimental and numerical study". *Int. J. Chem. R. Eng.*, 3:A35, 2005.

[47] Lehr F. and Mewes D. "a transport equation for the interfacial area density applied to bubble columns". *Chemical Engineering Science*, 56:1159–1166, 2001.

[48] Rong F., Daniele L.M., and Rodney F. "application of the direct quadrature method of moments to polydisperse gas-solid fluidized bed". *Powder Technology*, 139:7–20, 2004.

[49] Robert F.M and Oliver S. "two- and three-dimensional simulations of bubble plume using a two-fluid model". *Chemical Engineering Science*, 54:5061–5069, 1999.

[50] Tabor G. "turbulence modelling at high phase fraction". *Technical report BRITE/EURAM III (BE 4322)*, pages III–14, 1999.

[51] Batchelor G.K. "the theory of homogeneous turbulence". *Combridge University Press, Combridge*, 1956.

[52] Lane G.L., Schwarz M.P., and Evans G.M. "predicting gas-liquid flow in a mechanically stirred tank". *Applied Mathematical Modeling*, 26:223–235, 2002.

[53] Laux H. "modelling of dilute and dense dispersed fluid-particle two-phase flows". *PhD thesis, Norwegian University of Science and Technology, Trondheim*, 1998.

[54] Luo H. "coalescence, breakup and liquid circulation in bubble column reactors". *D.Sc. Thesis, Norwegian Institute of Technology*, 1993.

[55] Luo H and Svendsen H.F. "theoretical model for drop and bubble breakup in turbulent dispersions". *A.I.Ch.E Journal*, 42:1225–1233, 1996.

[56] Rusche H. "computational fluid dynamics of dispersed two-phase flows at high phase fraction". *Imperial college of Science*, Ph.D. thesis, 2002.

[57] Tennekes H. and Lumley J.L. "a first course in turbulence". *The MIT Press*, 1972.

[58] Jakobsen H.A. "on the modelling and simulation of bubble column reactors using a two-fluid model". *PhD thesis, Norwegian University of Science and Technology, Trondheim*, 1993.

[59] Jakobsen H.A., Svendsen H.F., and Hjarbo K.W. "on the prediction of local flow structures in internal loop and bubble column reactors using a two-fluid model". *Comp. Chem. Eng.*, 17:531–536, 1993.

[60] Van Der Vorst H.A. "bi-cgstab: A fast and smoothly converging variant of bi-cg for the solution of nonsymmetric linear systems". *SIAM J. Scientific Computing*, 13(2):631–644, 1992.

[61] Weller H.G. "derivation, modelling and solution of the conditionally averaged two-phase flow equations". *Technical Report TR/HGW/02, Nabla Ltd.*, 2002.

[62] Boussinesq J. "théorie de l'écoulement tourbillant". *Mémoires présentés par divers savants*, pages 23–46, 1877.

[63] Grienberger J. "untersuchung und modellierung von blasensäulen". *PhD thesis, Universität Erlangen-Nürnberg*, 1992.

[64] Hrvoje J. "error analysis and estimation for the finite volume method with applications to fluid flows". *PhD Thesis, Diploma of Imperial College*, 1996.

[65] Kim J., Moin P., and Moser R. "turbulence statistics in fully developed channel flow at low reynolds number". *Journal of Fluid Mechanics*, 177:133–166, 1987.

[66] Joshi J.B. "computational flow modelling and design of bubble column reactors". *Chemical Engineering Science*, 56:5893–5933, 2001.

[67] Tannehill J.C., Anderson D.A., and Pletcher R.H. "computational fluid mechanics and heat transfer". *Taylor and Francis*, 1997.

[68] Lister J.D., Smith D.J, and Hounslow M.J. "adjustable discretized population balance for growth and aggregation". *AIChE Journal*, 41(3):591–603, 1995.

[69] Ferziger J.H. and Peric M. "computational methods for fluid dynamics". *Springer-Verlag, Berlin-New York*, 1995.

[70] Liou J.J., Srienc F., and Fredrickson A.G. "solutions of population balance models based on a successive generations approach". *Chemical Engineering Science*, 52, 9:1529–1540, 1997.

[71] Hinze J.O. "turbulence". *McGraw-Hill*, 1975.

[72] Jones J.P. and Launder B.E. "the prediction of laminarization with a two-equation model of turbulence". *Journal of Heat and Mass Transfer*, 15:301–314, 1972.

[73] Deardorff J.W. "a numerical study of three-dimensional turbulent channel flow at large reynolds number". *J. Fluid Mechanics*, 41:452, 1970.

[74] Eppinger K. "Étude du mouvement des bulles dans une turbulence homogène isotrope". *PhD thesis, Institut National Polytechnique de Toulouse*, 1995.

[75] Hagesather L., Jakobsen H.A., Hjarbo K., and Svendsen H. "a coalescence and breakup module for implementation in cfd codes". *Chemical Engineering Science*, 30:367, 2000.

[76] Erasmus L.D., Eyre D., and Everson R.C. "numerical treatment of the population balance equation using a spline-galerkin method". *Computers and Chemical Engineering*, 18, 9:775–783, 1994.

[77] Ishii M. "thermodynamic theory of two-phase flow". *Eyrolles, Paris*, 1975.

[78] Ishii M. and Zuber N. "drag coefficient and relative velocity in bubbly, droplet particle or partucalte flows". *AIChE journal*, 25:843–854, 1979.

[79] Laakkonen M., Alopaeus V., and Aittamaa J. "validation of bubble breakage, coalescence and mass transfer models for gas-liquid dispersion in agitated vessel". *Chemical Engineering Science*, 61:218–228, 2006.

[80] Lance M., Marièe J.L., and Bataille J. "homogeneous turbulence in bubbly flows". *J. Fluids Eng., Trans. ASME*, 113:295–300, 1991.

[81] Perić M. "a finite volume method for the prediction of three-dimensional fluid flow in complex ducts". *PhD thesis, Diploma of Imperial College*, 1985.

[82] Smith M. "constant-number monte carlo simulation of population balance". *Chemical Engineering Science*, 53(9):1777–1786, 1998.

[83] Vanni M. "approximate population balance equations for aggregation-breakage processes". *Journal of Colloid and Interface Science*, 221 (2):143–160, 2000.

[84] Gonzalez N.Y. Mendoza, El Morsli M., and Proulx P. "production of nanoparticles in thermal plasmas: a model including evaporation, nucleation, coalescence and fractal aggregation". *Journal of Thermal Spray Technology*, 2008.

[85] Hounslow M.J., Ryall R.L., and Marshall V.R. "a discretized population balance equation for nucleation, growth and aggregation". *AIChE Journal*, 34(11):1821–1832, 1988.

[86] Prince M.J. and Blanch H.W. "bubble coalescence and break-up in air sparged bubble columns". *A.I.Ch.E Journal*, 36:1485–1499, 1990.

[87] Rogers M.M. and Moin P. "the structure of the vorticity fleld in homogeneous turbulent flows". *J. Fluid Mechanics*, 176:33–66, 1987.

[88] Guimaraes M.M.L. and Cruz-Pinto J.J.C. "mass transfer and dispersed phase mixing in liquid-liquid systems". *Computers and Chemical Engineering*, 12,11:1075–1082, 1988.

[89] Chen M.Q., Hwang C., and Shih Y.P. "a wavelet-galerkin method for solving population balance equations". *Computers and Chemical Engineering*, 20, 2:131–145, 1996.

[90] Bhole M.R., Joshi J.B., and Ramkrishna D. "cfd simulation of bubble columns incorporating population balance modeling". *Chemical Engineering Science*, 63:2267–2282, 2008.

[91] Hestens M.R. and Steifel E.L. "method of conjugate gradients for solving linear systems". *Journal of Research*, 29:409–436, 1952.

[92] Simonin O. "combustion and turbulence in two-phase flows". *In Lecture Ser. continuum modelling of dispersed phase flows. Von Karman Institute for Fluid Dynamics*, 1996.

[93] Chen P., Sanyal J., and Dudukovic M.P. "cfd modelling of bubble columns flow : implementation of population balance". *Chemical Engineering Science*, 59:5201–5207, 2004.

[94] Chen P., Sanyal J., and Dudukovic M.P. "numerical simulation of bubble columns flows:effect of different breakup and coalescence closures". *Chemical engineering science*, 60:1085–1101, 2005.

[95] Chen P., Dudukovic M.P., and Sanyal J. "numerical simulation of bubble columns flows : effect of different break-up and coalescence closures". *Chemical Engineering Science*, 60:1085–1101, 2005.

[96] Chen P., Dudukovic M.P., and Sányal J. "three dimensional simulation of bubble columns flows with bubble coalescence and break-up". *AIChE Journal*, 51:696–712, 2005.

[97] Saffman P.C. and Turner J.S. "on the collision of drops". *AIAA J.*, 14:1241–1249, 1976.

[98] Carrica P.M., Drew D., Bonetto F., and Lahey R.T.Jr. "a polydisperse model for bubbly two-phase flow around a surface ship". *International Journal of Multiphase Flow*, 25:257–305, 1999.

[99] Singh P.N. and Ramkrishna D. "solution of population balance equations by mwr". *Chemical Engineering Science*, 1, Issue 1:23–31, 1977.

[100] Wu Q., Kim S., Ishii M., and Beus S.G. "one-group interfacial area transport in vertical bubbly flow". *International Journal of Heat Mass Transfer*, 41 (8/9):1103–1112., 1998.

[101] Bannari R., Bannari A., Selma B., and Proulx P. "design and cfd analysis of mass transfer and distributions of shear stresses in airlift reactor". *Chemical Engineering Science, submitted 2009*, 2009.

[102] Bannari R., Kerdouss F., Selma B., Bannari A., and Proulx P. "three-dimensional mathematical modeling of dispersed two-phase flow using class method of population balance in bubble column". *Computers and Chemical Engineering*, 3224-3237:32, 2008.

[103] Bel F'Dhila R. and Simonin O. "eulérian prediction of a turbulent bubbly flow downstream a sudden pipe expansion". *In Six workshop on two-phase flow predictions*, 1992.

[104] Clift R., Grace J.R., and Weber M.E. "bubbles, droplets and particles". *Academic Press*, 1978.

[105] Fan R., Marchisio D.L., and Fox R.O. "application of the direct quadrature method of moments to polydispersed gas-solid fluidized beds". *Journal of Aerosol Science*, 139:7–20, 2004.

[106] Krishna R., van Baten J.M., and Urseanu M.I. "three-phase eulerian simulations of bubble column reactors operating in the chur-turbulent regime : A scale upstrategy". *Chemical Engineering Science*, 55:3275–3286, 2000.

[107] McGraw R. "description of aerosol dynamics by the quadrature method of moments". *Aerosol Science and Technology*, 27:255–265, 1997.

[108] McGraw R. and Wright D.L. "chemically resolved aerosol dynamics for internal mextures by the quadrature method of moments". *Journal of Aerosol Science*, 34:189–309, 2003.

[109] Warming R.F. and Beam R.M. "upwind second order differencing schemes and applications in aerodynamic flows". *AIAA J.*, 14:1241–1249, 1976.

[110] Issa R.I. "solution of the implicitly discretized fluid flow equations by operator-splitting". *J. Comp. Physics*, 62:40–65, 1986.

[111] Issa R.I. "a simple model for c_t". *Private Communication, see [?]*, 1992.

[112] Issa R.I. and Oliveira P.J. "modelling of turbulent dispersion in two phase flow jets". *In turbulence and Experiments*, 2:947–957, 1992.

[113] Batterham R.J., Hall J.S., and Barton G. "pelletizing kinetics and simulation of full-scale balling circuits". *3rd International Symposium on Agglomeration, Germany*, A136, 1981.

[114] Bajpai R.K., Ramkrishna D., and Prokop A. "a coalescence redispersion model for drop-size distributions in an agitated vessel". *Chemical Engineering Science*, 31, Issue 10:913–920, 1976.

[115] Rogallo R.S. and Moin P. "numerical simulation of turbulent flows". *Annual Review of Fluid Mechanic*, 16:99–137, 1984.

[116] Elghobashi S. and Truesdell G.C. "direct simulation of particle dispersion in a decaying isotropic turbulence". *J. Fluid Mech*, 242:655–700, 1992.

[117] Kumar S. and Ramkrishna D. "on the solution of population balance equations by discretization i. a fixed pivot technique". *Chemical Engineering Science*, 51(8):1311–1332, 1996.

[118] Kumar S. and Ramkrishna D. "on the solution of population balance equations by discretization ii. a moving pivot technique". *Chemical Engineering Science*, 51, 8:1333–1342, 1996.

[119] Kumar S., Vanderheyden W.B., Devanathan N., Duduković M.P. Padial N.T., and Kashiwa B.A. "numerical simulation and experimental verification of the gas-liquid flow in bubble columns". *In Industrial Mixing Fundamentals with Applications, AIChE Symp. Ser.*, 91:11–19, 1995.

[120] Lo S. "application of the musig model to bubbly flows". *AEAT-1096, AEA Technology*, 1996.

[121] Muzaferija S. "adaptive finite volume method for flow prediction using unstructured meshes and multigrid approach". *PhD thesis, Diploma of Imperial College*, 1994.

[122] Politis S. "prediction of two-phase solid-liquid turbulent flow stirred vessels". *PhD thesis, Imperial College, University of London*, 1989.

[123] Lee S.-J., Lahey R.T.Jr., and Jones O.C.Jr. "the prediction of two-phase turbulence and phase distribution using a $k-\epsilon$ model". *Jap. J. Multiphase Flow*, 3(4):335–368, 1989.

[124] Peyret S.B. and Taylor T.D. "computational methods for fluid flow". *3 ed ed.. Springer-Verlag, New York*, 1990.

[125] Elghobashi S.E. and Abou-Arab T.W. "a two-equation turbulence model for two-phase flows". *Physis. Fluids*, 26 (4):931–938, 1983.

[126] Alves S.S., Maia C.I., and Vasconcelos J.M.T. "experimental and modelling study of gas dispersion in a double turbine stirred tank". *Chemical Engineering Science*, 57:487–496, 2002.

[127] Alves S.S., Maia C.I., Vasconcelos J.M.T., and Serralheiro A.J. "bubble size in aerated stirred tanks". *Chemical Engineering Journal*, 89:109–117, 2002.

[128] Patankar S.V. "numerical heat transfer and fluid flow". *Hemisphere Publishing Corporation*, 1981.

[129] Eswaran V. and Pope S.B. "an examination of forcing in direct numerical simulations of turbulence". *Computers and Fluids*, 16(3):257–278, 1988.

[130] Eswaran V. and Pope S.B. "direct numerical simulations of the turbulent mixing of a passive scalar". *Physics of Fluids*, 31(3):506–520, 1988.

[131] Thai V.D., Minier J.P., Simonin O., Freydier P., and Olive J. "multidimensional two-fluid model computation of turbulent dispersed two-phase flows". *Crowe et al. [64]*, pages 277–291.

[132] Buwa V.V., Dhanannjay S.D., and Ranade V.V. "eulerian-lagrangian simulations of unsteady gas-liquid flows in bubble columns". *International Journal of Multiphase Flow*, 32:864–885, 2006.

[133] Buwa V.V. and Ranade V.V. "dynamics of gas-liquid flow in a rectangular bubble column: experiments and single/multi-group cfd simulations". *Chemical Engineering Science*, 57:4715–4736, 2002.

[134] Buwa V.V. and Ranade V.V. "mixings in bubble columns reactors: role of unsteady flow structures". *Canad. J. Chem. Eng.*, 81:402, 2003.

[135] Buwa V.V. and Ranade V.V. "characterisation of gas-liquid flows in rectangular bubble columns using conductivity probes". *Chem. Eng. Commun.*, 192:1129, 2005.

[136] Ranade V.V. "flow in bubble columns : Some numerical experiments". *Chemical Engineering Science*, 47:1857–1869, 1992.

[137] Ranade V.V. "modelling of turbulent flow in a bubble column reactor". *Chem. Eng. Res. Des, Part A: Trans. IChemE*, 75:14–23, 1997.

[138] Na Y. and Moin P. "direct numerical simulation of separated turbulent boundary layer". *Journal of Fluid Mechanics*, 370:175–201, 1998.

[139] Sato Y. and Sekoguchi K. "liquid velociy distribution in two-phase bubble flow". *International Journal of Multiphase Flow*, 2:79–95, 1975.

[140] Xiong Y. and Pratsinis S.E. "formation of irregular particles by coagulation and sinteringa two-dimensional solution of the population balance equation". *Journal of Aerosol Science*, 22, 1:S199–S202, 1991.